

Copyright
by
Jung-Kuei Chang
2008

The Dissertation Committee for Jung-Kuei Chang
Certifies that this is the approved version of the following dissertation:

**The Effect of Microstructure on Cavitation during Hot Deformation in
Fine-grained AA5083 Aluminum Alloy Sheet Material**

Committee:

Eric M. Taleff, Supervisor

Desiderio Kovar

Llewellyn K. Rabenberg

Paulo Ferreira

Maria Juenger

**The Effect of Microstructure on Cavitation during Hot Deformation in
Fine-grained AA5083 Aluminum Alloy Sheet Material**

by

Jung-Kuei Chang, B. S.; M. S.

Dissertation

Presented to the Faculty of the Graduate School of

The University of Texas at Austin

in Partial Fulfillment

of the Requirements

for the Degree of

Doctor of Philosophy

The University of Texas at Austin

December 2008

Dedication

To the loving memory of my father.

Acknowledgements

I would like to thank my committee members for all their help. My deepest gratitude goes to my advisor, Dr. Eric M. Taleff, for his expertise, guidance and encouragement throughout my graduate study. I also thank Dr. James Ciulik for giving me extensive comments on my dissertation, which have made me think more critically about the issue involved in this research. Thanks are also extended to Dr. Desiderio Kovar, Dr. Llewellyn K. Rabenberg, Dr. Paulo Ferreira and Dr. Maria Juenger, for their instructions and advisement.

I extend many thanks to my colleagues and friends, especially Amanda Niazi, and Ricardo Vanegas, for their advice and companionship.

Most importantly, none of this would have been possible without the love and support of my family. A special thank-you is extended to my parents, whose love and devotion has guided me through my education. I am especially grateful to my wife, Daisy Fan, for her patience and for helping me keep my life in proper perspective. Finally, I would like to thank my son, Ryan, for keeping me company and being cooperative throughout the dissertation writing.

The Effect of Microstructure on Cavitation during Hot Deformation in Fine-grained AA5083 Aluminum Alloy Sheet Material

Publication No. _____

Jung-Kuei Chang, Ph.D.

The University of Texas at Austin, 2008

Supervisor: Eric M. Taleff

Aluminum alloys are of great interest to the automobile industry for vehicle mass reduction, which improves vehicle performance and reduces emissions. Hot forming processes, such as superplastic forming (SPF) and quick-plastic forming (QPF) have been developed to take advantage of the improved formability of certain aluminum materials at elevated temperature. Commercial fine-grained aluminum alloy AA5083 sheet is the most commonly used material in the SPF and QPF forming processes. Hot formability of AA5083 is often limited by material cavitation during forming, which makes understanding and controlling cavitation an issue of primary importance for improving hot sheet forming processes. The thermomechanical processing history of AA5083 can strongly affect superplastic performance, causing variations in formability between material lots. These variations are closely related to microstructure, and intermetallic particles are prime suspects for controlling cavitation behavior. However, there has been little more than anecdotal evidence available that these particles nucleate or influence

cavitation. Interactions between intermetallic particles and cavities were, thus, analyzed using both two-dimensional (2-D) and three-dimensional (3-D) microstructure characterization techniques. Analysis of 3-D microstructures from AA5083 specimens deformed under conditions similar to the SPF and QPF processes provide conclusive proof that cavities form at specific types of intermetallic particles. Differences in cavitation between materials deformed under the SPF and QPF processes result from differences in deformation mechanisms. These differences are illustrated by the formation of filaments on fracture surfaces of superplastically deformed AA5083 specimens, which have been characterized.

Table of Contents

Acknowledgements	v
Abstract	vi
List of Tables	x
List of Figures	xi
Chapter 1: Introduction	1
Chapter 2: Background	3
2.1 Aluminum for Automotive Structural Components	3
2.1.1 Superplastic Forming	6
2.1.2 Quick-Plastic Forming	7
2.2 Deformation Mechanisms	8
2.2.1 Grain-Boundary-Sliding Creep	9
2.2.2 Solute-Drag Creep	11
2.3 Failure Mechanisms	12
2.4 Cavitation Behavior	13
2.4.1 Nucleation	13
2.4.2 Growth	14
2.4.3 Coalescence	15
2.5 Filaments on the failure surface	15
Chapter 3: Motivation of Problem and Methodology for Solution	23
3.1 Problem Statement	23
3.2 Characterization Techniques	25
3.3 Design of Experiment	27
Chapter 4: Experimental Procedures	33
4.1 Materials	33
4.2 High-Temperature Mechanical Tests	33
4.3 Elongation-to-Failure Tests in Air and in Vacuum	34

4.4 Failure Surface Characterization.....	35
4.5 Serial Sectioning Metallography.....	36
4.5.1 Sample Preparation	36
4.5.2 Image Acquisition.....	38
4.5.3 Microstructure Reconstruction.....	39
4.6 Two-Point Correlation Analysis	40
4.6.1 Computation of Two-Point Correlation Functions	40
4.6.2 Representing Two-Point Correlation Functions	46
Chapter 5: Failure Surface Characterization.....	61
5.1 Failure surface morphology	62
5.2 EDS analysis on filaments	63
5.3 Summary	65
Chapter 6: Three-Dimensional Characterization	72
6.1 Visualization of 3-D Data Sets	73
6.2 Qualitative Analysis of Microstructure in 3-D Data Sets	74
6.3 Quantitative Analysis of Cavities in 3-D Data Sets.....	75
6.4 Quantitative Analysis of Particles in 3-D Data Sets	78
6.5 Relationships between Particles and Cavities.....	79
Chapter 7: Two-Dimensional Characterization	91
7.1 The Cavity – Cavity Correlation.....	94
7.2 The Al ₆ (Mn,Fe) – Cavity Correlation.....	94
7.3 The Mg-Si – Cavity Correlation	95
Chapter 8: Conclusion.....	104
Appendix.....	106
Bibliography	114
Vita	124

List of Tables

Table 4.1:	Composition of the AA5083 material in weight percent.	47
Table 4.2:	Test true-strain rate ($\dot{\epsilon}$) at 450°C, number of cavities, cavity volume fraction and average individual cavity volume measured from the three 3-D data sets.	47
Table 5.1:	EDS analysis of chemical composition (in atomic %) is shown for: (a) a polished AA5083 material, (b) high-purity Al ₂ O ₃ powder and (c) a filament from a specimen tested in air. Results are shown for several electron beam energies.	67
Table 5.2:	The average EDS composition of filaments in atomic %.	68
Table 5.3:	The surface compositions of AA5083 specimens (in atomic %) by EDS at 20 keV	68
Table 6.1:	The number of particles, percentage of particles adjacent to cavities, average size of adjacent particles and average size of non-adjacent particles are given as a function of particle type in the 3-D data sets. Each 3-D data set has a volume of 540 × 360 × 25 μm.	81
Table 7.1:	The number and area fraction of cavity and two types of intermetallic particles are shown for three data sets.	97

List of Figures

Fig. 2.1:	A schematic of the SPF process is shown.....	17
Fig. 2.2:	A schematic representation of a QPF cell shows various stages in the process. Taken from [8].	17
Fig. 2.3:	Typical creep behavior of AA5083 materials is presented as a plot of the logarithm of Zener-Hollomon parameter against the logarithm of Young's modulus compensated stress using a single value of $Q_c = 110$ kJ/mole across both deformation mechanisms. The plot is from reference [1].....	18
Fig. 2.4:	A model is shown of grain boundary sliding accommodated by dislocation motion involving the sequential steps of glide and climb, from reference [37].	19
Fig. 2.5:	Failure regions of AA5083 specimens are shown for (a) failure controlled by cavitation when deformation dominated by GBS creep and (b) failure controlled by flow localization when deformation dominated by SD creep. Small windows on top of each image show each specimen at lower magnification.	20
Fig. 2.6:	Micrographs of AA5083 show cavity morphology under deformation by (a) GBS creep and (b) SD creep. Both the tensile axis and rolling direction are horizontal in each image.	21
Fig. 2.7:	A schematic shows possible cavitation mechanisms proposed by Khaleel et al, from reference [65].	22
Fig. 2.8:	A schematic shows possible cavitation mechanisms proposed by Bae et al, from reference [47]. Cavity nucleation and growth at (a) the particle-grain boundary interface and (b) the particle-matrix interface.	22
Fig. 3.2:	An optical photomicrograph of as-polished AA5083 material is shown. Intermetallic particles in the micrograph are black in color.	30
Fig. 3.3:	These figures demonstrate why cavity-cavity connectivity and cavity-particle adjacency cannot be determined from 2-D sections.	31
Fig. 3.4:	Trends from data in Ref. [1] for cavity fraction as a function of tensile straining are shown for a test temperature of 450 °C and true strain rates which produce deformation controlled by GBS creep ($3 \times 10^{-4} \text{ s}^{-1}$) and SD creep ($3 \times 10^{-2} \text{ s}^{-1}$). Points A, B and C represent the three mechanical testing conditions chosen for investigation.....	32
Fig 4.1:	The geometry of the tensile coupons (a) for high temperature mechanical test and elongation-to-failure tests in air, and (b) for elongation-to-failure tests in vacuum.	48

Fig. 4.2:	Images are shown of (a) a photograph of the test fixture and (b) a schematic (by Brian South) of the fixture.	49
Fig. 4.3:	Photographs of testing frames as shown for (a) high temperature mechanical tests, (b) elongation-to-failure tests in air and (c) elongation-to-failure tests in vacuum.	50
Fig. 4.4:	Coupons tested at 450°C under each of the three testing conditions are shown with an untested coupon. Regions representative of those from which metallographic specimens were removed are circled.	51
Fig. 4.5:	The flow chart of the serial sectioning processes.	52
Fig. 4.6:	The geometry of the Vickers diamond indenter is shown.	53
Fig. 4.7:	The Allied High Tech MultiPrep™ polishing system is shown.	53
Fig. 4.8:	An example of 2-D microstructure image used for serial section metallography is shown.	54
Fig. 4.9:	An example of a 3-D microstructure reconstruction is shown.	54
Fig. 4.10:	The EDS mappings of Al ₆ (Mn,Fe) particles are shown.	55
Fig. 4.11:	The EDS mappings of an Mg-Si particle are shown.	56
Fig. 4.12:	The method of two-point correlation function calculation is shown graphically.	57
Fig. 4.13:	A series of schematic diagrams demonstrates the two-point correlation function methodology of the current study. In (a), an example of a two-phase microstructure image is shown. In (b), the definition of transportable analysis array, base point and measurement frame are shown. Figures (c), (d), (e) and (f) show the calculation method for the two-point correlation function.	58
Fig. 4.14:	Two calculation methods for correlation probability from a transportable analysis array are shown. The probability in percentage is calculated from a transportable analysis array by dividing by the maximum count of the array, which is 8 in this case. The probability in normalized value is calculated from a transportable analysis array by dividing by the average value of the array, which is 2.36 in this case.	59
Fig. 4.15:	Two contour plots of the same Al ₆ (Mn,Fe)/cavity correlation. The numbers in contour lines represent (a) percentage and (b) normalized correlation.	60
Fig. 5.2:	Simulated electron beams interact with AA5083 bulk material are shown. The energies of electron beams simulated are: (a) 5 keV, (b) 10 keV and (c) 20 keV.	70
Fig. 5.3:	A filament analyzed at a reduced beam energy of 10 keV and the EDS scan area are shown.	71

Fig. 6.1:	Data for cavity content as a function of strain are shown in a plot similar to that of Fig. 3.4, which was used in the design of experiments. Open symbols are data for cavity area fraction from Ref. [1]. Filled symbols are cavity volume fractions measured from the three metallographic specimens examined in this investigation.	82
Fig. 6.2:	Example 2-D photomicrographs from (a) SD 1.3, (b) GBS 0.9 and (c) GBS 1.3 specimens used for 3-D microstructure reconstructions are shown.	83
Fig. 6.3:	Three optical photomicrographs taken at three different polishing depths in specimen SD 1.3 are shown. The plane of (b) is 2.5 μm below that of (a), and the plane of (c) is 5 μm below that of (a). Four microstructural features can be distinguished: matrix, cavity, $\text{Al}_6(\text{Mn,Fe})$ intermetallic and Mg-Si intermetallic.	84
Fig. 6.4:	3-D microstructure reconstructions from serial sections of (top) SD 1.3, (middle) GBS 0.9 and (bottom) GBS 1.3 specimen data sets are shown. In the left column, all distinguishable objects are displayed. In the right column, a select region of each 3-D data set is shown at higher magnification.	85
Fig. 6.5:	3-D microstructure reconstructions for intermetallic particles from serial sections of (a) SD 1.3, (b) GBS 0.9 and (c) GBS 1.3 specimen data sets are shown.	86
Fig. 6.6:	Cavity shape factor against cavity equivalent spherical diameter for (a) SD1.3, (b) GBS 0.9 and (c) GBS 1.3 specimens are shown.	87
Fig 6.7:	$\text{Al}_6(\text{Mn,Fe})$ particle shape factor against particle equivalent spherical diameter for (a) SD1.3, (b) GBS 0.9 and (c) GBS 1.3 specimens are shown.	88
Fig 6.8:	Mg-Si particle shape factor against particle equivalent spherical diameter for (a) SD1.3, (b) GBS 0.9 and (c) GBS 1.3 specimens are shown.	89
Fig. 6.9:	Intermetallic particle size distributions for (a) $\text{Al}_6(\text{Mn,Fe})$ and (b) Mg-Si are shown.	90
Fig. 6.10:	The fraction of particles adjacent to cavities is shown as a function of equivalent spherical particle diameter for (a) $\text{Al}_6(\text{Mn,Fe})$ and (b) Mg-Si intermetallic particles.	90
Fig. 7.1:	Images used for two-point correlation function analysis from 2-D data sets (a) SD 1.3, (b) GBS 0.9 and (c) GBS 1.3 are shown. Microstructural features in these images are cavities in gray, $\text{Al}_6(\text{Mn,Fe})$ particles in yellow and Mg-Si particles in purple.	98

Fig 7.2:	Histograms of the size distributions for (a) cavity (b) $\text{Al}_6(\text{Mn,Fe})$ particles and (c) Mg-Si particles from images of three data sets are shown.	99
Fig. 7.3:	Two-point correlation analyses for (a) SD 1.3: Cavity/Cavity, (b) GBS 0.9: Cavity/Cavity and (c) GBS 1.3: Cavity/Cavity are reported in contour plots.....	100
Fig. 7.4:	Two-point correlation analyses for (a) SD 1.3: $\text{Al}_6(\text{Mn,Fe})/\text{Cavity}$, (b) GBS 0.9: $\text{Al}_6(\text{Mn,Fe})/\text{Cavity}$ and (c) GBS 1.3: $\text{Al}_6(\text{Mn,Fe})/\text{Cavity}$ are reported in contour plots.	101
Fig. 7.5:	Two-point correlation analyses for (a) SD 1.3: Mg-Si/Cavity, (b) GBS 0.9: Mg-Si/Cavity and (c) GBS 1.3: Mg-Si/Cavity are reported in contour plots.....	102
Fig. 7.6:	Two-point correlation analyses for (a) SD 1.3: Cavity/Separate Cavity, (b) SD 1.3: $\text{Al}_6(\text{Mn,Fe})/\text{Separate Al}_6(\text{Mn,Fe})$ and (c) GBS 0.9: Cavity/Separate Cavity are reported in contour plots.	103

Chapter 1: Introduction

As the price of fuel reaches new highs, consumer awareness of the operational costs over the lifetime of a vehicle can become a major buying consideration. Meanwhile, the growing public and scientific concern for greenhouse gas (GHG) emissions forces the automotive industry to meet ever more stringent performance requirements of government regulations. Several different approaches are known to improve vehicle fuel efficiency and reduce vehicle emissions, such as alternative powertrain technologies and vehicle lightweighting. However, these improvements require additional investment in manufacturing and raise vehicle cost. Among these technologies, aluminum for lightweighting of vehicles provides the most cost-effective improvement while maintaining the strength requirements for vehicle safety. Besides several desirable properties of aluminum, the most attractive characteristic is low density, which is only one-third that of steel. Replacing steel parts with aluminum parts can significantly reduce the mass of a vehicle, which not only improves the performance but also reduces the powertrain size required for the same performance. These benefits make aluminum of increasing importance in automobile industry.

The lesser room-temperature ductility of aluminum compared to steel requires the automobile industry to seek new alternatives to conventional stamping operations to produce parts from aluminum sheet. Hot and warm forming techniques, such as superplastic forming (SPF) and quick plastic forming (QPF), were developed to improve the formability of aluminum. These forming techniques generally involve hot gas-pressure forming to produce panels of complex shapes using commercial fine-grained aluminum alloy AA5083 sheet, which is the most-used material for SPF and QPF processes. Although fine-grained commercial AA5083 materials possess superior

superplastic performance, these materials exhibit a large variability in superplastic ductilities, even between different material lots from the same supplier. Aside from a small variation in chemical composition, the only difference between these AA5083 materials is processing history, which may lead to different microstructures. On the other hand, variations in ductility were found to be closely related to cavitation damage during the forming processes [1]. Because of the importance of formability and material performance predictions for the SPF and QPF processes, there is a need to better understand cavitation evolution and the interaction between cavities and microstructural features.

The intent of this dissertation is to characterize the cavitation behaviors of commercial AA5083 material under deformation mechanisms corresponding to SPF and QPF processes. The necessity of three-dimensional (3-D) characterization for studying cavitation behaviors is discussed. A serial sectioning metallography technique was used to obtain 3-D microstructure data for 3-D visualizations and analyses. Results from 3-D characterization are provided and compared with analyses using two-point correlation functions from two-dimensional (2-D) images. The evolution of cavitation and correlation between cavities and intermetallic particles are emphasized. Unusual filament structures have been observed on the fracture surfaces of Al-Mg alloys after superplastic deformation. Such filaments on fracture surfaces of AA5083 specimens are characterized in this study.

Chapter 2: Background

2.1 ALUMINUM FOR AUTOMOTIVE STRUCTURAL COMPONENTS

Public concern for environmental issues, concern for the future availability of petroleum and increasing fuel costs are creating a demand for more fuel efficient vehicles. In response to these pressures, the automobile industry is vigorously pursuing vehicle lightweighting. Vehicle mass is the single greatest factor affecting fuel efficiency. Current-generation alternative powertrains, such as gasoline-electric hybrids, significantly increase vehicle mass, which makes reduction of mass in the vehicle structure even more critical. There are three methods to reduce vehicle mass. Vehicle size can be decreased, which involves primarily issues of design and marketing. Less material can be used without changing vehicle size. This requires more efficient structures, which typically requires improved metal forming technologies to produce more complex components. Metals, primarily steels, currently used in vehicle structures can be replaced with light-weight metals, such as aluminum and magnesium alloys. Composite systems, such as fiber-reinforced polymers, are far from being cost competitive with metals for most consumer vehicles and are, thus, not a credible alternative to metals for either manufacturing more complex parts or as a replacement for steels.

Steel has traditionally been the most prevalent material used for structural components in consumer automobiles. New generations of advanced steels, such as high strength low alloy (HSLA) steels, continue to provide decreased vehicle structure mass with improved performance [2]. However, even greater gains in vehicle lightweighting can be achieved by using light alloys. Moreover, recent increases in fuel costs make light alloys, which generally have a higher cost than steels, quite attractive for use in consumer vehicles. Aluminum currently offers the greatest potential for improved fuel economy

through vehicle lightweighting at the lowest cost, compared with other current technologies [3]. The use of aluminum alloys in automotive closure applications, which generally require wrought metal alloys, can reduce mass by 30 to 50% compared with similar steel closures [4]. Mass reduction dramatically affects fuel economy. Approximately 0.4 mpg are gained for every 100 lbs. of weight reduction [5]. Another important benefit of using vehicle light weighting is a reduction in CO₂ emissions; every kilogram of aluminum which replaces two kilograms of steel can provide a net reduction in CO₂ emissions of 10 kg over the life of a vehicle [6].

A major barrier to the introduction of aluminum into the vehicle body-in-white is its low formability compared to steels. While steels can offer a maximum formability of up to 50% in cold stamping, aluminums offer a maximum of only 30%. Overcoming this formability issue is a critical enabler for using aluminum to reduce the mass of vehicle structures. Aluminum otherwise offers the very attractive qualities of good specific stiffness, good specific strength, good weldability and excellent corrosion resistance. By using hot forming technologies, the effective formability of some aluminum alloys can be increased to well over 100%, enabling the forming of complex components impossible to manufacture in steel. Thus, hot forming can enable both insertion of light alloy, i.e. aluminum, components into a vehicle structure and the use of less material by producing more efficient, and more complex, components. Two sheet hot-forming technologies are used to form automotive structural and closure components, superplastic forming (SPF) and quick-plastic forming (QPF) [1, 7-8].

Alloy AA5083 sheet is the most commonly used material for hot forming of light panel structures [7]. This alloy is a non-heat-treatable alloy with a nominal composition of Al-4.5Mg-0.7Mn-0.1Cr-0.25Zn-0.5Si-0.4Fe-0.1Cu in wt. pct [9]. AA5083 offers many desirable properties for use in automobile body structures, such as low density, high

strength, good corrosion resistance and good weldability. This alloy can be processed to have a fine grain size and excellent superplastic response [1, 10-12]. Such fine-grained microstructure not only promotes superplastic performance during deformation at elevated temperatures, but also provides good mechanical strength at room temperature. The high Mg concentration in AA5083 provides solid-solution strengthening at room temperature and can produce solute-drag creep at elevated temperatures.

Fine-grained AA5083 aluminum sheet is used for hot-forming automotive body panels by gas pressure in the SPF and QPF processes. The fine-grained AA5083 alloy for hot forming applications is achieved through thermomechanical processing, which includes large cold rolling strain. Thickness reduction during final cold rolling is approximately 75% for production of fine-grained AA5083 sheet. Recrystallization after cold rolling, which typically occurs during heating prior to hot forming, occurs by particle-stimulated nucleation (PSN) of recrystallization [13-14]. This reaction involves the nucleation of new grains in the highly deformed regions around dispersed particles. The high Mn content of AA5083 is required to produce a significant volume fraction of Al_6Mn particles, proeutectic products, with sizes of greater than approximately $2\text{ }\mu\text{m}$ to locally concentrate matrix strain during cold rolling and activate the PSN mechanism. A fine-grained ($<10\text{ }\mu\text{m}$) microstructure with random recrystallization texture is achieved with uniformly-distributed constituent particles [13, 15]. In addition to the rather coarse particles, proeutectic products, of Al_6Mn , Mn additions also create fine precipitates which pin grain boundaries and stabilize grain size at elevated temperatures [15]. These precipitates do not otherwise provide any significant strengthening at room temperature. In addition, superplastic performance can be improved by lowering the amount of Fe and Si impurities [16-17] or by promoting grain-boundary-sliding (GBS) creep through Cu addition [18-19]. The most common particle observed in AA5083 is $\text{Al}_6(\text{Mn,Fe})$ with

sizes of the order of one micrometer [20-22]. Other particles commonly reported by literatures include Mg_2Si [20, 23-25] and $(\text{Fe,Mn})_3\text{SiAl}_{12}$ (50-100nm) [21, 23, 25].

2.1.1 Superplastic Forming

After 40 years of development, SPF is now considered a standard process in several industries, including aerospace and transportation [26]. SPF depends on the phenomenon of superplasticity, the capability of certain alloys to undergo extensive, neck-free, tensile deformation at elevated temperature (typically $T > 0.5 T_m$, T_m is the melting temperature of the material) prior to fracture [27]. Superplastic behavior is commonly associated with a high strain-rate sensitivity, m , as in Eqn. 2.1

$$\sigma = K\dot{\epsilon}^m \quad (2.1)$$

where σ is the flow stress, $\dot{\epsilon}$ is true strain rate and K is a constant which depends on test temperature, material and microstructure. The m values for most metals are less than 0.3, whereas superplastic materials achieve m values of 0.5 or greater. Superplastic deformation is associated with GBS creep, which requires a fine grain size, typically less than 10 μm . A typical SPF process uses hot gas pressure to form a sheet into a single-sided die of desired shape, as shown in Fig. 2.1. The single-sided tool is far less expensive than matched tooling for low volume production, for which capital investment must be minimized. SPF has been extensively used in the aerospace industry because small production quantities are required and complex parts must be produced in materials with relatively low room-temperature formability [28]. SPF has the ability to achieve large strains to failure in aluminum sheet alloys for the manufacture of complex panels. In addition to the low-capital-investment requirements of SPF, the high forming temperature associated with this process results in stress relieving, which eliminates springback, a common and costly problem encountered with conventional cold-stamping process. However, within the automotive industry, the primary problems with SPF

technology are manufacturing cost and productivity which greatly depend on forming cycle time. Beside the requirement of costly SPF-grade fine-grained aluminum alloys, SPF involves operating at an elevated temperature of 500°C or higher and a relatively slow strain-rate of 10^{-3} s^{-1} or slower. These requirements make SPF an expensive process with long forming time and, thus, only suitable for low-production, niche automobile applications.

2.1.2 Quick-Plastic Forming

QPF was recently developed by General Motors as a hot blow-forming technology that adapted the SPF process to produce aluminum closure panels at high volumes [8]. Fig. 2.2 shows an example of the QPF forming system. The QPF process uses commercial-grade AA5083 sheets and operates at lower temperatures ($\sim 450^\circ\text{C}$) and faster strain rates ($10^{-1} \sim 10^{-3} \text{ s}^{-1}$) than traditional SPF process. Under these conditions, dislocation creep phenomena, specifically solute-drag (SD) creep, become more important and contribute significantly to deformation. [29]. It has been shown that the conditions for QPF operation produce material deformation which is controlled by both GBS and SD creep [1, 29-30]. Although the formability of AA5083 in QPF is less than in SPF, the QPF process is capable of producing complex automobile parts at remarkable rates. Several production closures have been successfully produced using this technology, including the Oldsmobile Aurora decklid, Chevrolet Malibu Maxx liftgate, and Cadillac STS decklid, with over 300,000 panels produced through the end of 2005 [8]. Comparing with SPF technology, the required cycle time for QPF has been reduced from ~ 30 minutes per part to 2–3 minutes per part [4], which make the QPF technology viable for commercial forming of complex parts in large quantities at fast production rates.

2.2 DEFORMATION MECHANISMS

There exist a variety of creep deformation mechanisms, described in great detail by Nieh et al [28], such as diffusional creep, GBS creep, dislocation creep, and etc. More than one creep mechanism can be active at the same time. If several mechanisms are independent and operating in parallel, then the steady-state creep rate is given by

$$\dot{\epsilon} = \sum \dot{\epsilon}_i \quad (2.2)$$

where $\dot{\epsilon}_i$ is the creep rate for the i th mechanism. The fastest mechanism will dominate the creep behavior. For mechanisms operating in sequence, then the steady-state creep rate is given by

$$\frac{1}{\dot{\epsilon}} = \sum \frac{1}{\dot{\epsilon}_i} \quad (2.3)$$

and the slowest mechanism will control the rate of creep deformation.

Two deformation mechanisms, GBS and SD creep, are known to govern the plastic deformation of AA5083 in hot forming processes over the strain rates and temperatures of interest for QPF [29]. GBS creep dominates deformation at slow strain rates and high temperatures, and SD creep dominates deformation at fast strain rates and low temperatures. The creep behaviors of AA5083 materials are summarized in Fig. 2.3 [1], for which the logarithm of the Zener-Hollomon parameter, Z , is plotted against the logarithm of Young's modulus compensated stress. Zener-Hollomon parameter is the normalized strain rate which accounts for the temperature dependence of diffusivity, $Z = \dot{\epsilon} \exp(Q_c/RT)$. These creep behaviors can be described by a phenomenological equation [18, 29],

$$\dot{\epsilon} = A \left(\frac{b}{d}\right)^p \left(\frac{\sigma}{E}\right)^n \exp\left(\frac{Q_c}{RT}\right) \quad (2.4)$$

where $\dot{\epsilon}$ is strain rate, A corresponds to a material constant, b is the Burgers vector, d is the grain size, p is grain size exponent, σ is the flow stress, n is the stress exponent, E is

the dynamic unrelaxed Young's modulus, Q_c is the activation energy for creep, R is the gas constant and T is the absolute temperature. The slope of data in Fig. 2.3 is equivalent to the stress exponent, n , which is the inverse of the strain rate sensitivity, i.e. $n = 1/m$ and is useful for identifying different deformation mechanisms. However, much more information is necessary to confidently identify a particular creep mechanism: activation energy, microstructure (e.g. grain-size) dependence, steady-state behaviors, creep transients, etc. In general, smaller n values mean larger resistance to necking formation and, hence, large ductility. For most fine-grained superplastic materials, a value of $n = 2$ corresponds to the region of superplastic deformation. As the value of n increases to 3 or above, the deformation mechanism changes to dislocation creep. In the case of fine-grained AA5083 with $d \approx 7 \mu\text{m}$, SD creep dominates for $\sigma/E > 3 \times 10^{-4}$ and $Z < 10^5$, while GBS creep dominates for $\sigma/E < 3 \times 10^{-4}$ and $Z > 10^5$. Both creep mechanisms are described in the following sections.

2.2.1 Grain-Boundary-Sliding Creep

Over the years, superplasticity has been investigated extensively, and a number of models for its governing mechanism have been proposed [18]. A majority of experimental evidence suggests that GBS is the dominant deformation mechanism. GBS is a process in which shear stresses at grain boundaries produce sliding of grains along their boundaries. The stress exponent, n , of GBS dominated creep deformation is typically about 2. Generally, GBS occurs at temperatures above $0.5 T_m$ and is promoted by an increase in temperature and/or a decrease in strain rate. Studies indicate that the strain due to GBS represents from only a few percent to as high as 50 percent of the total strain, depending on the material and test conditions [31]. Since the total strain is the sum of strain due to slip within grains and the strain contributed by GBS, fine-grained materials ($<10 \mu\text{m}$) can enhance superplasticity by increasing the contribution of GBS.

For any two adjacent grains in a polycrystalline material, grain boundaries cannot slide freely because they impinge on each other. Processes likely to occur during straining are grain rotation, grain boundary migration and grain switching events to accommodate and thus relax stress concentrations at grain boundaries. It is believed that the process which accommodates GBS is the rate-controlling mechanism for GBS creep deformation. The generally accepted mechanism to explain superplasticity is GBS accommodated by slip [32], which has been proposed in several models [33-36]. Such slip involves dislocation motion, including climb and glide, within grain or near grain boundaries. Fig. 2.4 presents a schematic of this mechanism [37]. Thus, GBS is rate-controlled by the accommodation process of dislocation motion.

Weertman [38] proposed a model based on dislocation motion as a sequential two-step process. The first step is dislocation glide on slip planes until meeting an obstacle; and the second step is dislocation climb by thermal activation to overcome the obstacle. Thus, the slip accommodation can be further classified into two accommodation processes, one rate-controlled by dislocation climb and one rate-controlled by dislocation glide. During creep deformation, dislocations are generated at dislocation sources, glide on slip planes and pile-up at obstacles. For dislocations to move freely again, they must climb to overcome the obstacle or to be annihilated with other dislocations of opposite sign. In dislocation climb-controlled creep, the slowest step in the two-step sequence is the climb process, which governs the creep rate. Pure metals and most solid-solutions alloys, referred as Class II alloys [39] or Class M alloys [40], deform under the mechanism of dislocation-climb creep. The second class of solid-solution alloys, referred to Class I [39] alloy or Class A [40] alloys, deform under the mechanism of dislocation-glide creep. In this case, solute interactions with gliding dislocations slows glide until it is

the slowest of the sequential processes, making it rate controlling. This deformation mechanism is also referred to as SD creep.

2.2.2 Solute-Drag Creep

SD creep is a dislocation glide-controlled creep mechanism which can occur in several solid solution alloys, including Al-Mg alloys. Weertman [41] introduced the first widely accepted mechanism for SD creep based on the idea that creep rate is controlled by interactions between dislocations and solute atoms. This mechanism specifies that dislocations attractively interact with a solute atmosphere which hinders dislocation glide. In this case, dislocation glide motion becomes the rate limiting step of creep deformation. The average dislocation velocity is controlled by the drag force from the solute atmosphere [42]. Solute-drag creep occurs when solute atoms have a significant volumetric size difference with the matrix atoms, causing strain fields that interact with dislocations in motion [41, 43-45]. The following relation describes the steady-state creep rate during solute-drag creep [41, 45],

$$\dot{\epsilon} = AD_{sol} \times \left(\frac{kT}{E}\right) \left(\frac{\sigma}{E}\right)^3 \quad (2.5)$$

where D_{sol} is the solute diffusion coefficient, k is Boltzman's constant, T is absolute temperature, E is dynamic Young's modulus and A is a material constant depending on solute concentration and the volumetric size mismatch between the solute and solvent atoms. Therefore, SD creep can be characterized with stress exponent of $n \approx 3$ and an activation energy for creep corresponding to that of solute diffusion.

Deformation under SD creep has received little attention compared to the extensive investigations of superplasticity based on the mechanism of GBS creep. This is likely due to the fact that tensile elongations obtained under SD creep conditions are generally less than under GBS creep conditions. However, forming by SD creep has two

important advantages over GBS creep in conventional SPF: 1. lower temperatures and faster strain rates are possible. 2. SD creep is independent of grain size and, thus, fine-grained microstructure is not required for the forming process. Moreover, cavitation development with strain under SD creep is slower than under GBS creep, which results in less cavitation damage in the QPF process. Details of cavitation behaviors under GBS and SD creep are described in the following sections.

2.3 FAILURE MECHANISMS

The failure of AA5083 materials was studied under conditions for which deformation is dominated by GBS [1, 46-49] and SD creep [1]. These investigations revealed that failure is controlled by the cavitation processes leading final rupture when deformation is dominated by GBS creep under conditions typical of SPF operations. On the other hand, failure has been shown to be controlled by flow localization (i.e., necking formation) when deformation is dominated by SD creep. Fig. 2.5 shows typical failure regions from AA5083 specimens tested in GBS and SD creep. Both failure mechanisms, cavitation failure and flow localization, were observed in several Al-Mg alloys when deformed under conditions of GBS and SD creep, respectively [12, 50-51]. It was shown that cavitation-controlled failure is generally associated with GBS creep deformation, while localization-controlled failure was generally observed for SD creep deformation [1]. However, both deformation mechanisms involve cavitation processes during straining but in different fashions. Examples of cavitated microstructures after deformation by GBS and SD creep are shown in Figs. 2.6(a) and (b). The difference in cavity morphology strongly depends on the deformation mechanism active during cavity development.

In general, cavitation growth rate with strain is significantly faster when deformation is controlled by GBS creep than by SD creep [1]. Even when there is no

material rupture, cavitation damage degrades mechanical properties during hot forming processes and limits the useful forming strains. It is generally considered that beyond 2 vol. pct. of cavity concentration is unacceptable for performance requirements [31].

2.4 CAVITATION BEHAVIOR

Cavitation is commonly observed during creep deformation in metallic and ceramic materials. The evolution of cavitation can be categorized into three processes: nucleation, growth and coalescence; all these processes can occur simultaneously throughout creep deformation. Experimental and theoretical studies [1, 12, 47-49, 52-56] of Al-Mg alloys found that cavitation behavior is influenced not only by external factors, such as strain, deformation mechanism and stress state, but also by microstructural features, such as grain size, intermetallic particles and other defects. Although several models have been proposed for many cavitation processes [57-63] and for overall cavitation behavior [63-64], the complex interaction of all of these parameters makes it difficult to clearly distinguish the dependence of cavitation on any one parameter.

2.4.1 Nucleation

Experimental observations suggest that cavities usually nucleate at grain boundary particles and triple points, as theoretically expected when the concentrated stress at grain boundaries cannot be relaxed sufficiently by diffusion or by dislocation motion. The precise mechanism of cavity formation during creep deformation is difficult to ascertain and is not fully understood. Some possible cavity nucleation mechanisms for Al-Mg alloys have been proposed by Khaleel et al. [65], and Bae et al. [47], as shown in Fig. 2.7 and Fig 2.8. Various models for the initiation of cavities at grain boundaries have been suggested. These generally assume that cavities are nucleated by the continuous condensation of vacancies on grain boundaries under a normal tensile stress [57] or

interfacial separation by stress concentration [49]. These models were developed for high-temperature creep of a coarse-grained microstructure at very slow creep rate and may not satisfy the deformation conditions of fine-grained superplastic materials. Some reports indicate that an initial strain is required for newly emerging cavities to appear [1, 34, 41]. Also, the number of emerging cavities is closely related to intermetallic particles. Generally, small particles require more strain to form debonding interfaces and produce new cavities. Because the population of small particles in an alloy is substantial, cavities can continue nucleate until very large strain.

2.4.2 Growth

Khaleel [65] suggests that cavitation growth may occur by: 1. diffusion of vacancies along grain boundaries into the cavity or 2. plastic deformation of surrounding matrix or 3. by a coupled diffusional and plasticity process. Diffusional growth is expected when cavity size is small. After rapid initial growth, diffusional cavity growth rate can drop significantly, and eventually plastic flow of the surrounding matrix leads to a rising growth rate. It was reported that cavity growth is mostly plasticity-controlled for superplastic material [66]. Some theoretical work has been concerned with plasticity-controlled cavity growth during superplastic flow [60-61]. These predict a relationship similar to that initially proposed by Hancock [67]. The cavity ratio under plastic-controlled growth can be express by the following equation,

$$C_v = C_0 \exp(\eta \epsilon) \quad (2.6)$$

where C_v is the cavity volume fraction, C_0 is the initial volume fraction of cavities, ϵ is true strain and η is the cavity growth rate parameter. This simple relation agrees with some experimental data. However it does not consider newly nucleated cavities, which may accelerate cavitation damage at high strains.

Diffusion and plastic flow during straining lead to cavity growth, as cavities become larger or numerous enough to interlink, failure can occur. In Al-Mg alloys, increasing strain rate was found to increase cavitation during GBS creep [52, 54]. However, a recent study indicates that cavity growth rate is dominated by deformation mechanisms rather than strain rates [1].

2.4.3 Coalescence

Failure during superplastic deformation is usually a result of cavity coalescence, where very large cavities form and across the entire specimen. Because of the difficulty in obtaining the population of cavities from experimental data, the coalescence process remains poorly documented. Nevertheless, some experimental work has been carried out on modeling cavity coalescence, but with approaches based on relatively stringent assumptions [61-62]. These models address the distribution and shape of cavities or the occurring of coalescence only when two cavities are in contact. Recently, X-ray computed tomography has been used to evaluate cavitation damage during superplastic deformation [55, 68-70]. This non-destructive technique is capable of providing three-dimensional (3-D) image data from bulk material. It is possible to develop an improved understanding of coalescence mechanisms using interrupted in-situ experiments [55, 70]. However, a synchrotron X-ray source is required to produce sufficient image resolution for detailed observation.

2.5 FILAMENTS ON THE FAILURE SURFACE

Several investigations have reported observing filaments on the order of one micrometer in diameter grow on the failure surface of aluminum alloys during superplastic deformation [1, 71-84]. In all cases, the filaments formed only on aluminum alloys tested in air, were aligned along the tensile axis and formed at failure surfaces

resulting from deformation under grain-boundary-sliding (GBS) creep, i.e. superplastic deformation. Filaments have been observed with diameters of 0.05 to 3 μm and with lengths up to 100 μm [71-73]. Previous investigations of fine-grained Al-Mg alloys indicated filament growth under GBS creep, but less or no filament growth under dislocation creep, e.g. solute-drag (SD) creep. Some investigators have reported suppression of filament formation by an inert atmosphere, such as argon or nitrogen [73-75], but only one photomicrograph of a specimen tested in argon is reported among these studies [75]. Reports of filament composition differ between investigators. Shaw [76] indicated no difference between the chemical composition of fibers and of the bulk material. Cao *et al.* [77] reported filaments of high-purity aluminum. Other investigators report high concentrations of solute elements, particularly magnesium and oxygen, in the filaments [75, 78-80]. Several mechanisms proposed for formation of these filaments have been summarized by Zelin [73] and Robinson *et al.* [79]. Those still generally under consideration by researchers include the following: 1. superplastic flow in micro-volumes [81], 2. single-crystalline plasticity [76, 82], 3. viscous flow [77, 80] and 4. oxide growth [73]. The current study investigates the possible mechanism for filament formation in AA5083 material.

Fig. 2.1: A schematic of the SPF process is shown.

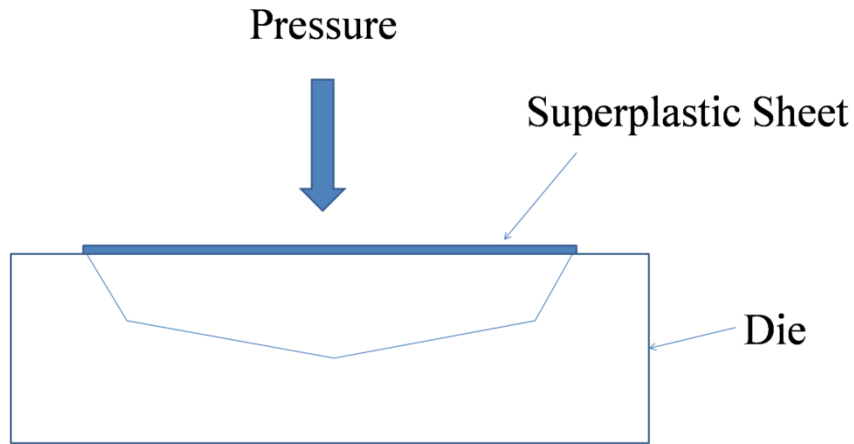


Fig. 2.2: A schematic representation of a QPF cell shows various stages in the process. Taken from [8].

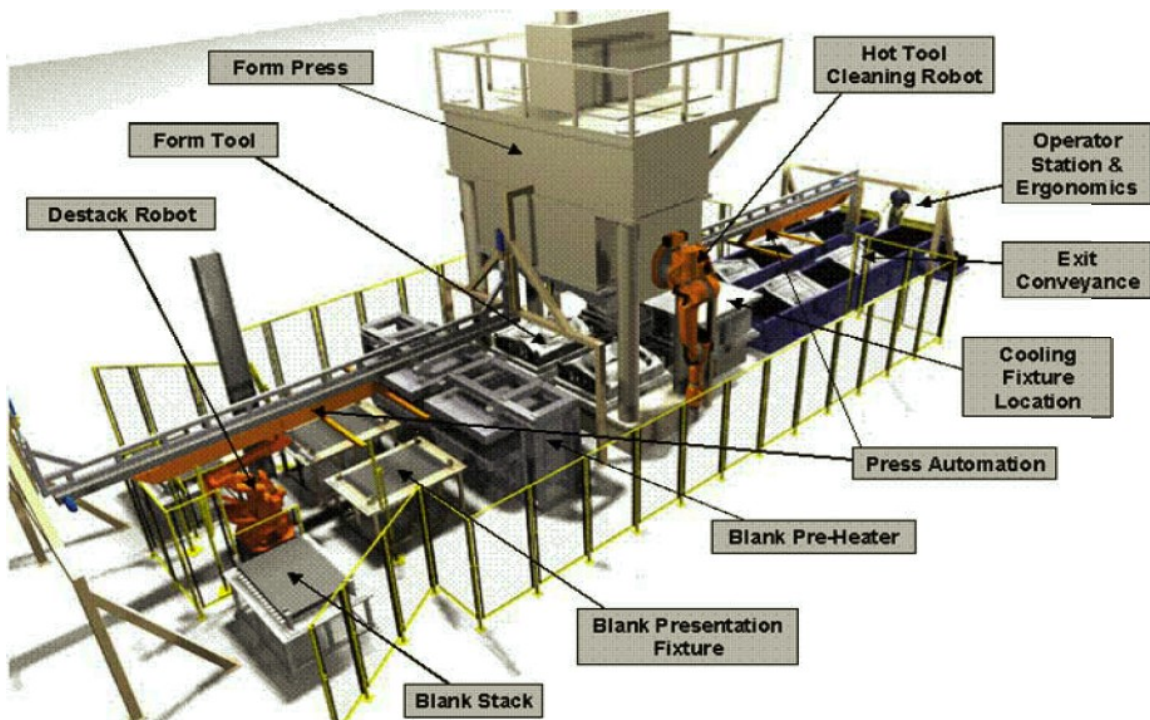


Fig. 2.3: Typical creep behavior of AA5083 materials is presented as a plot of the logarithm of Zener-Hollomon parameter against the logarithm of Young's modulus compensated stress using a single value of $Q_c = 110$ kJ/mole across both deformation mechanisms. The plot is from reference [1].

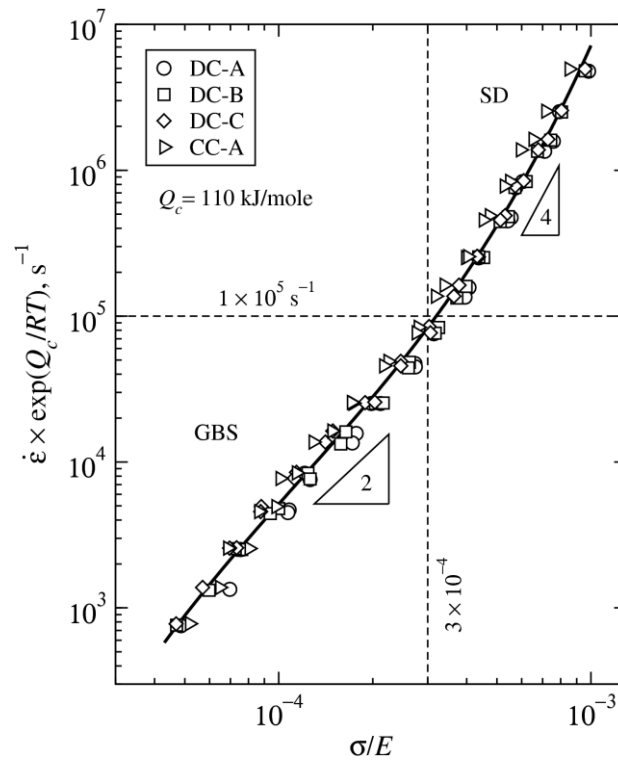


Fig. 2.4: A model is shown of grain boundary sliding accommodated by dislocation motion involving the sequential steps of glide and climb, from reference [37].

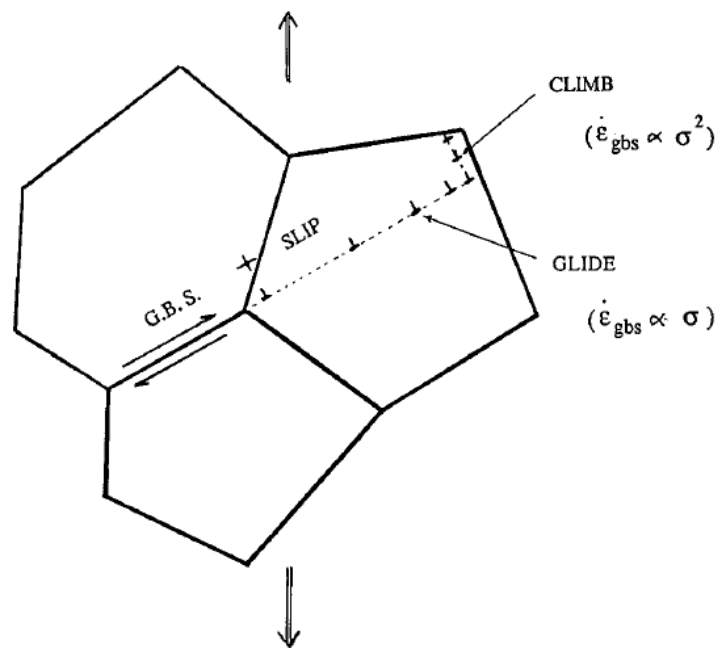


Fig. 2.5: Failure regions of AA5083 specimens are shown for (a) failure controlled by cavitation when deformation dominated by GBS creep and (b) failure controlled by flow localization when deformation dominated by SD creep. Small windows on top of each image show each specimen at lower magnification.

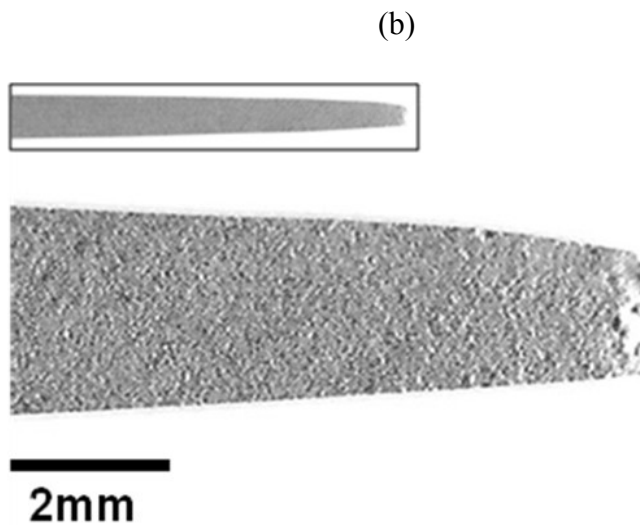
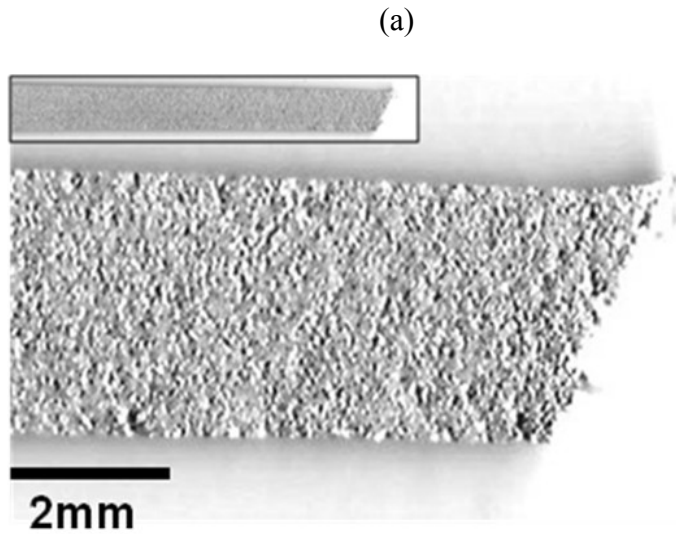


Fig. 2.6: Micrographs of AA5083 show cavity morphology under deformation by (a) GBS creep and (b) SD creep. Both the tensile axis and rolling direction are horizontal in each image.

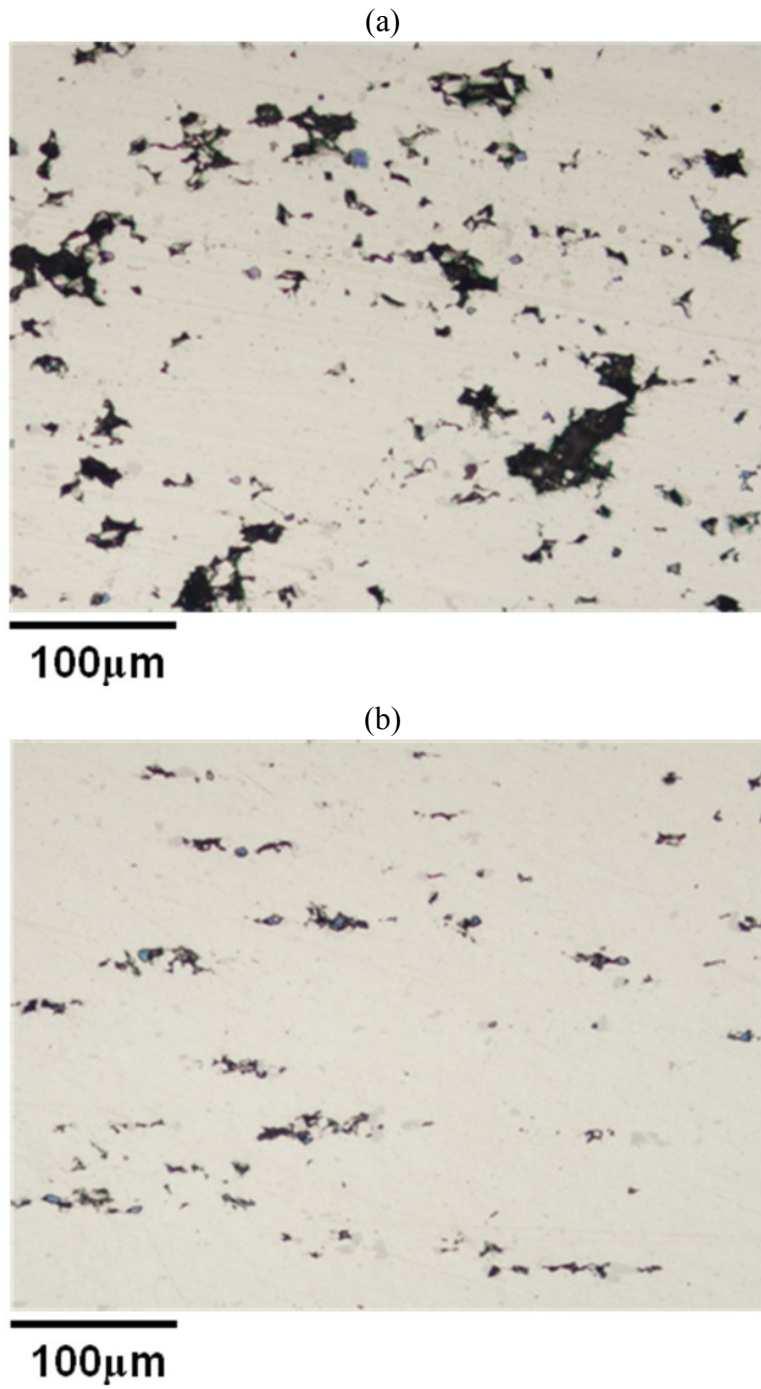


Fig. 2.7: A schematic shows possible cavitation mechanisms proposed by Khaleel et al, from reference [65].

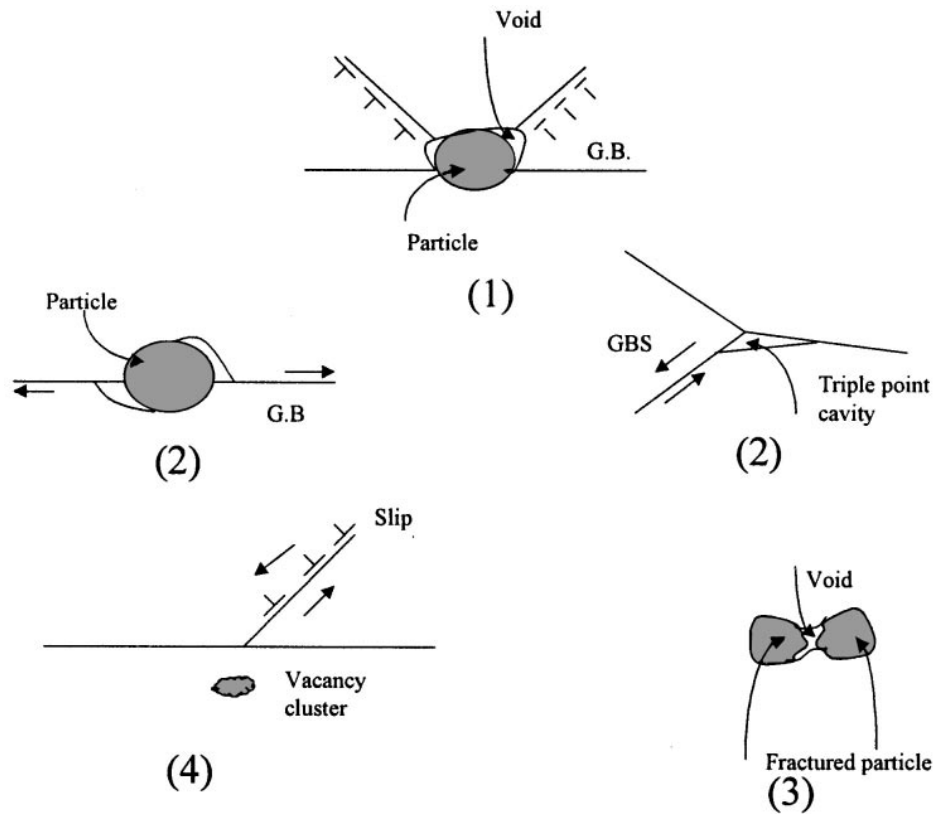
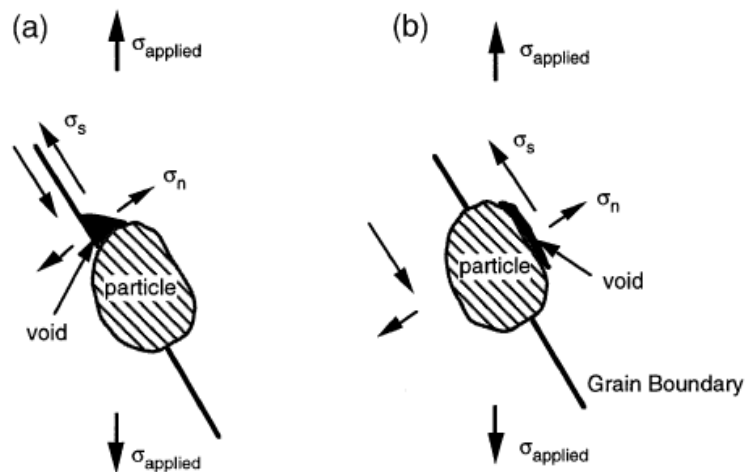


Fig. 2.8: A schematic shows possible cavitation mechanisms proposed by Bae et al, from reference [47]. Cavity nucleation and growth at (a) the particle-grain boundary interface and (b) the particle-matrix interface.



Chapter 3: Motivation of Problem and Methodology for Solution

3.1 PROBLEM STATEMENT

The evolution of cavitation in commercial aluminum material is a function of strain during the hot forming process [47-48, 85]. Recent investigations have revealed that cavity growth is approximately exponential with strain for both GBS and SD creep [1]; although the rate of cavity growth with strain for SD creep is much slower than that of GBS creep. Fig. 3.1, from a previous investigation [1], shows the evolution of cavitation with strain from four different AA5083 materials under deformation dominated by GBS or SD creep. This figure also indicates the approximate maximum acceptable cavity content, 2 vol. pct., for commercial SPF process [31]. All the AA5083 materials of Fig. 3.1 have similar chemical compositions but were produced using different processing methods. The materials labeled DC were produced by direct-chill casting, and the materials labeled CC were produced by continuous casting. The flow behaviors of all these materials are similar when tested under conditions of GBS or SD creep. However, the initiation strains for cavitation are significantly different between the AA5083 materials. For materials CC-A and DC-B, cavitation initiates at earlier strains than for DC-A and DC-C materials. As the result, the CC-A and DC-B materials fail at smaller strains. Extensive mechanical testing also indicates that CC-A and DC-B have poorer tensile ductility than materials DC-A and DC-C [1].

In order to improve the formability of AA5083 materials and to maintain acceptable mechanical properties after forming, cavitation damage must be restricted during creep deformation. Fig. 3.1 suggests that, it is possible to reduce the cavitation damage by: 1. controlling cavitation growth rate or 2. increasing the strain prior to the initiation of cavitation. For the first option, the cavitation growth rate depends only on the

dominant deformation mechanism, which is related to the forming conditions. For the second option, it is important to understand how cavities initially form in AA5083 materials. Aside from a small variation in chemical composition, the only difference between these AA5083 materials is processing history, which may lead to different microstructures.

AA5083 materials usually contain significant amounts of intermetallic particles. An example of an optical micrograph from an AA5083 material is shown in Fig. 3.2. This micrograph displays a large number of constituent particles in the material. These intermetallic particles stabilize the fine-grain microstructure, which enhances grain-boundary-sliding during SPF or QPF forming processes. From such a point of view, these intermetallic particles promote GBS creep and improve the ductility. However, many investigations indicate that intermetallic particles are closely related to cavitation which limits formability [1, 54, 87-88]. Thus, it is important to understand how cavitation evolves under different deformation mechanisms and how these intermetallic particles interact with cavities. This requires a fundamental understanding of cavity initiation and the interaction between cavities and local microstructural features.

Previous studies suggest the strong correlation between cavitation and intermetallic particles [1, 54, 87-88]. However, these data from traditional 2-D microstructure observations reveal no more than indirect evidence of this correlation. An example in Fig. 3.3 demonstrates the limitation of 2-D image observations in studying cavities and intermetallic particles. These figures were recorded from a hot-deformed AA5083 specimen in the same region at three different polished depths. Fig. 3.3(a) displays several independent cavities and an intermetallic particle. Fig. 3.3(b) shows an image of material 0.5 μm below that of Fig. 3.3(a) and reveals adjacency between the particle and a cavity. In the Fig. 3.3(c), is of material 0.5 μm below that of Fig. 3.3(b) and

shows two cavities connected to each other. These images provide an example of how 2-D observations rely on mere chance to capture interactions between cavities and particles. Because of the complex shapes of cavities, cavity-particle adjacency and cavity-cavity connectivity cannot be revealed from traditional 2-D observations. Therefore, it is necessary to use different characterization techniques, which overcome the limitations of 2-D observation, for the current investigation.

3.2 CHARACTERIZATION TECHNIQUES

To avoid the limitations of 2-D observations, 3-D characterization techniques were used to reveal the fundamental nature of microstructures. By utilizing 3-D characterization techniques, it is now possible to visualize and characterize 3-D microstructures important to processing-microstructure-property relationships. A few innovative methods have been described in literature for obtaining 3-D microstructural data. A common method used in the current study is serial-sectioning metallography. This technique was developed in the 1970s [89] and has been used extensively to study opaque materials [90-94]. The principle of this technique is to obtain detailed 3-D microstructural data from a stack of 2-D parallel sections through stereological rules. The classic serial sectioning technique includes gradual removal of material layers to obtain a series of micrographs acquired using an optical microscope or a scanning electron microscope (SEM). This technique is useful for visualization and analysis of detailed 3-D microstructural features at sufficiently high resolution. The resolution of 3-D data simply depends on the thickness of parallel sections and the resolution of 2-D photomicrographs, which makes this technique suitable for the observation of detailed interactions between cavities and intermetallic particles. However, microstructural features, such as grain boundaries, revealed after etching or other additional processes cannot be easily obtained by this technique. These processes may alter the surface morphology and change the

section thickness, which cause difficulties for obtaining unbiased images in the serial sectioning technique. Equipment required for serial sectioning is relatively common in many metallography laboratories, but obtaining 3-D microstructural data involves routine and time-consuming processes. Although an automated robot designed for serial sectioning has been developed recently [95], the reconstruction of large volumes of microstructural data still remains a challenge for this technique.

Another method to obtain detailed 3-D microstructural data is ultra-high-resolution x-ray computed tomography. This technique uses an x-ray diffraction microscope for fast and non-destructive characterization of microstructure inside bulk materials. In this method, a high-energy x-ray beam generated by a synchrotron source passes through a rotating specimen and creates diffraction patterns at many angles. These diffraction patterns are stored and reconstructed by utilizing a computer to generate 2-D computed tomography images. By stacking a series of such 2-D images, one can obtain 3-D microstructure data. This technique is ideal for characterizing individual grains, crystal orientation, and strain inside materials [96]. Although this technique is undoubtedly promising, particularly with recent advances in x-ray source and detector technologies, high-resolution computed tomography systems, such as the one in European Synchrotron Radiation Facility, are so far capable of achieving spatial resolution only about 5 μm [96-97]. Such spatial resolution is not sufficient for the current investigation to reveal the details of cavities and intermetallic particles. Therefore, taken together, serial-sectioning metallography is considered the best currently available 3-D characterization technique for revealing detailed microstructural features in hot-deformed AA5083 material.

Some consider the statistical analysis of large 2-D data sets to be a potential alternate to analysis of 3-D data sets. The most common statistical method for

microstructure analysis is the two-point correlation function which can be used to represent the relationships between microstructural features in 2-D metallographic data [33-37]. The two-point correlation function is a mathematical representation of the probability that a particular object exists at a specific distance and along a specific direction from a chosen location. Analyses of two-point correlation functions can provide quantitative correlation between microstructural features, such as a correlation between cavities and intermetallic particles. The potential and the limitation of two-point correlation functions are further explored in this investigation.

3.3 DESIGN OF EXPERIMENT

The goal of current investigation is to understand the effects of microstructural features and deformation mechanisms on the evolution of cavitation in fine-grained AA5083 sheet under GBS and SD creep deformation. With this purpose, microstructures produced in fine-grained AA5083 sheet by deformation under GBS creep and SD creep should ideally be compared at: 1. identical true strains and 2. identical cavity fractions. The “good” material, AA5083 DC-C, was used for the current investigation because data on cavitation at large strains are available for this material. It is known from previous investigations [1, 13, 29] that each deformation mechanism, ie. GBS and SD creep, can be produced at 450 °C simply by applying different strain rates. Thus, temperature was kept constant at 450 °C and strain rates were chosen, based upon prior experimental data [1, 13, 29], to be $3 \times 10^{-4} \text{ s}^{-1}$ to produce deformation dominated by GBS creep and $3 \times 10^{-2} \text{ s}^{-1}$ to produce deformation dominated by SD creep. Previous results for DC-C material on the evolution of cavity area fraction with strain under each of these test conditions [1], shown in Fig. 3.4, served as a guide in designing experiments for this investigation. The maximum true strain under uniaxial tension for the GBS test condition is approximately 1.3, as measured from local area reduction. The cavity area fraction at this strain, shown

by point A in Fig. 3.4, is predicted to be approximately 10%. For this same local strain, the SD test condition will produce a cavity area fraction of approximately 1.2%, as shown by point B in Fig. 3.4. Thus, points A and B represent two test conditions which can produce specimens with identical local true strains, but different cavity contents because of deformation controlled by two different mechanisms. In order to determine a third test condition which produces the same cavity fraction as that at point B, but under GBS creep deformation, a horizontal line was drawn in Fig. 3.4 from point B. That horizontal line intersects the GBS data line at point C. Point C occurs at a true strain of approximately 0.9. Thus, points A, B and C in Fig. 3.4 represent the three test conditions chosen to produce specimens for microstructure observations.

Fig. 3.1: Trends from data in Ref. [1] are shown. The logarithm of measured cavity area fraction is plotted against true strain measured from reduction in area for AA5083 materials tested under GBS and SD creep.

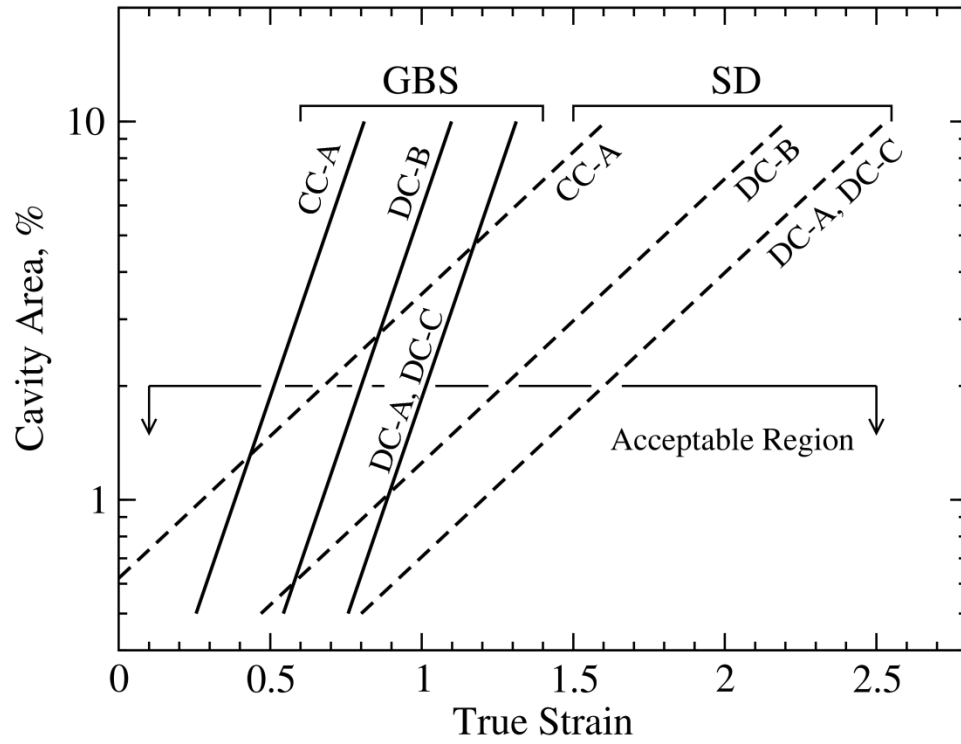


Fig. 3.2: An optical photomicrograph of as-polished AA5083 material is shown. Intermetallic particles in the micrograph are black in color.

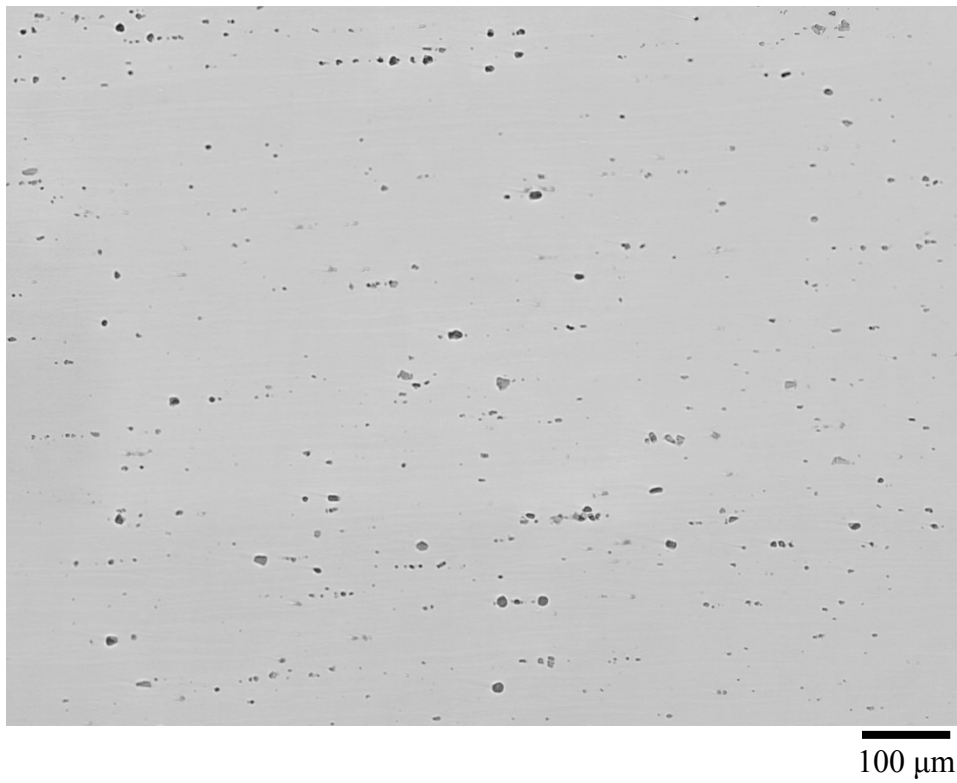


Fig. 3.3: These figures demonstrate why cavity-cavity connectivity and cavity-particle adjacency cannot be determined from 2-D sections.

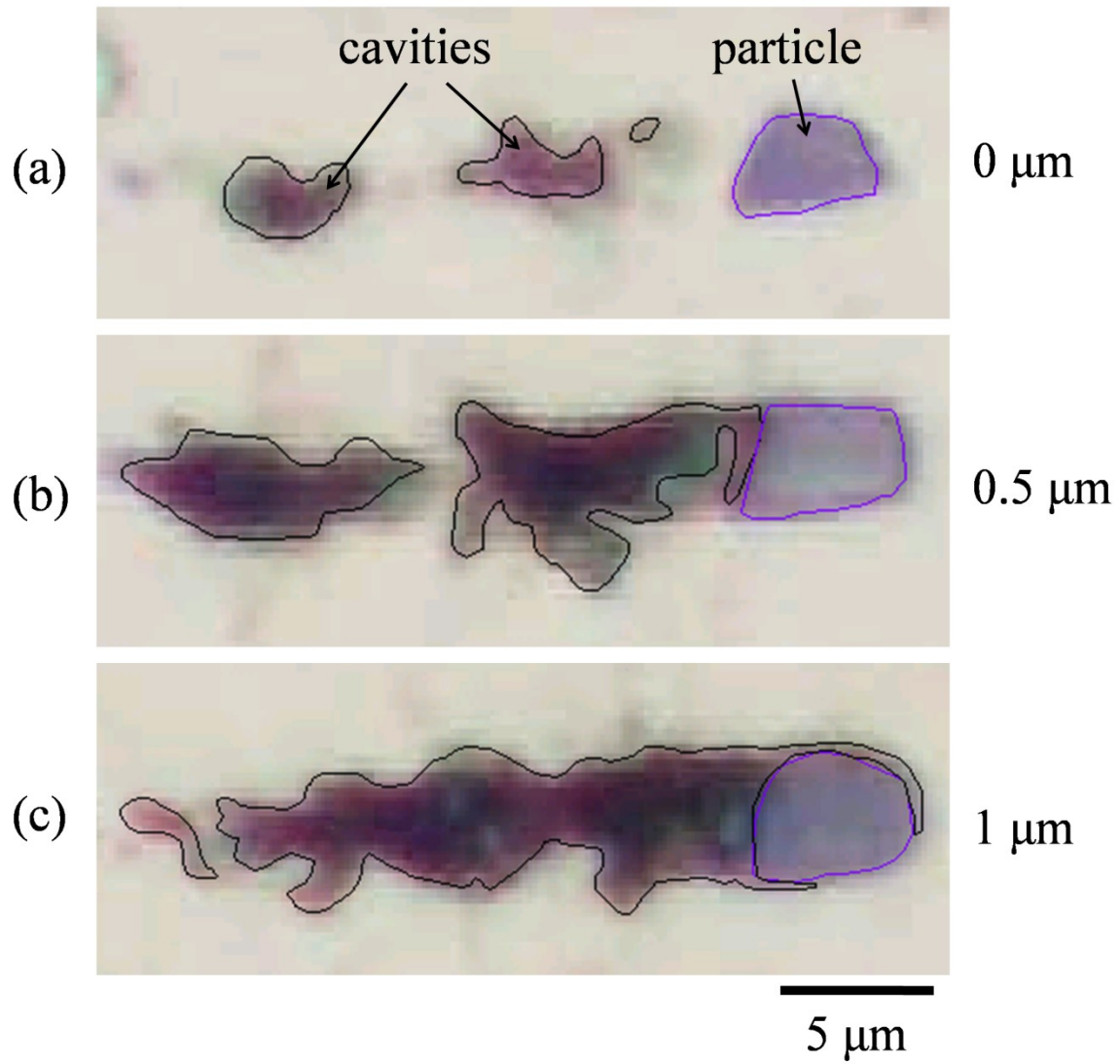
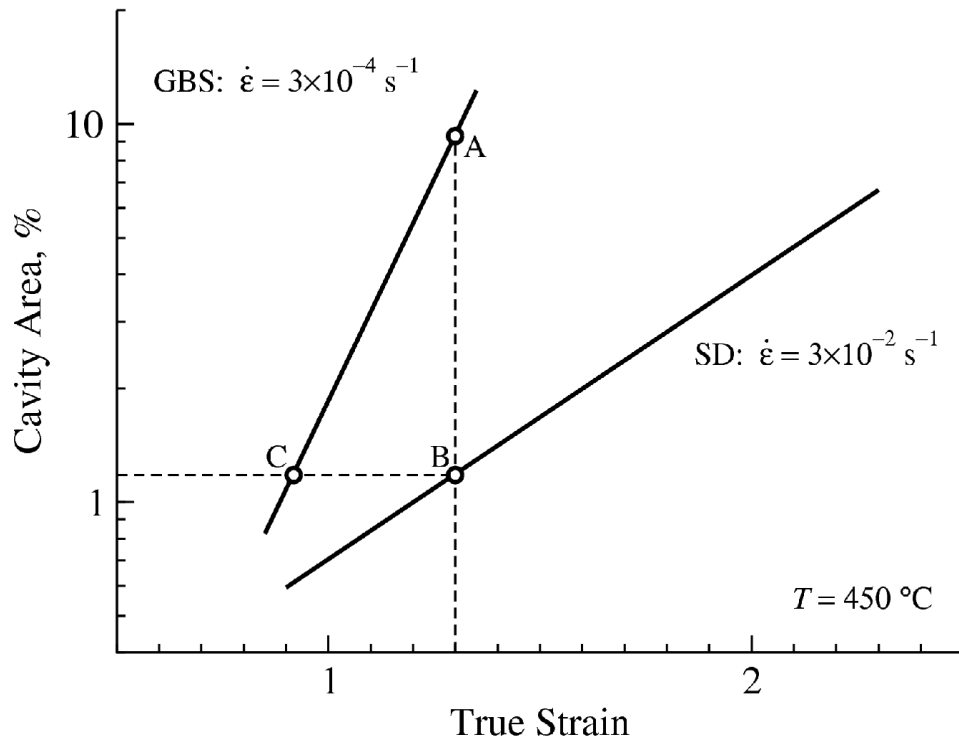


Fig. 3.4: Trends from data in Ref. [1] for cavity fraction as a function of tensile straining are shown for a test temperature of 450°C and true strain rates which produce deformation controlled by GBS creep ($3 \times 10^{-4} \text{ s}^{-1}$) and SD creep ($3 \times 10^{-2} \text{ s}^{-1}$). Points A, B and C represent the three mechanical testing conditions chosen for investigation.



Chapter 4: Experimental Procedures

4.1 MATERIALS

A fine-grained AA5083 sheet material was studied in this investigation. This is the same as material DC-C studied previously in references [1, 29]. This sheet material, produced by Pechiney Rolled Products of Ravenswood, West Virginia, was hot- and cold-rolled from an homogenized, direct-chill casting to a final thickness of 1.2 mm and an approximately H18 temper [98-99]. Table 4.1 shows the chemical composition of the AA5083 sheet provided by the supplier. The chemical composition was also verified using energy dispersive spectroscopy (EDS) of polished specimens. After recrystallization, which occurs rapidly at 450 °C, the lineal intercept grain size was measured, in accord with ASTM E 112-96 [5], to be 6.5 μm . This microstructure is resistant to static grain growth at temperatures of 500°C or lower [29].

4.2 HIGH-TEMPERATURE MECHANICAL TESTS

High temperature uniaxial-tensile tests were conducted on the AA5083 sheet material. Tensile coupons were machined from the as-received sheet, with the tensile axis parallel to the rolling direction, and were tested in tension at 450 °C. Tensile coupons were dog-bone shaped and had a gage length of 25.4 mm, gage width of 6.0 mm, grip shoulder radius of 7.9 mm and thickness of 1.2 mm. Fig. 4.1(a) presents the geometry of the tensile coupons. Coupons were held in shoulder-loading quick-attach grips, which effectively restricted deformation to the specimen gage region. The quick-attach grips allow testing coupons while maintaining optimal alignment along the tensile direction during testing and quick exchange of coupons between tests. Fig. 4.2 shows a photograph of this fixture. Temperature was controlled to within ± 1.5 °C along the entire specimen

gage length, as measured from multiple type-K thermocouples, using a three-zone resistance furnace. Both a screw-driven electro-mechanical testing frame and a servo-hydraulic testing frame were used for tensile testing. Both testing frames were computer-controlled and used computerized data acquisition. Fig. 4.3 shows the testing frames used for high-temperature mechanical tests. Tensile tests were conducted by controlling displacement as a function of time, with several different displacement rates imposed in sequential steps to simulate a constant true-strain rate. Tensile tests were conducted to failure or until a particular desired elongation was achieved. Two tensile tests were conducted to failure at 450 °C, one at a true-strain rate of $3 \times 10^{-2} \text{ s}^{-1}$ and the other at $3 \times 10^{-4} \text{ s}^{-1}$. A third tensile test at 450 °C and $3 \times 10^{-4} \text{ s}^{-1}$ was conducted to a total elongation of 146%. Specimens for metallographic examination were sectioned from tested coupons, as represented in Fig. 4.4. Specific locations from which to remove metallographic specimens were determined from local true strains calculated using measurements of area reduction along the gage length of each specimen. Metallographic specimens were removed from regions of tested coupons with local strains as indicated in Table 4.2.

4.3 ELONGATION-TO-FAILURE TESTS IN AIR AND IN VACUUM

Elongation-to-failure tests were performed in air and in vacuum using tensile coupons with two dog-bone geometries for different testing frames and furnaces. Coupons for both tests used the as-received thickness of 1.2 mm and were oriented with the rolling direction parallel to the tensile axis. Coupons tested in air had a gage length of 25.4 mm and a gage width 6 mm (Fig. 4.1(a)). Coupons tested in vacuum had a gage length 15.24 mm and a gage width 6.35 mm (Fig. 4.1(b)). The shorter gage length was used to match the specimen size and position to the vacuum furnace hot zone with the least temperature variation. Testing frames used for air and vacuum test are shown in Figs. 4.3(b) and (c). Specimens were subjected to elongation-to-failure tests at a

temperature of 500°C and a true strain rate of $3 \times 10^{-5} \text{ s}^{-1}$. These test conditions were previously shown to produce deformation by GBS creep in this material, which corresponds with the observation of filament production [1, 29, 84]. Tests in air used a computer-controlled, servo-hydraulic testing frame and a resistance furnace with three independent heating zones. Temperature was monitored at each end of the gage length using type-K thermocouples and was controlled to within $\pm 2^\circ\text{C}$ along the entire gage length during the test. Tests in vacuum used a computer-controlled, screw-driven, electromechanical testing system and a high-temperature vacuum furnace with tungsten heating elements. Temperature was controlled to within approximately $\pm 15^\circ\text{C}$ along the entire gage length during the test. Temperature variation within the vacuum furnace was determined by profiling the hot-zone with a type-K thermocouple, and these data were used to determine specimen gage length and location for testing. All tests utilized a constant true-strain rate by using a computer to control fixture speed in real time during tensile elongation. Specimens tested in vacuum were cleaned with acetone and dried prior to installation in the vacuum furnace. The vacuum chamber was purged with argon and pumped down to 2.6×10^{-6} Torr before testing.

4.4 FAILURE SURFACE CHARACTERIZATION

Elongation-to-failure specimens tested in air and in vacuum were examined in a scanning electron microscope (SEM), JEOL™ JSM 5610, to observe surface morphologies. Sections of the deformed gage regions of tensile specimens were analyzed. Chemical composition of specimen surfaces was analyzed using EDS, Oxford™ INCA200 EDS detector. As-received and deformed specimens tested in different environments were examined using EDS with an electron beam energy of 20keV and a scan area of 0.18mm^2 . Specimen surfaces were analyzed after deformation using EDS to measure differences in surface chemical composition following testing in air and in

vacuum. Filaments formed during testing in air with average diameters of 1 to 2 μm were characterized with EDS at a reduced electron beam energy of 10 keV to avoid X-ray signals generated from background material, i.e. to avoid electron beam penetration through the filament. EDS calibration for 10keV was conducted by comparing spectra taken at 10 keV and the standard 20 keV from polished AA5083 base material and an Al_2O_3 powder reference.

4.5 SERIAL SECTIONING METALLOGRAPHY

Serial sectioning metallography is a technique for obtaining three-dimensional (3-D) microstructural data from two-dimensional (2-D) sections. The serial sectioning technique involves serial steps of material removal and image acquisition to collect digital 2-D microstructure images. Once 2-D images were cropped, aligned and stacked to produce a 3-D data set, 3-D microstructure reconstructions were analyzed quantitatively and qualitatively. Fig. 4.5 shows the flow chart of the serial sectioning process in this study. The detailed serial sectioning processes are described in the following section.

4.5.1 Sample Preparation

To characterize hot-deformed AA5083 specimens using the serial sectioning technique, it is important to define the representative volume for analysis. The proper representative volume is based on the size of microstructural features and computational capability [100]. In this study, it was desired to obtain several intermetallic particles and cavities with sufficient resolution for quantitative analysis in the volume. Since the average intermetallic particle size is less than 8 μm in diameter, and most cavities are less than 10 μm in diameter, it was determined that a $540\ \mu\text{m} \times 360\ \mu\text{m} \times 25$ (thickness) μm volume would yield a representative group of intermetallic particles and cavities for

analysis. Fifty (50) sections, with each section 0.5 μm in thickness, would provide sufficient microstructure detail for analysis.

Specimens for serial-sectioning were sectioned from deformed gage regions of tested coupons after testing at 450°C. Each specimen was selected within a specific local true strain measured from the cross-section reduction in area. According to the design of experiment, specimens with local true strain 1.3 for both GBS and SD creep tested coupons were sectioned, and a specimen with local true strain of 0.9 for GBS creep was sectioned. Metallographic specimens were mounted on individual stainless steel polishing fixtures using a hot-melt wax adhesive with the sheet normal direction normal to the mounting surface. The tensile axis of each specimen was oriented along a known, marked direction. Each specimen was ground flat and parallel to the fixture using SiC abrasive.

Three Vickers hardness indentations were then placed in each specimen to act as fiduciary marks during serial polishing [90, 93-94]. The observation areas of each specimen were located within the center of the three indentations. Indentations were used to measure the material thickness loss during the polishing process as well as image alignment of successive parallel sections for 3-D reconstruction. The material thickness loss was calculated from measurements of the indentation diagonal length based on the geometry of the Vickers indenter. Fig. 4.6 shows the geometry of the Vickers diamond indenter. The indenter forms a pyramidal mark on the specimens' surface with depth (h), edge length (l) and diagonal length (d). The depth of the indentation (h) is given by,

$$h = \frac{d}{2\sqrt{2} \tan(\theta/2)} \quad , \quad (4.1)$$

where θ is the Vickers indenter's apex angle (taken as 135°). From this equation, the ratio of the diagonal length (d) to the depth of the indent (h) is approximately 7:1. Thus, the depth can be determined from the average of the two diagonals. A proper load is required

to produce an indentation with desired dimensions. Small indentation marks may record fewer parallel sections, whereas very large indentation marks may contain distortions which alter the depth measurement. With the intention of producing 50 sections that span a 25 μm depth for each specimen, a load of 5 kg for 15 seconds was applied to create indentation marks about 380 μm in diagonal length and 54 μm in depth. Such indentations are able to serve as fiduciary marks throughout serial polishing.

All observations in the optical microscope were made viewing along the sheet normal direction with the tensile axis horizontal. Specimens were polished to a final finish with 1 μm diamond abrasive prior to serial polishing. Fifty (50) serial polishing sections were made for each specimen by polishing with 1 μm diamond abrasive using an Allied High Tech MultiPrep™ polishing system as shown in Fig. 4.7. The 1 μm diamond abrasive was chosen for serial polishing because of the reasonable material removal rates and the acceptable surface quality after polishing. This polishing system uses a digital thickness gauge to monitor the material removal during polishing, which provides precise control of the desired section depth. Material removal rate, approximate 0.2 μm per minute in the current study, was calculated from the average thickness loss during polishing. Each polishing cycle was 2.5 minutes and aimed to remove 0.5 μm of material thickness. The actual material loss after polishing was examined by measuring diagonals of Vickers indentations using an optical microscope. Specimens were re-polished until the desired section depths were achieved. The average section depth for all data sets was about 0.5 μm , and the depth of individual sections removed was controlled to within $\pm 0.2 \mu\text{m}$.

4.5.2 Image Acquisition

Digitized images were acquired from each polished section using an optical microscope at a magnification of 200 \times . Aluminum matrix, cavity, and two types of

intermetallic particles are easy to distinguish from these optical photographs. An example of a 2-D microstructure image is shown in Fig. 4.8. Each section was held parallel to within the resolution for measuring parallelism from the change in Vickers indentation features during polishing. Digitized images were aligned to fiduciary marks and cropped to $540 \times 360 \mu\text{m}$, represented as 3000×2000 pixels, in image processing software. These processed images were then stacked for further 3-D microstructure reconstruction.

4.5.3 Microstructure Reconstruction

Microstructures in serial sections were traced and placed together using the Reconstruct [101] software package to generate 3-D models. This software transforms all traced microstructure data into a Cartesian coordinate system and provides 3-D visualization for detailed analysis. Fig. 4.9 shows an example of 3-D microstructure reconstructions with detailed interaction between a cavity and two different types of intermetallic particles. Each 3-D data set was $540 \times 360 \times 25 \mu\text{m}$ in size and contained fifty serial section planes. Four (4) distinct phases are represented in each 3-D data set: 1. Al matrix, 2. cavity, 3. $\text{Al}_6(\text{Mn,Fe})$ intermetallic and 4. Mg-Si intermetallic. The two intermetallic particle types are easily distinguished in optical photomicrographs of polished, unetched specimens, as shown in Fig. 4.8. $\text{Al}_6(\text{Mn,Fe})$ intermetallic particles, common to 5000-series alloys, appear as a gray color different from that of the Al matrix. The Mg-Si intermetallic particles have a light blue tint. These identifications were confirmed with energy dispersive spectroscopy (EDS) in a JEOL™ JSM 5610 SEM with an Oxford™ INCA200 EDS detector. The EDS mappings of the two intermetallic particles are shown in Fig. 4.10 and 4.11. Note that the specific stoichiometry of the Mg-Si intermetallic particles was not determined in this study, but other investigators have most commonly observed Mg_2Si [20, 23-24], with some reports of more complex chemistries [21, 25].

4.6 TWO-POINT CORRELATION ANALYSIS

Mechanical and physical properties of materials are generally affected by microstructural features (particle, cavity, grain etc.), their morphologies (size, shape, surface area, etc.) and location. The distribution of relative locations of microstructural feature is important to spatial patterns, correlation, clustering and texture. Statistical description of the distribution of material microstructures is a mathematical approach to understanding microstructure formation [102-103]. One of the most common statistical methods for material characterization is the TCF, representing the spatial distribution of microstructural features. Statistical correlation functions have been developed for a few decades to quantify spatial characterization of random microstructures [104]. These distribution functions are useful in computation of mechanical and physical properties of heterogeneous materials [105-106]. The most important microstructural features investigated in the current study are cavities and intermetallic particles. Revealing the relationship between the spatial distribution of microstructural features and failure mechanisms in the AA5083 alloy is important to understand formability.

4.6.1 Computation of Two-Point Correlation Functions

Consider a microstructure containing two phases, namely phase-1 and phase-2. Phase-1 and phase-2 may be particle, cavity, matrix, etc. In the current study, the two-point correlation function $P_{ij}(r, \theta, \varphi)$ can be defined as the probability that a particular object (j) exists at a specific distance (r) and specific angular orientations (θ, φ) from a chosen location (i) [107-108]. The orientation averaged two-point correlation functions $\langle P_{ij}(r) \rangle$ can be calculated from the corresponding direction dependent functions $P_{ij}(r, \theta, \varphi)$ using the following equation [105].

$$\langle P_{ij}(r) \rangle = \frac{1}{2\pi} \int_0^{2\pi} \int_0^{\pi/2} P_{ij}(r, \theta, \varphi) \sin \theta d\theta d\varphi$$

Thus, $\langle P_{11}(r) \rangle$ is defined as the average probability that both ends of a randomly located straight line (with length r) are contained in phase-1. Similarly, $\langle P_{12}(r) \rangle$ is the average probability of a randomly located straight line (with length r) that has a first end contained in phase-1 and a second end contained in phase-2. Therefore, there are four possible orientation averaged two-point correlation functions, $\langle P_{11}(r) \rangle$, $\langle P_{12}(r) \rangle$, $\langle P_{21}(r) \rangle$ and $\langle P_{22}(r) \rangle$, in a two-phase microstructure. However, only one of the four two-point correlation functions is independent based on the following relationships [105, 109].

$$\langle P_{11}(r) \rangle + \langle P_{12}(r) \rangle + \langle P_{21}(r) \rangle + \langle P_{22}(r) \rangle = 1, \quad (4.3)$$

$$\langle P_{12}(r) \rangle = \langle P_{21}(r) \rangle, \quad (4.4)$$

$$\langle P_{11}(r) \rangle + \langle P_{12}(r) \rangle = f_1, \quad (4.5)$$

$$\langle P_{21}(r) \rangle + \langle P_{22}(r) \rangle = 1 - f_1. \quad (4.6)$$

Eq. (4.3) states that the sum of all possibility is equal to unity. In Eq. (4.5), f_1 is the volume fraction of phase-1. Eq. (4.5) arises from the fact that the probability of all two-point correlation functions whose first end falls in phase-1 is equal to the volume fraction of phase-1. Similarly in Eq. (4.6), the probability of all two-point correlation functions whose first end falls in phase-2 is equal to the volume fraction of phase-2, or $1 - f_1$. Note that the Eq. (4.3) can be obtained from adding Eqs. (4.5) and (4.6), and therefore, it is not an independent constraint. The following well-know limits exist for the two-point correlation functions when the value of r approaches zero.

$$\lim_{r \rightarrow 0} \langle P_{11}(r) \rangle = f_1, \quad (4.7)$$

$$\lim_{r \rightarrow 0} \langle P_{12}(r) \rangle = 0. \quad (4.8)$$

In addition, the following limits exist for random microstructures as r approaches infinity.

$$\lim_{r \rightarrow \infty} \langle P_{11}(r) \rangle = [f_1]^2, \quad (4.9)$$

$$\lim_{r \rightarrow \infty} \langle P_{12}(r) \rangle = [f_1][f_2]. \quad (4.10)$$

The two-point correlation function formalism can be extended to an n-phase microstructure in a straightforward manner. In an AA5083 microstructure, there are four phases included in the current analysis. They are (1) Al matrix, (2) cavity, (3) particle $\text{Al}_6(\text{Mn,Fe})$ and (4) particle Mg-Si. The two-point correlation functions $P_{ij}(r, \theta, \varphi)$ can be simplified to $P_{ij}(r, \theta)$ as these two-point correlation functions were analyzed from 2-D sections, and therefore, only one orientation (θ) is considered in the current study. In such a case, the two-point correlation function $P_{ij}(r, \theta)$ is the probability that a straight line (length r) with angular orientation (θ) randomly placed in a 2-D microstructure has its first end in phase- i (where $i = 1$, or 2, or 3, or 4) and second end in phase- j (where $j = 1$, or 2, or 3, or 4). Obviously, there are sixteen (16) two-point correlation functions for a 4-phase microstructure. However, not all of these two-point correlation functions are independent due to the following relationships.

$$\sum_{i=1}^n \sum_{j=1}^n P_{ij}(r, \theta) = 1, \quad (4.11)$$

$$\sum_{j=1}^n P_{ij}(r, \theta) = f_i, \quad (4.12)$$

$$P_{ij}(r, \theta) = P_{ji}(r, \theta). \quad (4.13)$$

For a 4-phase AA5083 microstructure, Eq. (4.11) and Eq. (4.12) represent 4 relationships, and Eq. (4.13) represents 6 relationships. Therefore, only 6 independent two-point correlation functions occur for the current analysis.

These two-point correlation functions were analyzed from feature profiles of selected serial sections for each 3-D data set. Additional image processing is required for the analysis of these images. First, digital images were exported from traced profiles of serial sections using the software package “Reconstruct” [101]. Each microstructural

feature in these images was given a specific color for phase identification. These images then were converted to PGM format, a grayscale graphic image similar to an array of arbitrary integers, using “ImageJ” software [110]. Finally, all microstructural features were re-coded with specific gray values so that Al matrix coded as “1”, cavity coded as “2”, Al₆(Mn,Fe) coded as “3” and Mg-Si coded as “4”. Each image is 3000 × 2000 pixels in size, corresponding area of 540 μm × 360 μm, with 0.18 μm per pixel resolution where all features of interest are clearly resolved.

To compute two-point correlation functions for microstructural features, the re-coded PGM files were analyzed using a custom program written in Mathematica™ [111]. The detailed custom program for this analysis is documented in the appendix. The basic algorithm for calculating two-point correlation functions is described as follows. The program reads grayscale PGM files and asks the user for inputs of the image size to be analyzed and the maximum measurement distance (r_{\max}) to be measured. Based on the input information, the program defines a virtual rectangle “measurement frame” inside the analyzed image and a $r_{\max} \times r_{\max}$ transportable analysis array for computing two-point correlation functions. The measurement frame is at least r_{\max} distance from the nearest edge of the analyzed image. Fig. 4.12 shows the image analysis geometry and the concept of two-point correlation function calculation. Once the measurement frame is defined, the program goes to the next step to calculate two-point correlation functions and allocates their variables P_{ij} , as $r_{\max} \times r_{\max}$ arrays. Starting from the first point of the measurement frame, the program applies the transportable analysis array on the measurement frame so that the center of the transportable analysis array, referred to as the base point, is on the first point. The digital value of the base point on the analyzed image is read and used to identify the first suffix, i , of the two-point correlation functions. After the first suffix of P_{ij} is determined, all other points in the transportable analysis

array are read to determine the second suffix, j , and the results are stored in the corresponding location of P_{ij} variables. For example, if the gray value of the base point is “1” and all other points in the transportable analysis array are “2”, then the results are $p_{11} = 1$ in the center and $p_{12} = 1$ in all other positions, where the p_{11} and p_{12} are the individual two-point correlation functions in the transportable analysis array and are stored in variable array P_{11} and P_{12} respectively. The values of p_{11} and p_{12} represent the event for the specific location in the transportable analysis array, and that value is equal to one when correlation exists, or is equal to zero for no correlation. These results are then stored in the variables P_{11} and P_{12} according to the corresponding position in the transportable analysis array. Once all points in the transportable analysis array have been analyzed and recorded, the base point moves to the next point in the measurement frame and repeats the same process. This process is repeated until the base point passes through all the area and moves to the last point in the measurement frame. Finally, the resulting variables P_{ij} count all events in the analyzed image. Two-point correlation functions are then calculated from these variables, P_{ij} , by dividing by the number of pixels in the measurement frame, so that each element in a variable represents the probability in percentage at the specific location. Therefore, each calculated $\langle P_{ij} \rangle$ array can represent a two-point correlation function with all angular orientations (θ) and distances (r) in a $r_{\max} \times r_{\max}$ square area.

The principle of two-point correlation function methodology used in the current investigation is illustrated as a series of schematic diagrams in Fig. 4.13. In this demonstration, a 9×9 pixel grid of a two-phase (A and B) microstructure is shown in Fig. 4.13(a). This grid is analyzed using a two-point correlation function $\langle P_{AA} \rangle$. First, a proper measurement distance (r) is chosen, say 2 pixels in distance, and a virtual 5×5 transportable analysis array and a virtual rectangle measurement frame are defined in the

image; see Fig. 4.13(b). This step ensures all analyses in the transportable analysis array are within the image by restricting the array to move only inside the measurement frame. When calculating the two-point correlation function, the center point of the array, referred to as the base point, represents the first object of the pair correlation (i) and all other points in the array represent the second object of the pair correlation (j). As shown in Fig. 4.13(c), the unit in the array is reported as “1” if the P_{AA} correlation exists or “0” if it does not exist. Next, the transportable array moves to the next point in the measured frame and analyzes and updates the result calculated in the new area, as shown in Fig. 4.13(d). It is of note that if the base point is not on the phase-A, then there is no P_{AA} correlation in this area, as shown in Fig. 4.13(e). When the base point moves to the last point in the measurement frame, shown in Fig. 4.13(f), the two-point correlation function $\langle P_{AA} \rangle$ can be calculated from the transportable analysis array. Fig. 4.14 gives an example describing the two-point correlation function from the array in Fig. 4.13(f) in two different ways: 1. it can report the probability in percentage, and 2. it can report the probability by normalizing to the random correlation. To calculate the percentage of probabilities, each value in the array is divided by the value of the base point, where the self correlation probability of the base point was always 100% in $\langle P_{AA} \rangle$. To calculate the normalized correlation, each value in the array is divided by the average value in the array, thus setting the value of random correlation to unity. Each calculation type provides different information. Contour plots are used to display results of two-point correlation functions between microstructural features, where the center of the contour plots stands for the first point (i) and all other points in the contour plot represent for the second point (j). Hence, a contour plot can display probabilities of finding a second object around the center object in a 2-D sense.

4.6.2 Representing Two-Point Correlation Functions

A convenient way to represent two-point correlation functions from calculated $\langle P_{ij} \rangle$ arrays is using contour plots. Examples of contour plots are shown in Fig. 4.15. These $\text{Al}_6(\text{Mn,Fe})$ cavity contour plots show the average probability of finding a cavity around an $\text{Al}_6(\text{Mn,Fe})$ particle in a $27 \times 27 \mu\text{m}^2$ area. Each contour line in these plots has the same probability calculated from the $\langle P_{\text{Al}_6(\text{Mn,Fe})\text{-cavity}} \rangle$ two-point correlation function. Numbers shown on the contours of Fig. 4.15(a) are probabilities in percent. Dashed contours represent locations of completely random correlation, i.e. no meaningful correlation between objects, which were calculated by averaging the probabilities at all locations. The dashed contour is, thus, a value of unity for the normalized two-point correlation function, i.e. $\langle P_{ij} \rangle = 1$. Because the random levels are different in all correlation functions, the random probability is normalized before comparing with other similar contours plots. Fig. 4.15(b) shows the normalized $\text{Al}_6(\text{Mn,Fe})$ cavity contour plot. The value represents the normalized probability of finding a cavity around a $\text{Al}_6(\text{Mn,Fe})$ particle. Values above “1” indicate a higher probability of finding a cavity than the random level.

Table 4.1: Composition of the AA5083 material in weight percent.

Element	Mg	Mn	Fe	Si	Cu	Al
wt. %	4.50	0.76	0.20	0.15	0.03	Bal.

Table 4.2: Test true-strain rate ($\dot{\epsilon}$) at 450°C, number of cavities, cavity volume fraction and average individual cavity volume measured from the three 3-D data sets.

	SD 1.3	GBS 0.9	GBS 1.3
$\dot{\epsilon}$ (s ⁻¹)	3×10^{-2}	3×10^{-4}	3×10^{-4}
Local true strain	1.3	0.9	1.3
Cavity volume fraction	1.35%	1.33%	11.3%
Number of cavities	604	227	316
Average individual cavity volume	109 μm^3	284 μm^3	1737 μm^3

Fig 4.1: The geometry of the tensile coupons (a) for high temperature mechanical test and elongation-to-failure tests in air, and (b) for elongation-to-failure tests in vacuum.

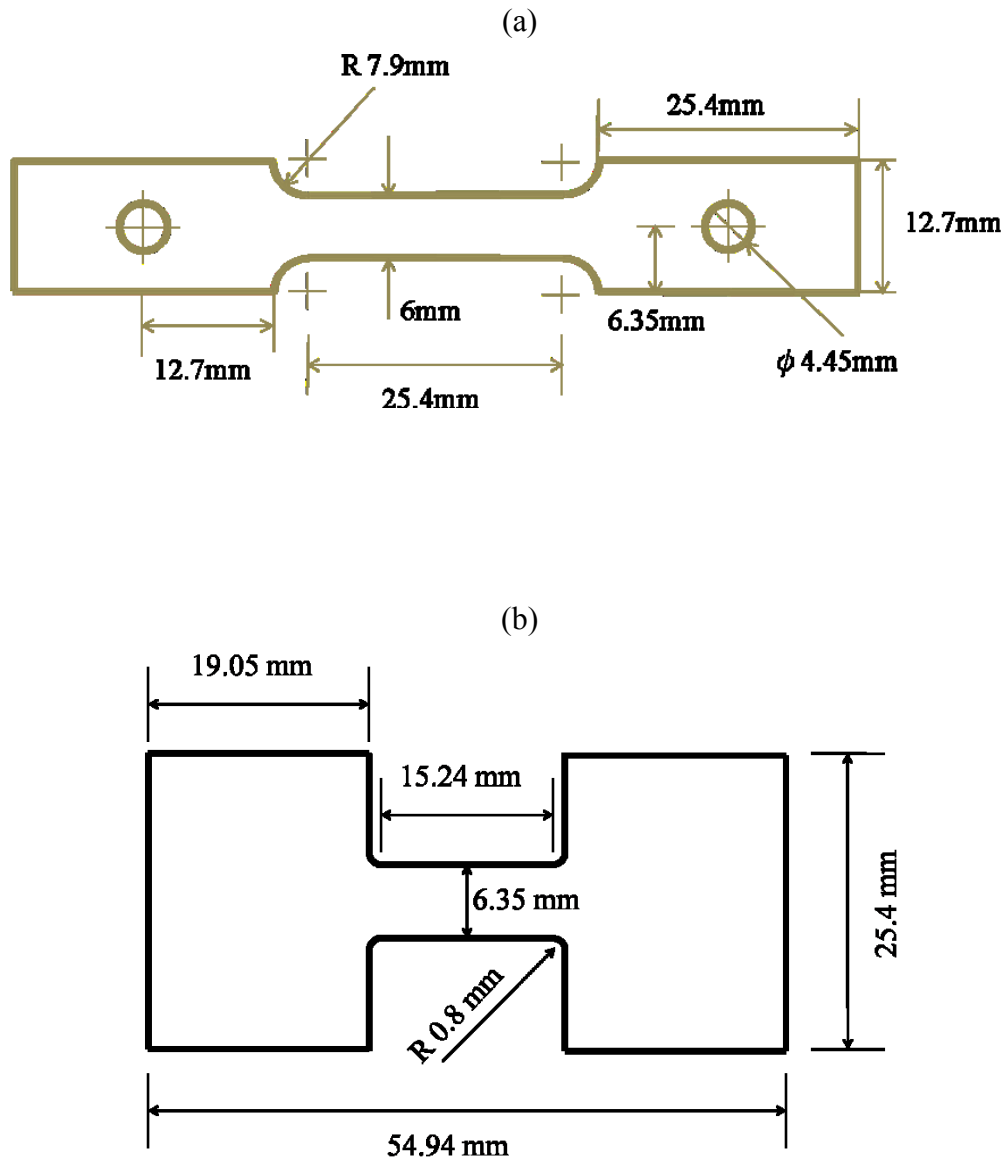


Fig. 4.2: Images are shown of (a) a photograph of the test fixture and (b) a schematic (by Brian South) of the fixture.

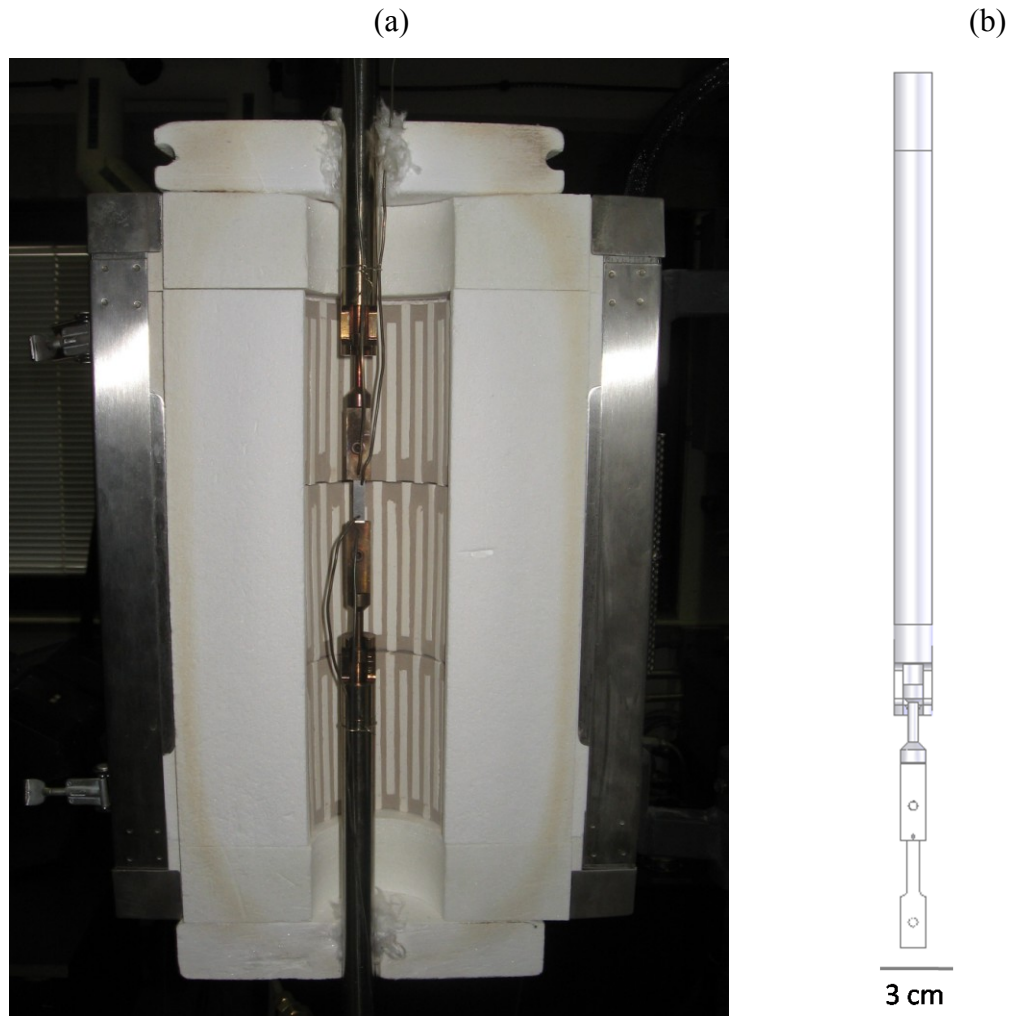
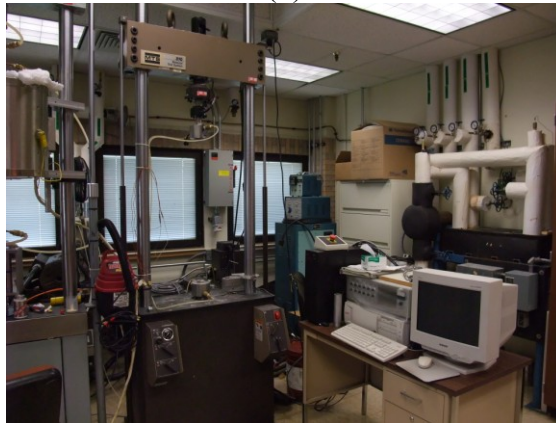


Fig. 4.3: Photographs of testing frames as shown for (a) high temperature mechanical tests, (b) elongation-to-failure tests in air and (c) elongation-to-failure tests in vacuum.

(a)



(b)



(c)

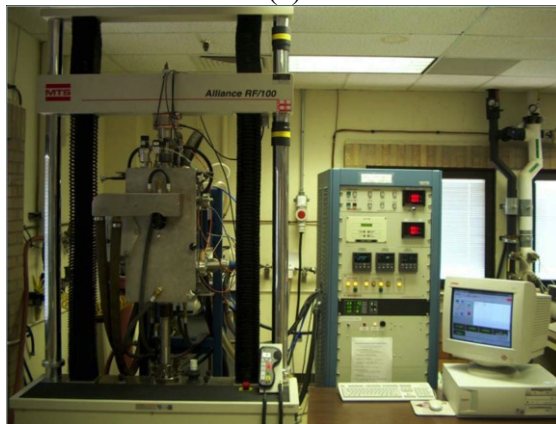


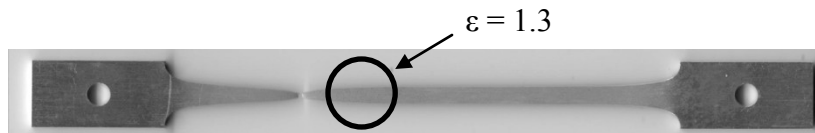
Fig. 4.4: Coupons tested at 450°C under each of the three testing conditions are shown with an untested coupon. Regions representative of those from which metallographic specimens were removed are circled.

Untested Coupon



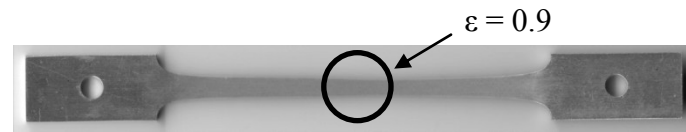
SD 1.3

$$\dot{\epsilon} = 3 \times 10^{-2} \text{ s}^{-1}$$



GBS 0.9

$$\dot{\epsilon} = 3 \times 10^{-4} \text{ s}^{-1}$$



GBS 1.3

$$\dot{\epsilon} = 3 \times 10^{-4} \text{ s}^{-1}$$

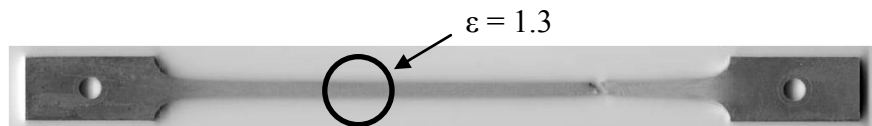


Fig. 4.5: The flow chart of the serial sectioning processes.

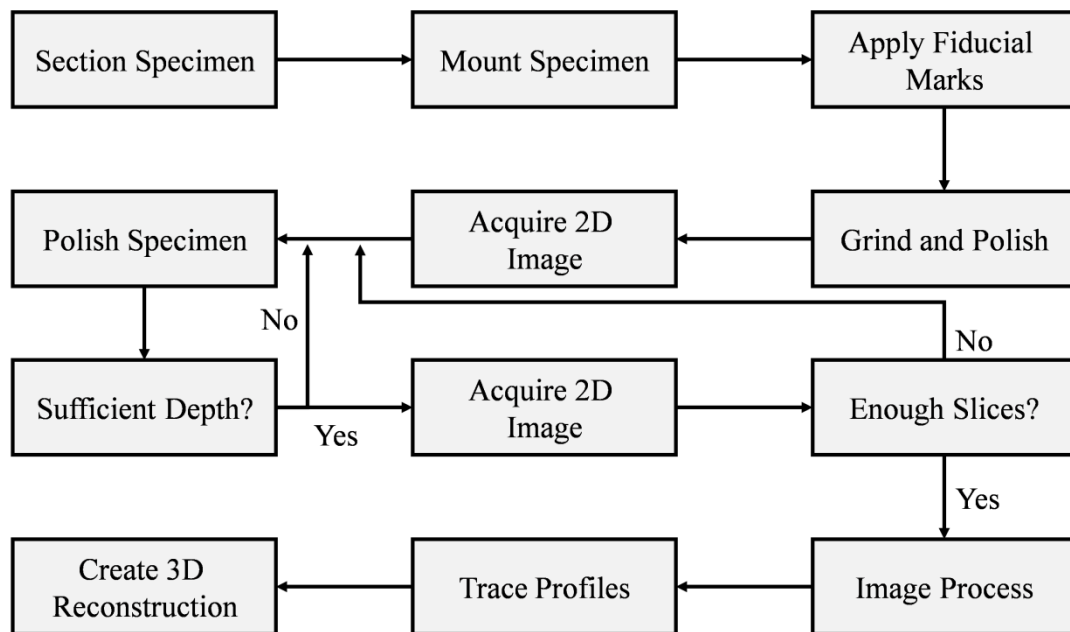


Fig. 4.6: The geometry of the Vickers diamond indenter is shown.

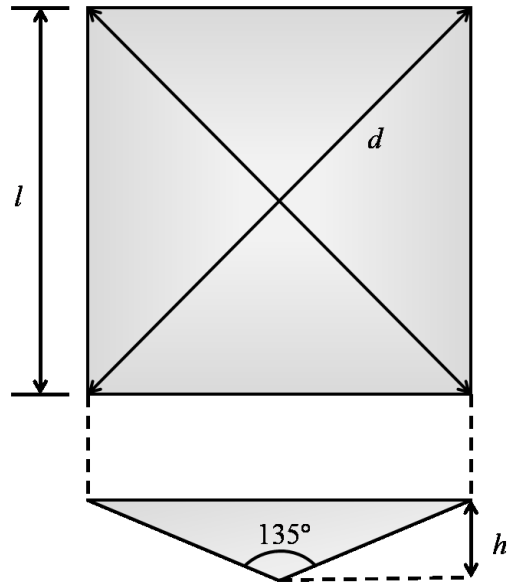


Fig. 4.7: The Allied High Tech MultiPrep™ polishing system is shown.



Fig. 4.8: An example of 2-D microstructure image used for serial section metallography is shown.

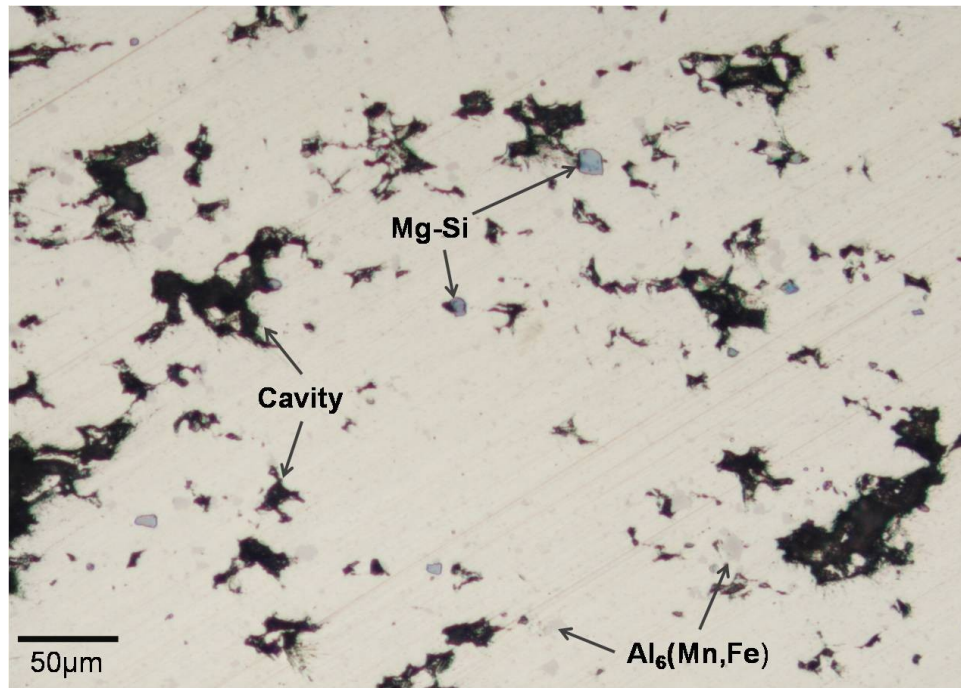


Fig. 4.9: An example of a 3-D microstructure reconstruction is shown.

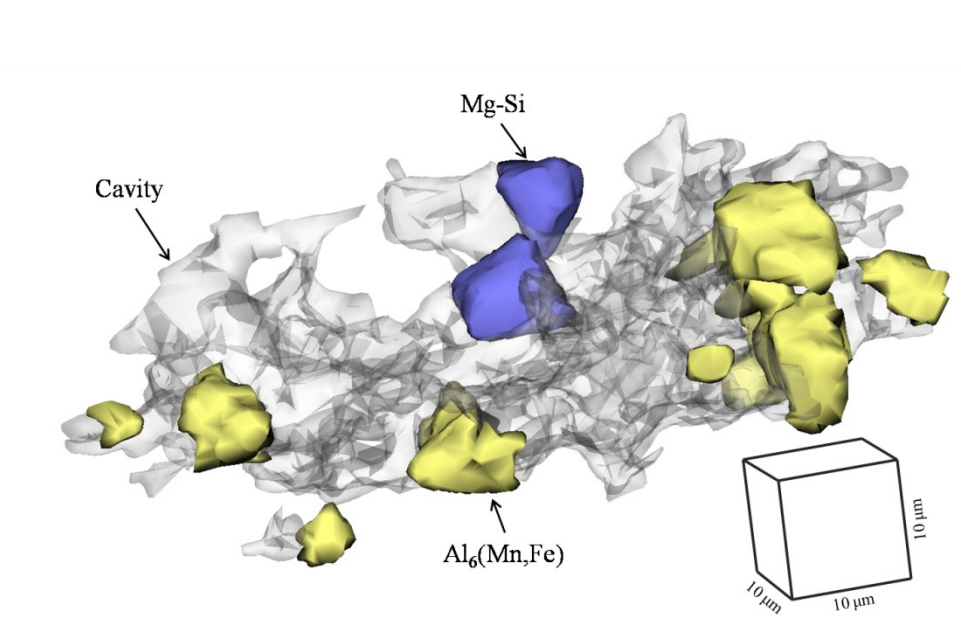
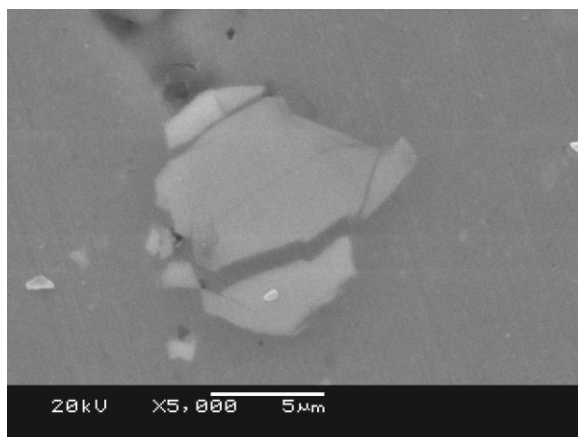
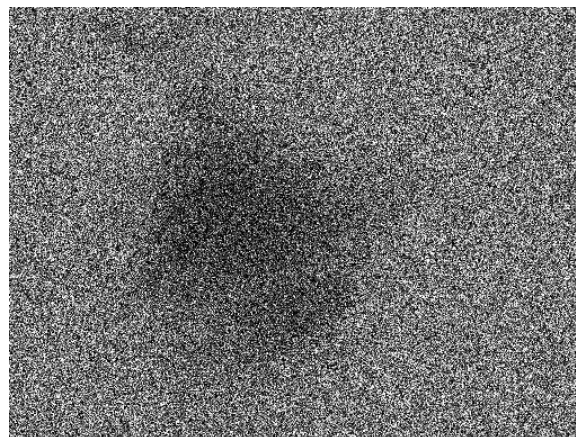


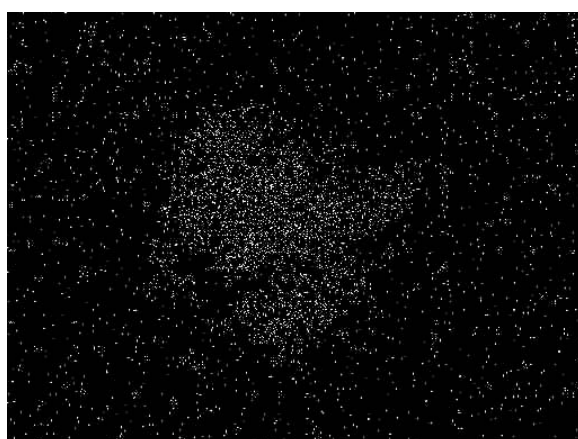
Fig. 4.10: The EDS mappings of $\text{Al}_6(\text{Mn,Fe})$ particles are shown.



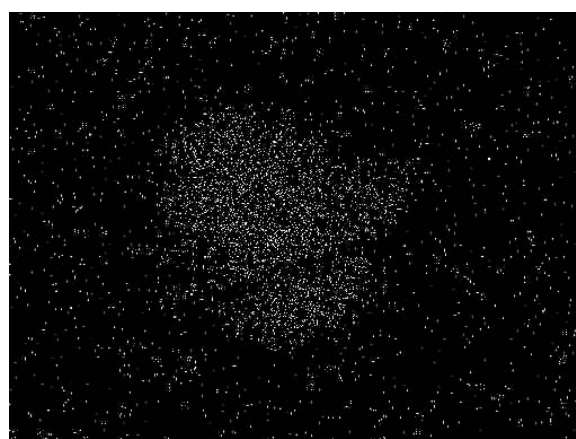
SEM image



Al

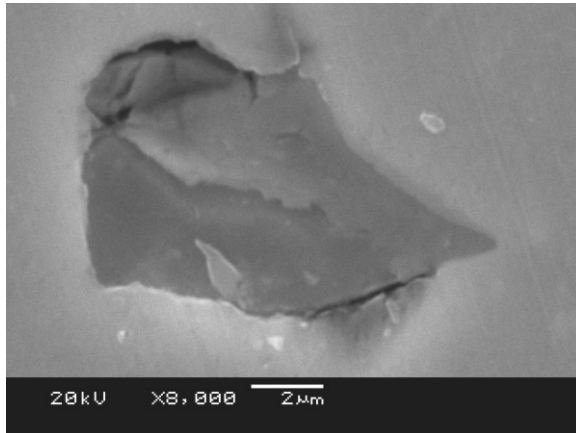


Mn

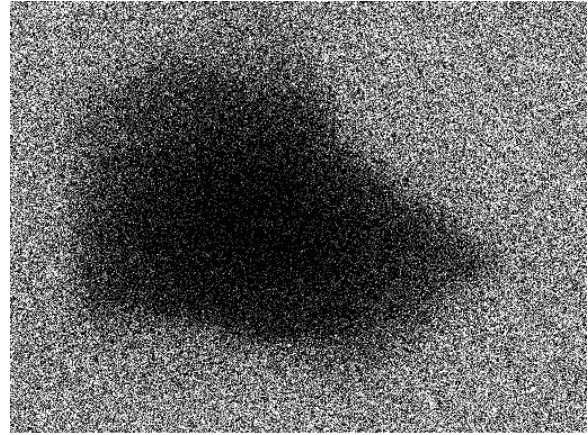


Fe

Fig. 4.11: The EDS mappings of an Mg-Si particle are shown.

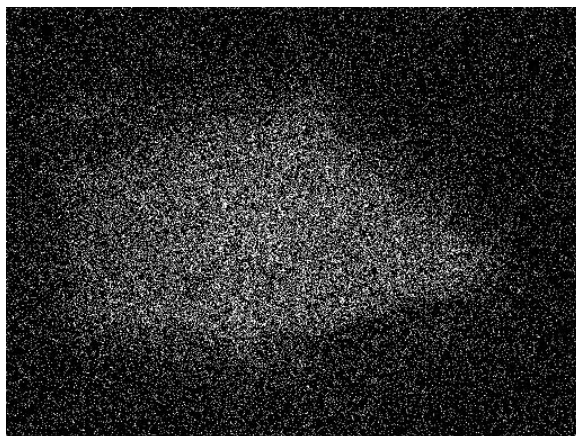


SEM image



Al Kα1

Al



Mg Kα1_2

Mg



Si Kα1

Si

Fig. 4.12: The method of two-point correlation function calculation is shown graphically.

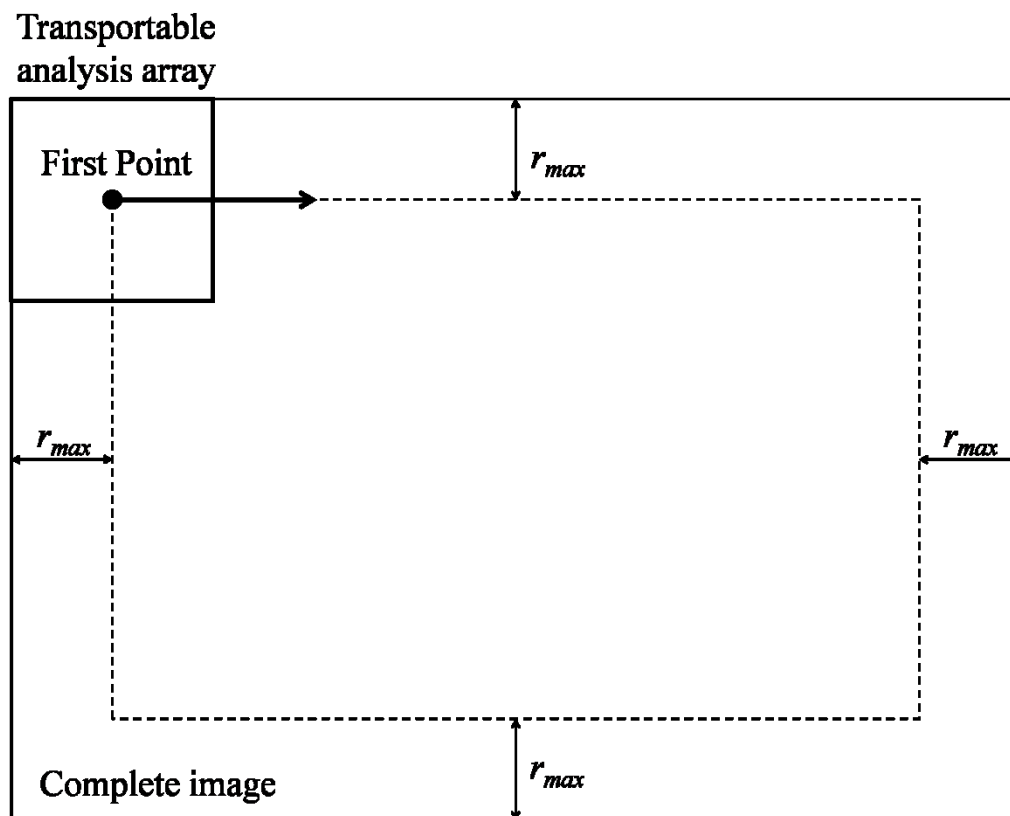


Fig. 4.13: A series of schematic diagrams demonstrates the two-point correlation function methodology of the current study. In (a), an example of a two-phase microstructure image is shown. In (b), the definition of transportable analysis array, base point and measurement frame are shown. Figures (c), (d), (e) and (f) show the calculation method for the two-point correlation function.

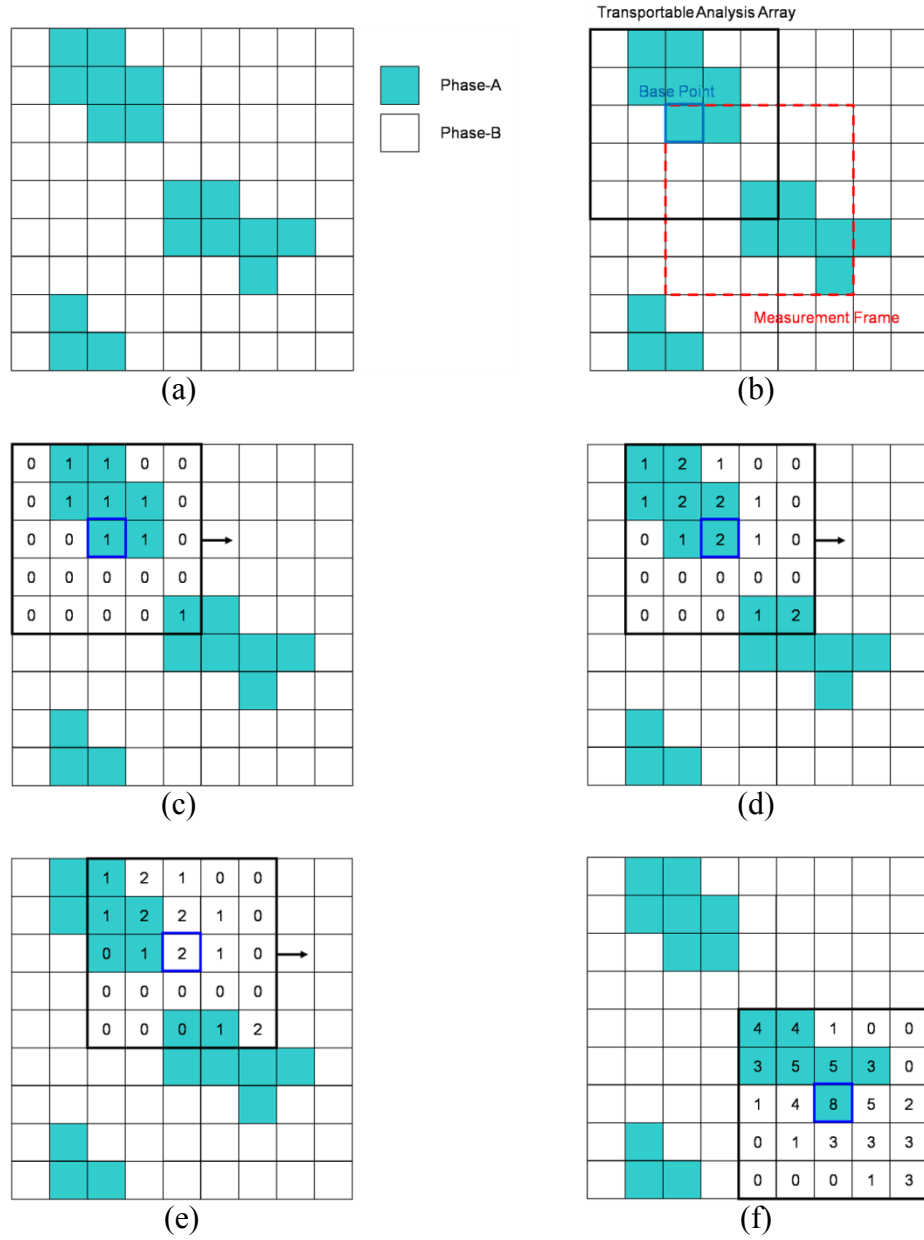


Fig. 4.14: Two calculation methods for correlation probability from a transportable analysis array are shown. The probability in percentage is calculated from a transportable analysis array by dividing by the maximum count of the array, which is 8 in this case. The probability in normalized value is calculated from a transportable analysis array by dividing by the average value of the array, which is 2.36 in this case.

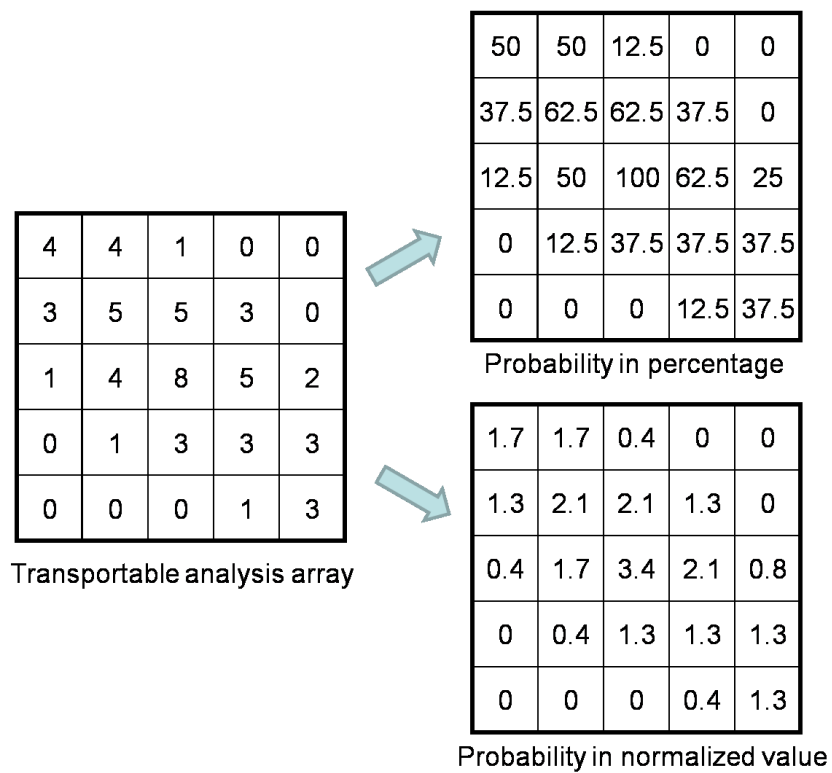
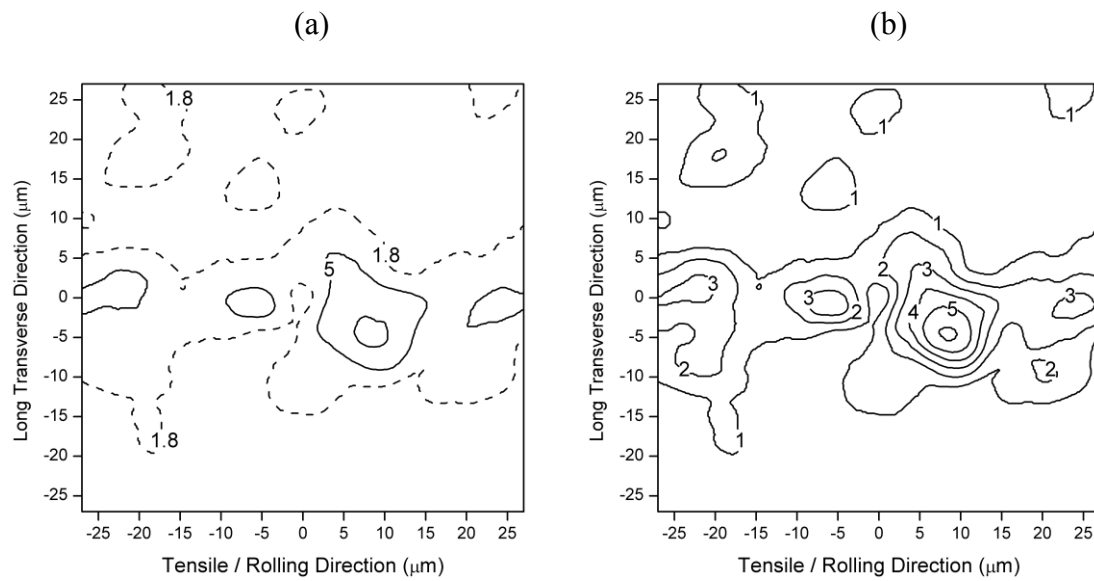


Fig. 4.15: Two contour plots of the same $\text{Al}_6(\text{Mn,Fe})/\text{cavity}$ correlation. The numbers in contour lines represent (a) percentage and (b) normalized correlation.



Chapter 5: Failure Surface Characterization

Several investigations have reported observing filaments on the order of one micrometer in diameter growing on the failure surface of aluminum alloys during superplastic deformation [1, 71-84]. In all cases, the filaments formed only on aluminum alloys tested in air, were aligned along the tensile axis and formed at failure surfaces resulting from deformation under grain-boundary-sliding (GBS) creep, i.e. superplastic deformation. Filaments have been observed with diameters of 0.05 to 3 μm and with lengths up to 100 μm [71-73]. Previous investigations of fine-grained Al-Mg alloys indicated filament growth under GBS creep, but less or no filament growth under dislocation creep, *e.g.* solute-drag (SD) creep [1]. Some investigators have reported suppression of filament formation by an inert atmosphere, such as argon or nitrogen [73-75], but only one photomicrograph of a specimen tested in argon is reported among these studies [75]. Reports of filament composition differ between investigators. Shaw [76] indicated no difference between the chemical composition of fibers and of the bulk material. Cao et al. [77] reported filaments of high-purity aluminum. Other investigators report high concentrations of solute elements, particularly magnesium and oxygen, in the filaments [75, 78-80]. Several mechanisms proposed for formation of these filaments have been summarized by Zelin [73] and Robinson et al. [79]. Those still generally under consideration by researchers include the following: 1. superplastic flow in micro-volumes [81], 2. single-crystalline plasticity [76, 82], 3. viscous flow [77, 80] and 4. oxide growth [73].

In order to better understand the formation of these filaments, the failure surfaces of fine-grained AA5083 after superplastic deformation in air and in vacuum were characterized. Tensile tests were conducted at a temperature of 500°C and a strain rate of

$3 \times 10^{-5} \text{ s}^{-1}$, conditions previously shown to produce deformation by GBS creep [29]. Tests were conducted both in air and in vacuum to explore the potential role of oxygen in filament growth. Chemical compositions of the filaments produced and of the base material were examined by energy dispersive X-ray spectroscopy, EDS, and are compared.

5.1 FAILURE SURFACE MORPHOLOGY

Specimens of fine-grained AA5083 sheet material, see Table 4.1 for composition, were deformed in tension at a temperature 500°C and a true-strain rate of $3 \times 10^{-5} \text{ s}^{-1}$ until fracture. The specimens tested in air and in vacuum were examined in a scanning electron microscope, SEM, after deformation. The specific surface regions examined include: 1. grip surface, 2. deformed surface without fractures or cavities, 3. deformed surface with fractures and exposed cavities and 4. the final fracture surface. SEM photomicrographs taken from examples of each region type are shown in Fig. 5.1 for a specimen tested in air and a specimen tested in vacuum. Figs. 5.1(a) and (b) show surface conditions of undeformed regions in grip areas. Both surfaces were exposed to a temperature of 500°C for approximately 16 hours, one in air and the other in vacuum. Extensive surface oxidation was observed in the specimen exposed to air, while only slight oxidation was observed on the surface of the specimen exposed to vacuum. Figs. 5.1(c) and (d) show regions of deformed surface without fractures following testing in air and in vacuum, respectively. Both show islands of broken oxide film, the remnants of native oxide on the as-received material. Between these islands of broken oxide is a network of material newly exposed during deformation. These newly exposed surfaces exhibit very different surface morphologies between specimens tested in air and in vacuum. For the specimen tested in air, the newly exposed material forms oxide lines, which typically run parallel to the tensile direction. These lines bridge over exposed cavities and may evolve into

filaments, as illustrated in Figs. 5.1(c) and (e). Filaments develop on the fracture surface of the specimen tested in air, as shown in Fig. 5.1(e). For the specimen tested in vacuum, material exposed between islands of broken native oxide appears relatively free of new oxide, as is shown in Figs. 5.1(b), (d), (f) and (h). Neither oxide lines nor filaments are observed on freshly exposed surfaces or across cavities of the specimen tested in vacuum, see Figs. 5.1(b) and 1(d). The fracture surface of the specimen tested in vacuum, Fig. 5.1(f), has no filaments. Because testing in vacuum completely eliminates filament formation, and evidence is available in the literature [74] that an argon atmosphere also eliminates filament formation, it is most likely that oxygen is involved in filament formation.

5.2 EDS ANALYSIS ON FILAMENTS

Filaments analyzed by EDS for the present work typically had diameters of 1 to 2 μm . Such small diameters can be easily penetrated by the analyzing electron beam, introducing unwanted signal from underlying material. To avoid this effect, low-energy electron beams were used to analyze filaments. The Casino v2.42 software package was used to simulate electron beam interaction with the AA5083 material at various beam energies [112]. This software employs a Monte Carlo simulation of electron trajectory in solids designed for low beam interaction in bulk or thin foil specimens. Images of simulated electron interactions in AA5083 bulk material are shown in Fig. 5.2 for electron beam energies at 5 keV, 10 keV and 20 keV. The calculated X-ray generation depth in AA5083 is approximately 3 μm at 20 keV, 1 μm at 10 keV and 0.3 μm at 5 keV. Using low voltage on the SEM will shift the EDS spectrum to low energies, making low-energy peaks larger. Raising beam energy will make high-energy peaks larger. Because the EDS spectrum analysis system was calibrated at an electron beam energy at 20 keV, the most accurate EDS results are obtained at or close to 20 keV.

The effect of various electron energies on EDS analysis of chemical composition was evaluated using a polished AA5083 specimen, high-purity Al_2O_3 powder and a filament from a tested specimen. Table 5.1 shows the characterized chemical compositions using various electron energies. As the electron energy decreases, EDS detection becomes less sensitive to heavy elements, such as Fe and Mn, as shown in Table 5.1 (a). No effect on EDS analysis of polished AA5083 or high-purity Al_2O_3 powder is observed when beam energy is lowered from 20 to 10 keV, see Table 5.1 (a) and (b). Below 10 keV, at 5 and 2.5 keV, beam energy does affect the composition reported from EDS analysis. Thus, an electron beam energy of 10 keV was used to limit the X-ray signal measured to the filament under observation by reducing beam penetration through the filament. The effect of reduced electron beam penetration on EDS analysis results for filament composition is shown in Table 5.1 (c). The decrease in Al and increase in Mg concentrations reported upon reducing beam energy from 20 to 10 keV is a result of less signal from Al matrix underlying the filament, thus revealing a high concentration of Mg in the filament. Chemical compositions of filaments produced during testing in air were characterized using EDS at the reduced electron beam energy of 10 keV.

A typical filament analyzed using EDS is shown in Fig. 5.3. EDS data averaged from eight filaments using a 20 keV electron beam energy and averaged from two filaments using a 10 keV electron beam energy are listed in Table 5. 2. A higher magnesium concentration is measured at an electron beam energy of 10 keV, which is expected to localize X-ray production in the filament, than is measured at 20 keV, for which significant beam penetration beyond the filament results in X-ray production in the base material underlying the filament. This result suggests that filaments are composed of Mg-rich oxide.

EDS analysis was conducted on large areas of specimens after testing. These areas included undeformed grip region, islands of broken native oxide and newly exposed material between those islands, as shown in Fig. 1(d). EDS data taken from undeformed areas in the grip, deformed area in the gage, and newly exposed material between broken native oxides in deformed region, are reported in Table 3. Very little magnesium is observed on the continuous surface of the specimen tested in vacuum, and no magnesium is observed in the newly exposed material of this specimen. The surface is depleted of magnesium by evaporation into the vacuum, and native oxide retains the only measurable quantities of magnesium. According to the X-ray generation depth calculated for AA5083, the depletion depth of magnesium is at least 2 to 3 μm . For the specimen tested in air, however, high concentrations of magnesium and oxygen are observed, suggesting formation of a magnesium-rich oxide. Striations on the newly exposed surface regions, shown in Fig. 5.1(a), are oxide lines, which have compositions similar to those measured for filaments at the fracture surface. This result is consistent with the work of Ritchie et al. [106], who reported that the magnesium-rich oxides MgO and MgAl_2O_4 are preferentially formed on Al-Mg alloys at the testing temperature of the present investigation, 500°C.

5.3 SUMMARY

Various mechanisms of filament formation at fracture surfaces of aluminum alloys during superplastic deformation have been proposed in the literature, including viscous flow [81], single-crystalline plasticity [76, 82], superplastic flow in micro-volumes [77, 80] and oxide growth [73]. Only the oxide growth mechanism is consistent with results of the present investigation. Oxygen was found to play an important role in filament formation during superplastic deformation. No filaments were observed on specimens tested in vacuum. High concentrations of oxygen and magnesium were

observed on newly exposed surfaces and in filaments of specimens tested in air, indicating that magnesium-rich oxide was formed during testing. These results suggest that the formation of filaments during superplastic deformation occurs by growth of magnesium-rich oxides on fine-grained AA5083 material.

Table 5.1: EDS analysis of chemical composition (in atomic %) is shown for: (a) a polished AA5083 material, (b) high-purity Al_2O_3 powder and (c) a filament from a specimen tested in air. Results are shown for several electron beam energies.

(a)

Voltage	O	Mg	Al	Mn	Fe
20 keV	2.2	5.0	92.2	0.40	0.15
10 keV	2.5	5.0	92.1	0.35	-
5 keV	4.9	4.5	90.6	-	-
2.5 keV	14.0	5.0	81.0	-	-

(b)

Voltage	O	Al
20 keV	57.4	42.6
10 keV	58.1	41.9
5 keV	54.3	45.7
2.5 keV	50.8	49.2

(c)

Voltage	O	Mg	Al
20 keV	31.6	12.7	55.8
10 keV	34.7	22.1	43.2

Table 5.2: The average EDS composition of filaments in atomic %.

Voltage	O	Mg	Al
20keV	28	11	Bal.
10keV	30	21	Bal.

Table 5.3: The surface compositions of AA5083 specimens (in atomic %) by EDS at 20 keV

Specimen	Location	O	Mg	Al	Mn	Fe
As-received	All area	10	4.5	Bal.	0.3	0.1
Tested in Air	Grip area	45	29	Bal.	0.3	0.1
Tested in Air	Gage area	27	12	Bal.	0.4	0.1
Tested in Air	Newly exposed	13	7.2	Bal.	0.2	-
Tested in Vacuum	Grip area	13	2.3	Bal.	0.4	0.1
Tested in Vacuum	Gage area	6.3	0.4	Bal.	0.4	0.1
Tested in Vacuum	Newly exposed	1.2	-	Bal.	0.4	0.1

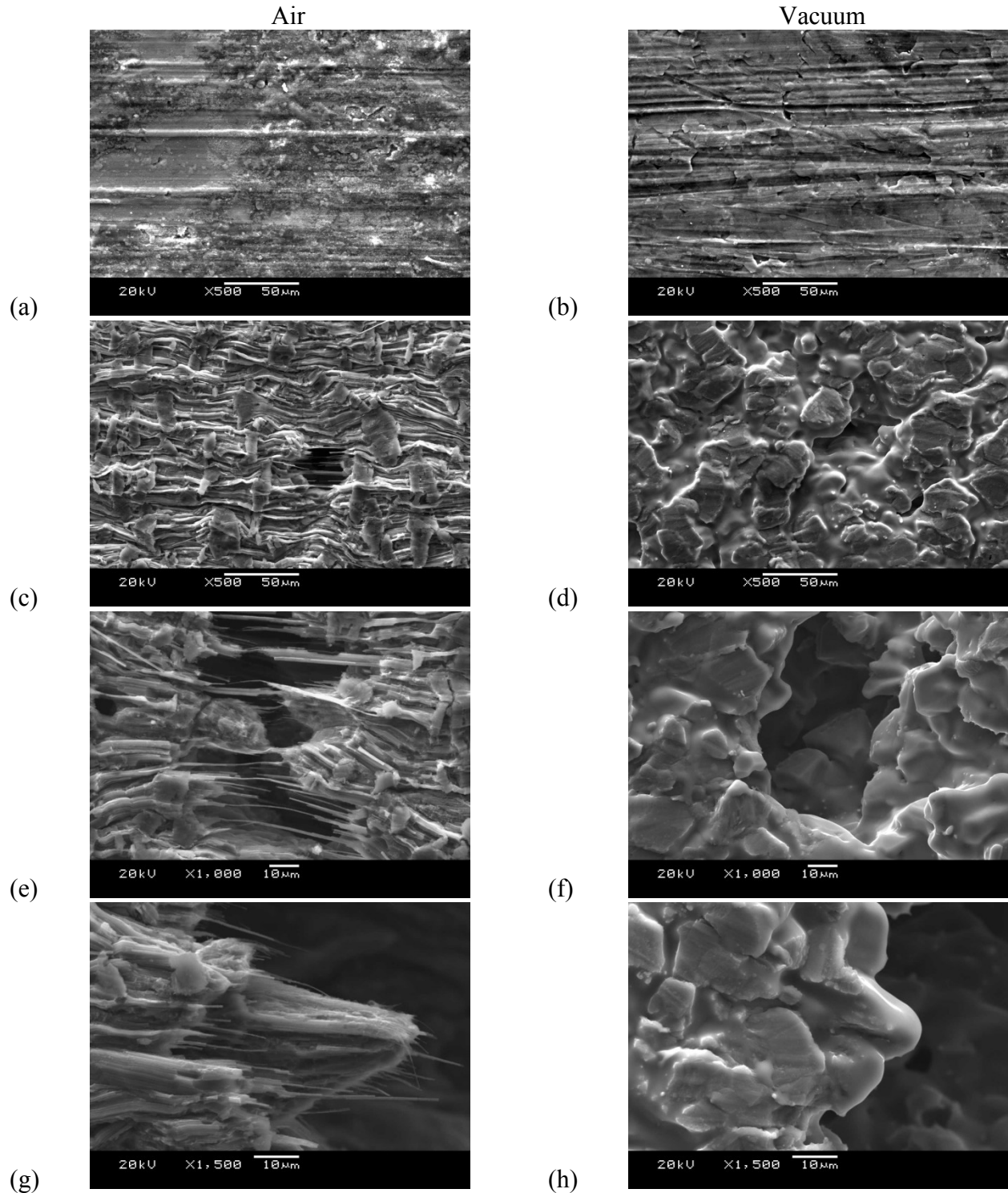


Fig. 5.1: A series of photomicrographs from superplastically deformed AA5083 specimens tested in air (a, c, e, g) and in vacuum (b, d, f, h) is shown. The left column shows images from a specimen tested in air at (a) an undeformed region in the grip, (c) a deformed surface, (e) a cavity opening and (g) the fracture surface. The right column shows a specimen tested in vacuum at (b) an undeformed region in the grip, (d) a deformed surface, (f) a cavity opening and (h) the fracture surface. The tensile axis is horizontal in all images.

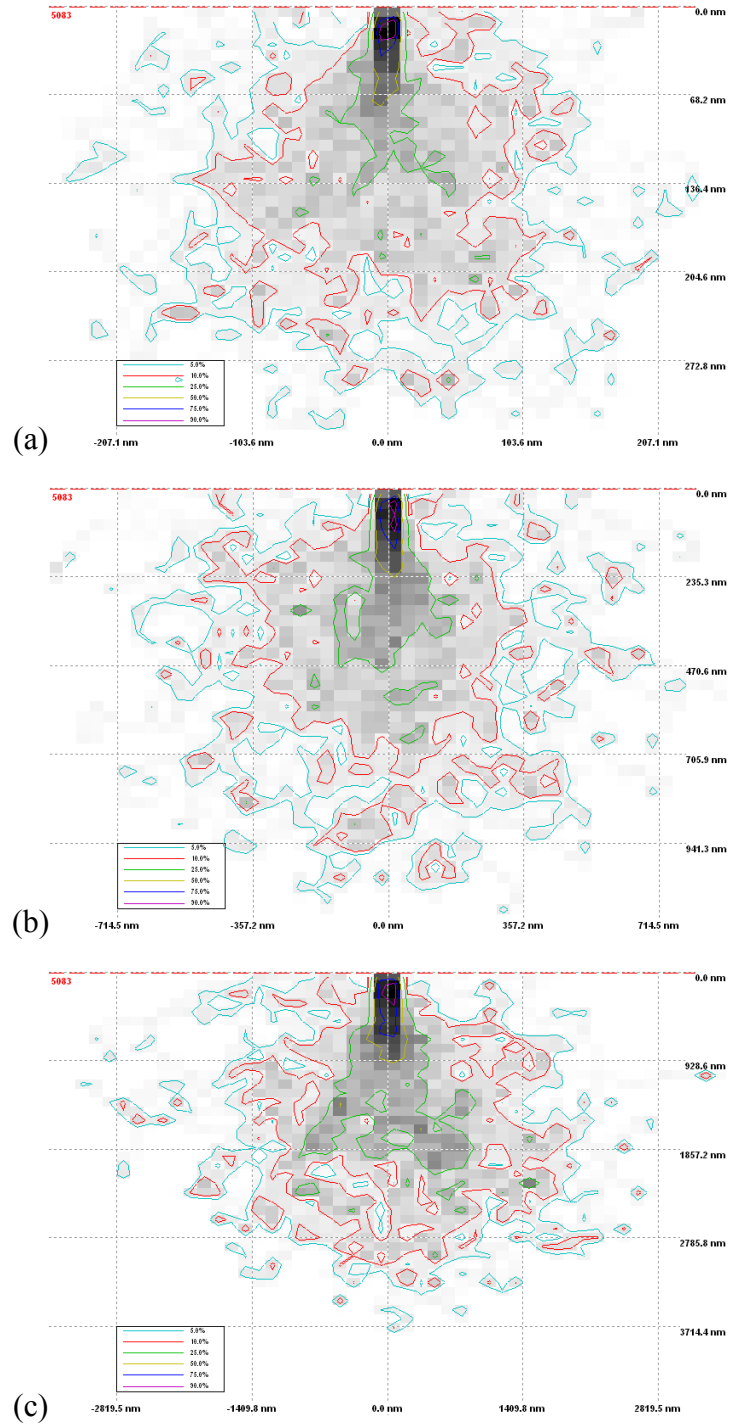
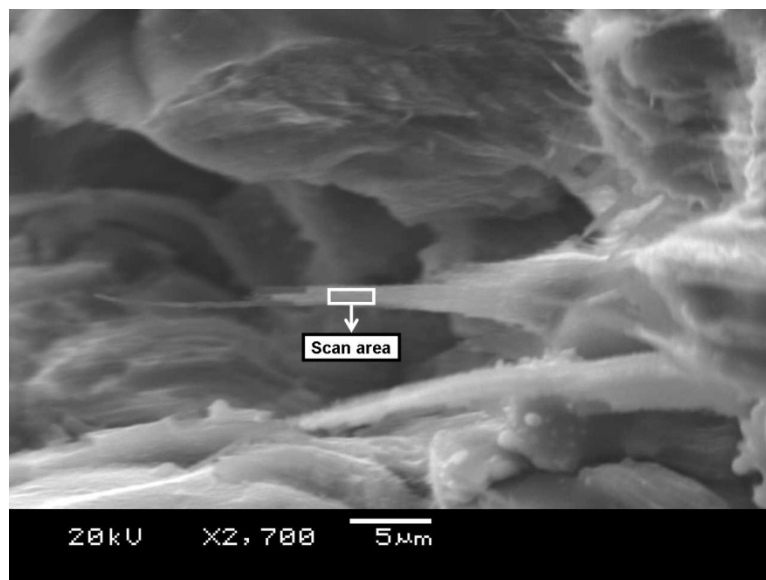


Fig. 5.2: Simulated electron beams interact with AA5083 bulk material are shown. The energies of electron beams simulated are: (a) 5 keV, (b) 10 keV and (c) 20 keV.

Fig. 5.3: A filament analyzed at a reduced beam energy of 10 keV and the EDS scan area are shown.



Chapter 6: Three-Dimensional Characterization

Experiments of this investigation were aimed to produce specimens deformed under GBS creep and under SD creep to various true strains. Fig. 6.1 reproduces the trend lines shown in Fig. 3.4 for logarithm of cavity area fraction as a function of strain and shows data from reference [1], from which these trend lines were drawn. Also shown in Fig. 6.1 are the volume fractions of cavities and the local true strains measured from the three metallographic specimens of the present study. These experimental results agree closely with those expected from the design of experiments, i.e. points A, B and C in Fig. 3.4. Data were collected from each of these three specimens as 2-D serial section images, from which 3-D microstructure reconstructions were produced. Both the 2-D and 3-D data sets were used to quantitatively characterize microstructural features associated with cavitation. Example 2-D images taken from image stacks, used for 3-D reconstructions, are shown in Fig. 6.2. Specimens were mechanically polished with a 1 μm diamond compound for these observations. Although no grain boundary information is provided in these photomicrographs, as-polished specimen images clearly reveal cavities and two types of intermetallic particles. Cavities and both types of particles are important in this investigation, because these microstructural features play fundamentally important roles in cavitation behaviors. All microstructural features shown in Fig. 6.2 are easy to identify using an optical microscope, in which cavities appear black, $\text{Al}_6(\text{Mn,Fe})$ particles appear gray and Mg-Si particles appear with a blue tint.

3-D microstructure reconstructions were produced from 2-D serial sections for 3-D characterization. Characterization of 3-D data sets involves visualization and quantitative analysis to study cavitation behaviors and interactions between cavities and intermetallic particles under different deformation mechanisms and various true strains.

Fig. 4.9 in chapter 4 presented an example of a 3-D microstructure reconstruction of a cavity with adjacent intermetallic particles, produced from the same region of specimen SD 1.3 as the 2-D serial sections shown in Fig. 6.3. This 3-D model clearly demonstrates cavity connectivity and adjacency between the cavity and intermetallic particles, neither of which is fully revealed in the 2-D images of Fig. 6.3. The reconstructed 3-D microstructure data provide useful information not available from 2-D data sets, such as feature volume, surface area, 3-D morphology, connectivity and adjacency. These aspects were evaluated in 3-D microstructure reconstructions from specimens SD 1.3, GBS 0.9 and GBS 1.3. Measurements of cavity volume fraction in each were given in Table 4.2 in chapter 4 and were used to plot the filled data points in Fig. 6.1. Also shown in Table 4.2 were the number of cavities observed and the average individual cavity volume calculated from the 3-D data volumes. Note that these results include features which intersect the data volume surface, i.e. are not completely contained within the 3-D volume observed. These results indicate that the GBS 1.3 specimen contains a cavity volume fraction of 11.3%, and both the GBS 0.9 and SD 1.3 specimens contain a cavity volume fraction of approximately 1.3%.

6.1 VISUALIZATION OF 3-D DATA SETS

Visualizations of 3-D microstructures reconstructed using serial-section data from the three metallographic specimens are shown in Fig. 6.4. Each of the 3-D reconstructions reproduces microstructural features within a volume of $540 \times 360 \times 25 \mu\text{m}$ ($3000 \times 2000 \times 50$ voxels). The rolling direction is horizontal in Fig. 6.4, and the long-transverse direction is vertical. Three different microstructural features are shaded in Fig. 6.4: 1. cavities, 2. $\text{Al}_6(\text{Mn,Fe})$ intermetallic particles and 3. Mg-Si intermetallic particles. Each feature type is distinguished in Fig. 6.4 by a color shown in the color key at the bottom of that figure. The regions not colored are Al matrix material. The

resolution of these 3-D reconstructions is limited by the pixel size of acquired 2-D images ($0.18\ \mu\text{m}/\text{pixel}$) and the spacing of serial sections, which is on average $0.5\ \mu\text{m}$ between each serial section. These 3-D microstructure reconstructions provide sufficient detail to qualitatively and quantitatively characterize most of the microstructural features which control cavitation. The most important microstructure feature not included in these data is the grain boundary, which is a challenge to experimental technique left for future studies.

6.2 QUALITATIVE ANALYSIS OF MICROSTRUCTURE IN 3-D DATA SETS

The left column of images in Fig. 6.4 displays all the microstructural features contained in the 3-D reconstructions. The right column in Fig. 6.4 displays detailed images of regions from 3-D data sets of the left column, shown at a higher magnification. Cavity sizes, morphologies and distributions are clearly different among the three specimens. Qualitative observation of Figs. 6.4(a) and (b) reveal cavities elongated and aligned along the tensile (rolling) direction in the SD 1.3 specimen, which is consistent with the two-point correlation functions to be discussed and shown in chapter 7 in Figs. 7.5 and 7.8. Observation of Figs. 6.4(c) and (d) reveal cavities which are more equiaxed and somewhat aligned along the tensile (rolling) direction in the GBS 0.9 specimen, which is consistent with the two-point correlation functions to be discussed in chapter 7 and shown in Figs. 7.5 and 7.8. Observation of Figs. 6.4(e) and (f) reveal cavities which tend to grow in multiple directions and coalesce with other cavities perpendicular to tensile axis. Highly convoluted cavity shapes observed in the GBS 1.3 specimen are not fully revealed by two-point correlation functions to be discussed in chapter 7 and shown in Figs. 7.5 and 7.8. The alignment of cavities observed in the GBS 0.9 specimen, Fig. 6.4(c), is not apparent in the GBS 1.3 specimen, Fig. 6.4(e). This is consistent with two-point correction functions to be discussed in chapter 7 and presented in Figs. 7.5 and 7.8. However, several small cavities are still clearly observed in Fig. 6.4(e), supporting

the concept of continuous nucleation of new cavities during deformation [52]. This is also in agreement with the observed increase in cavity numbers between the strains of 0.9 and 1.3. These observations indicate that cavity evolution is significantly different between the three specimens. Detailed qualitative examination of 3-D visualizations shown in Fig. 6.4 suggests a large fraction of intermetallic particles adjacent to cavities in all specimens.

Fig. 6.5 displays only intermetallic particles contained in the 3-D reconstructions. The 3-D spatial distributions and particle size distributions of both $\text{Al}_6(\text{Mn,Fe})$ and Mg-Si type intermetallic particles appear very similar between the three specimens. This suggests no differences in intermetallic particle distributions between specimens, which could significantly alter the cavitation behavior. Some clustering of $\text{Al}_6(\text{Mn,Fe})$ intermetallic particles is observed in all specimens, while no obvious clustering occurs for Mg-Si intermetallic particles. Such observations suggest that $\text{Al}_6(\text{Mn,Fe})$ particles may break and redistribute during thermomechanical processes. Detailed examination of the $\text{Al}_6(\text{Mn,Fe})$ particle clustering reveals a high probability cavities exist in these areas. This implies that cavities tend to nucleate in regions with a high density of intermetallic particles.

6.3 QUANTITATIVE ANALYSIS OF CAVITIES IN 3-D DATA SETS

Quantitative analysis of 3-D data sets provides useful microstructure information, such as the number density of microstructural features, cavity – particle adjacency fraction, feature surface area and feature volume, which are not available from 2-D microstructure data. The number density of cavities is an important parameter because it provides information on the cavitation mechanism. The cavitation processes usually occurs in three steps: 1. nucleation, during which the number of cavities is increasing, 2. growth of cavities, during which the number is stable and 3. coalescence, during which

the number decreases. These steps can occur simultaneously during straining. Some microstructure differences between specimens were quantified in Table 4.2. Both the SD 1.3 and GBS 0.9 specimens contain a similar volume fraction of cavities, approximately 1.3%, but contain very different numbers of cavities for the same observed volume, 604 cavities versus 227 cavities, respectively. This results in very different average individual cavity sizes between the SD 1.3 and GBS 0.9 specimens, as was shown in Table 4.2. The GBS 1.3 specimen contains almost ten times the volume fraction of cavities that the specimen GBS 0.9 contains, but it contains only 40% more cavities by number. This results in an average individual cavity size in the GBS 1.3 specimen which is at least six times that of the GBS 0.9 specimen, as is shown in Table 4.2. The small increase in cavity numbers between specimen GBS 0.9 and GBS 1.3 suggests that much of the cavity volume increase under GBS deformation between strains of 0.9 and 1.3 is a result of individual cavity growth and coalescence of cavities. This is consistent with qualitative observations from Figs. 6.4(e) and (f), which shows large, continuous cavities that frequently interconnect.

Surface area measurements from 3-D reconstructions were used to evaluate the shape factors of microstructural features using the following relationship,

$$\text{Shape Factor} = \frac{\text{Measured Surface Area}}{\text{Equivalent Spherical Surface Area}} \quad (6.1)$$

where the equivalent spherical surface area is the minimum surface area of a feature with same volume. For example, the shape factor of a sphere is equal to 1, and the shape factor of a cube is approximately 1.24. Thus, the shape factor is one measure of the surface morphology of cavities. A large shape factor indicates a complex shape, while a small shape factor indicates a nearly spherical shape. Fig. 6.6 shows plots of cavity shape factor against cavity equivalent spherical diameter for all three specimens. Only data from cavities completely including in the 3-D data volumes, i.e. which do not intersect the

surface of the data volume, are included in Fig. 6.6. Cavities adjacent to particles are also distinguished in Fig. 6.6. The filled data points in Fig. 6.6 are cavities with one or more adjacent particles, and the open points are cavities without an adjacent particle. Note that only cavities larger than 1.75 μm equivalent spherical diameter are considered for values shown Fig. 6.6.

Small cavities typically have small shape factors as shown in Fig. 6.6(a), suggesting that newly nucleated cavities are approximately spherical in shape. As revealed in Fig. 6.6(a), an increase in cavity size is accompanied by an increase in shape factor for the SD 1.3 specimen. As cavitation developed with straining, cavities grew and formed more complex morphologies. The elongated cavities in the SD 1.3 specimen along the tensile (rolling) direction, which are observed from both 3-D reconstruction (Fig. 6.4) and 2-D two-point correlation analysis (Figs. 7.5 and 7.8) strongly affect the shape factors measured. Significant nucleation occurred in the SD 1.3 specimen because a large fraction of cavities have small equivalent spherical diameter. As shown in Fig. 6.6(b), no significant relationship between cavity equivalent spherical diameter and shape factor is observed for the GBS 0.9 specimen. Two important observations are apparent from Fig. 6.6(b). First, small cavities, said less than 3 μm , are only a small portion of whole population. Second, cavity sizes are evenly distributed within observed data volume. These observations suggest the development of cavitation dominated by cavity growth. Data in Fig. 6.6(c), suggest that shape factor increases with increasing cavity, which is similar to the trend of data in Fig. 6.6(a). Cavities grow under GBS creep to form complex morphologies which are highly convoluted, as are those shown in Figs. 6.4(e) and 6.4(f). Data in Fig. 6.6(c) reveal a large number of small cavities, indicating continuous nucleation of new cavities during deformation. Note that most large cavities in the GBS 1.3 specimen are not shown in Fig. 6.6(c) because these cavities intersect the

data volume and are not included in these data. These observations from Fig. 6.6(c) imply that cavity nucleation, growth and coalescence simultaneously occurred in the GBS 1.3 specimen.

From observation of Fig. 6.6, a large fraction of cavities are adjacent to particles and particles tend to be adjacent to large cavities in all three specimens. This suggests that particles play important roles in cavitation. These intermetallic particles may provide potential sites for cavity nucleation and may enhance the cavity growth during deformation.

6.4 QUANTITATIVE ANALYSIS OF PARTICLES IN 3-D DATA SETS

The data in Table 6.1 imply that all three specimens contain similar number densities of each intermetallic particle type. The ratio of $\text{Al}_6(\text{Mn,Fe})$ to Mg-Si particles is approximately 10:1 for all specimens. Note that particles which intersect the data volume surface and those with particle sizes of less than $1.75\ \mu\text{m}$ equivalent spherical diameter are not included in this analysis. Particle shape factor is presented as a function of particle size for $\text{Al}_6(\text{Mn,Fe})$ and Mg-Si particles in Figs. 6.7 and 6.8, respectively. As in Fig. 6.6, the filled data points in Figs. 6.7 and 6.8 are particles with one or more adjacent cavities, and the open points are particles without an adjacent cavity. Particle size and shape distributions for $\text{Al}_6(\text{Mn,Fe})$, Fig. 6.7, and Mg-Si, Fig. 6.8, particles are similar between the three specimens for a given particle type. Shape factors for both types of intermetallic particles are generally less than 2, which means that most particles are approximately spherical in shape. These data show no correlation between shape factor and particle – cavity adjacency in the three specimens.

$\text{Al}_6(\text{Mn,Fe})$ and Mg-Si particle size distributions measured from the observed 3-D data sets are shown in Fig. 6.9. The particle size distributions for $\text{Al}_6(\text{Mn,Fe})$ particles, Fig. 6.9(a), and Mg-Si particles, Fig. 6.9(b), in the three metallographic specimens are

almost identical for a given particle type. The consistencies of particle densities and distributions between specimens imply that cavitation does not significantly alter particle sizes, at least to within the strain and cavity volume fractions represented in specimen GBS 1.3.

6.5 RELATIONSHIPS BETWEEN PARTICLES AND CAVITIES

Detailed qualitative examination of 3-D visualizations shown in Fig. 6.4 suggests a large fraction of intermetallic particles adjacent to cavities. This observation was further investigated in a quantitative manner by measuring the type, number and size of intermetallic particles adjacent to cavities and of intermetallic particles not adjacent to cavities. As shown in Table 6.1, the cavity adjacency fraction, the fraction of particles adjacent to cavities, for Mg-Si particles is much larger than that of $\text{Al}_6(\text{Mn,Fe})$ particles. From 67 to 84% of Mg-Si particles are adjacent to cavities, but only 11 to 22% of $\text{Al}_6(\text{Mn,Fe})$ particles are adjacent to cavities. Note that only particles larger than 1.75 μm equivalent spherical diameter are considered for values shown in Table 6.1. Both types of intermetallic particles are more likely to be adjacent to cavities as particle diameter increases. The average equivalent spherical diameter of $\text{Al}_6(\text{Mn,Fe})$ intermetallic particles adjacent to cavities is approximately 70% larger than that of $\text{Al}_6(\text{Mn,Fe})$ particles not adjacent to cavities. For Mg-Si intermetallic particles adjacent to cavities, the average equivalent spherical diameter is approximately 40% larger than that of Mg-Si particles not adjacent to cavities. These results suggest that cavities occur more frequently adjacent to large intermetallic particles during straining in all specimens and those cavities occur preferentially at Mg-Si particles.

Fig. 6.10 shows the fraction of particles adjacent to cavities as a function of equivalent spherical diameter for (a) $\text{Al}_6(\text{Mn,Fe})$ and (b) Mg-Si particles. Only particles with equivalent spherical diameters of 2 μm and greater are considered for the

distributions shown in Fig. 6.10, and the bin size of distributions presented is 1 μm . For both particle types, an increase in particle size increases the probability of cavity adjacency. This trend is significantly more pronounced for $\text{Al}_6(\text{Mn,Fe})$ particles. While nearly 100% of $\text{Al}_6(\text{Mn,Fe})$ particles with an equivalent spherical diameter of 10 μm and greater reside adjacent to a cavity, less than 10% at the smallest measured diameters (2 to 3 μm) reside adjacent to a cavity. While 100% of Mg-Si particles with a diameter of 7 μm or greater reside adjacent to a cavity, more than 60% at the smallest measured diameters (2 to 3 μm) also reside adjacent to a cavity. These findings strongly suggest that Mg-Si particles are more prone to nucleate cavities than are $\text{Al}_6(\text{Mn,Fe})$ particles, particularly at small particle sizes. However, because there are approximately ten times as many $\text{Al}_6(\text{Mn,Fe})$ particles as Mg-Si particles, it is clear that both particle types play important roles in the cavitation process.

Table 6.1: The number of particles, percentage of particles adjacent to cavities, average size of adjacent particles and average size of non-adjacent particles are given as a function of particle type in the 3-D data sets. Each 3-D data set has a volume of $540 \times 360 \times 25 \mu\text{m}$.

	SD 1.3		GBS 0.9		GBS 1.3	
	Al ₆ (Mn,Fe)	Mg-Si	Al ₆ (Mn,Fe)	Mg-Si	Al ₆ (Mn,Fe)	Mg-Si
Number of particles	1053	109	1171	108	1157	117
Cavity adjacency (%)	16.4	83.5	11.3	66.7	21.7	70.1
Average size of particle adjacent to cavity (μm)	5.5	4.0	5.3	4.2	4.7	3.8
Average size of particle not adjacent to cavity (μm)	2.9	2.7	3.0	3.2	2.8	2.8

Fig. 6.1: Data for cavity content as a function of strain are shown in a plot similar to that of Fig. 3.4, which was used in the design of experiments. Open symbols are data for cavity area fraction from Ref. [1]. Filled symbols are cavity volume fractions measured from the three metallographic specimens examined in this investigation.

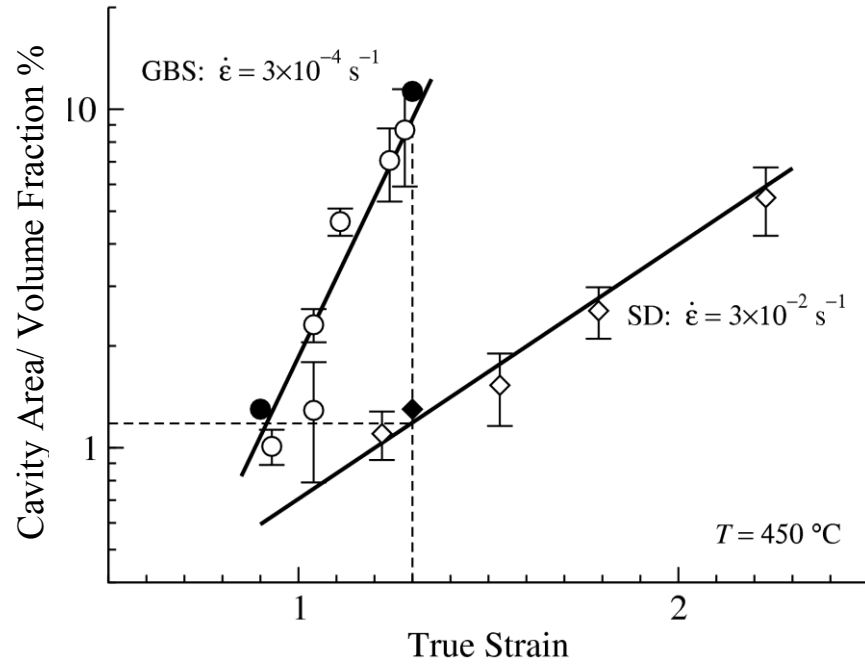
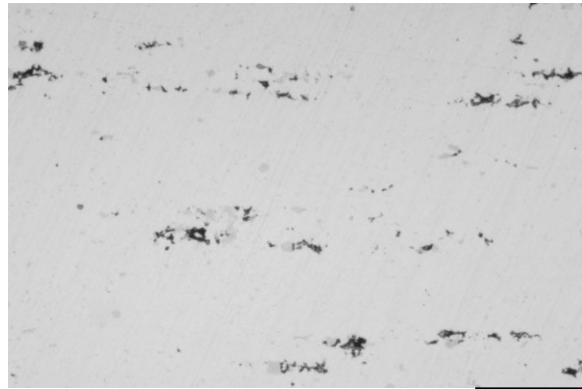
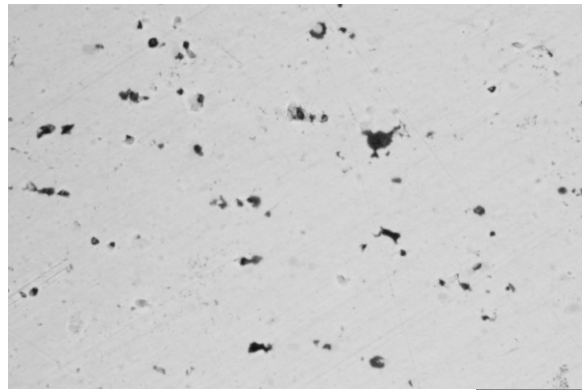


Fig. 6.2: Example 2-D photomicrographs from (a) SD 1.3, (b) GBS 0.9 and (c) GBS 1.3 specimens used for 3-D microstructure reconstructions are shown.



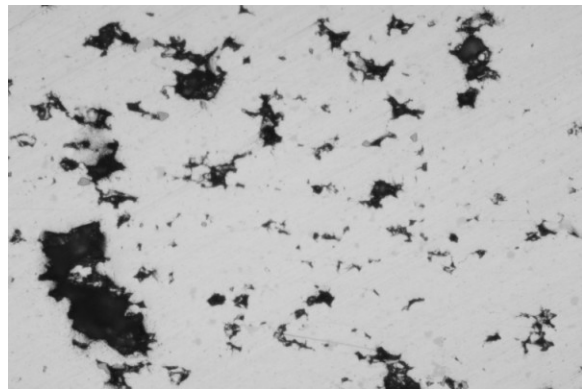
(a) SD 1.3

100 μm



(b) GBS 0.9

100 μm



(c) GBS 1.3

100 μm

Fig. 6.3: Three optical photomicrographs taken at three different polishing depths in specimen SD 1.3 are shown. The plane of (b) is 2.5 μm below that of (a), and the plane of (c) is 5 μm below that of (a). Four microstructural features can be distinguished: matrix, cavity, $\text{Al}_6(\text{Mn,Fe})$ intermetallic and Mg-Si intermetallic.

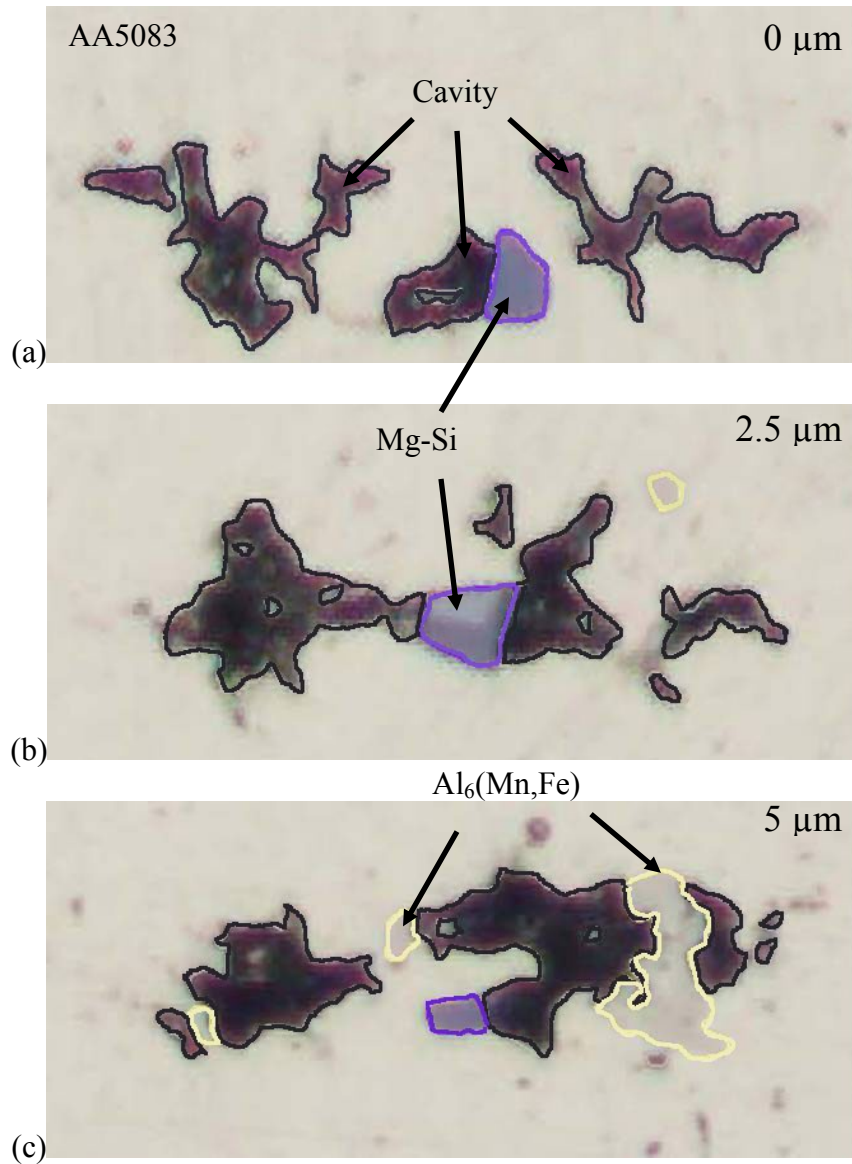


Fig. 6.4: 3-D microstructure reconstructions from serial sections of (top) SD 1.3, (middle) GBS 0.9 and (bottom) GBS 1.3 specimen data sets are shown. In the left column, all distinguishable objects are displayed. In the right column, a select region of each 3-D data set is shown at higher magnification.

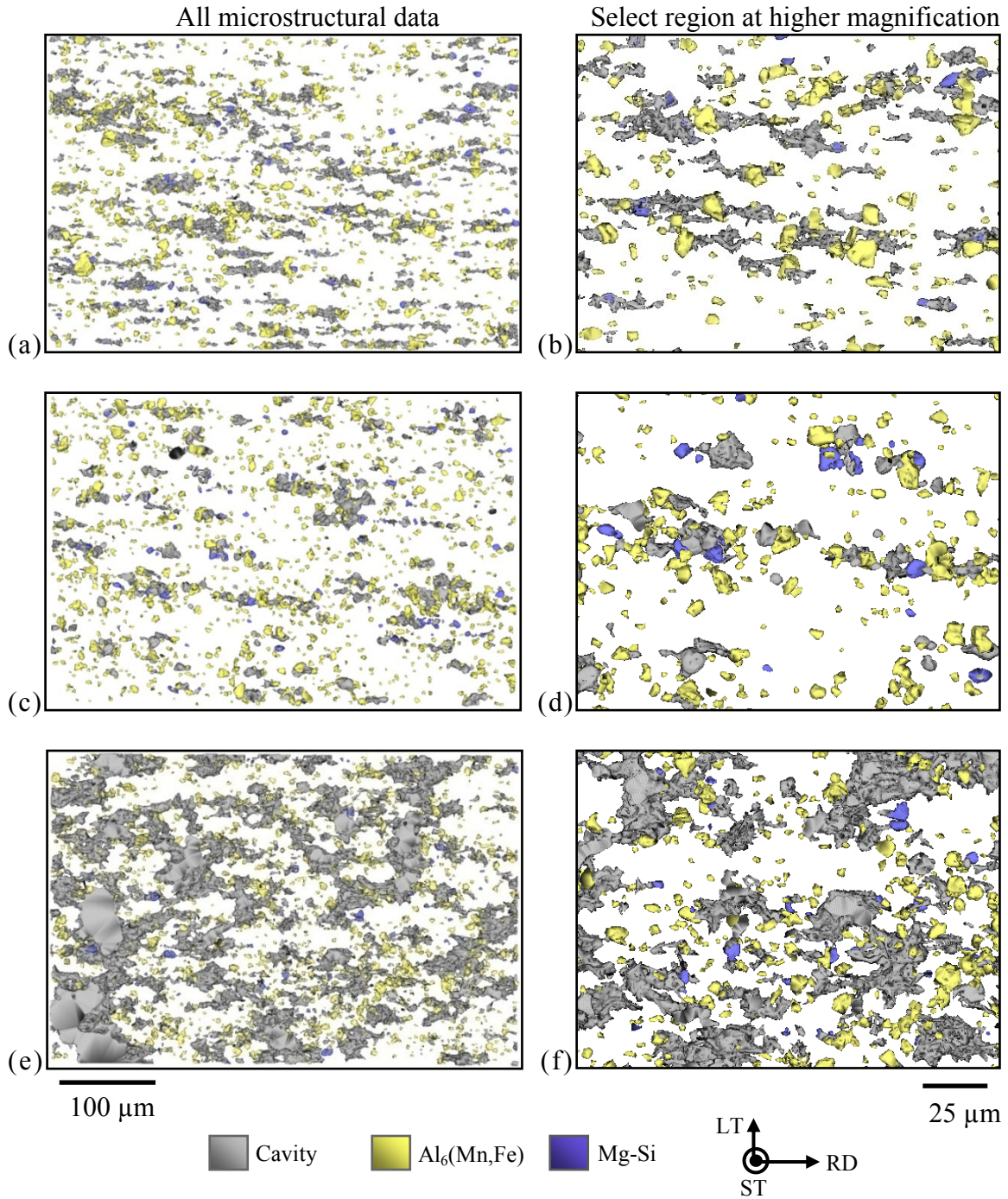


Fig. 6.5: 3-D microstructure reconstructions for intermetallic particles from serial sections of (a) SD 1.3, (b) GBS 0.9 and (c) GBS 1.3 specimen data sets are shown.

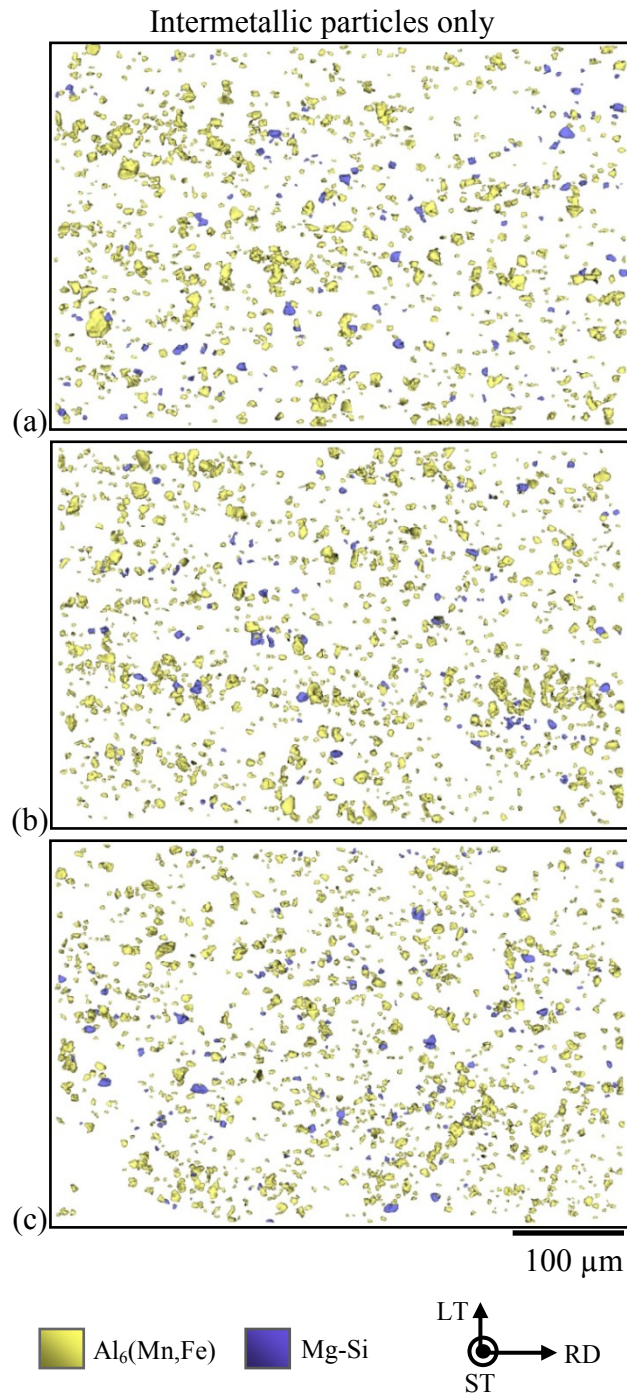


Fig. 6.6: Cavity shape factor against cavity equivalent spherical diameter for (a) SD1.3, (b) GBS 0.9 and (c) GBS 1.3 specimens are shown.

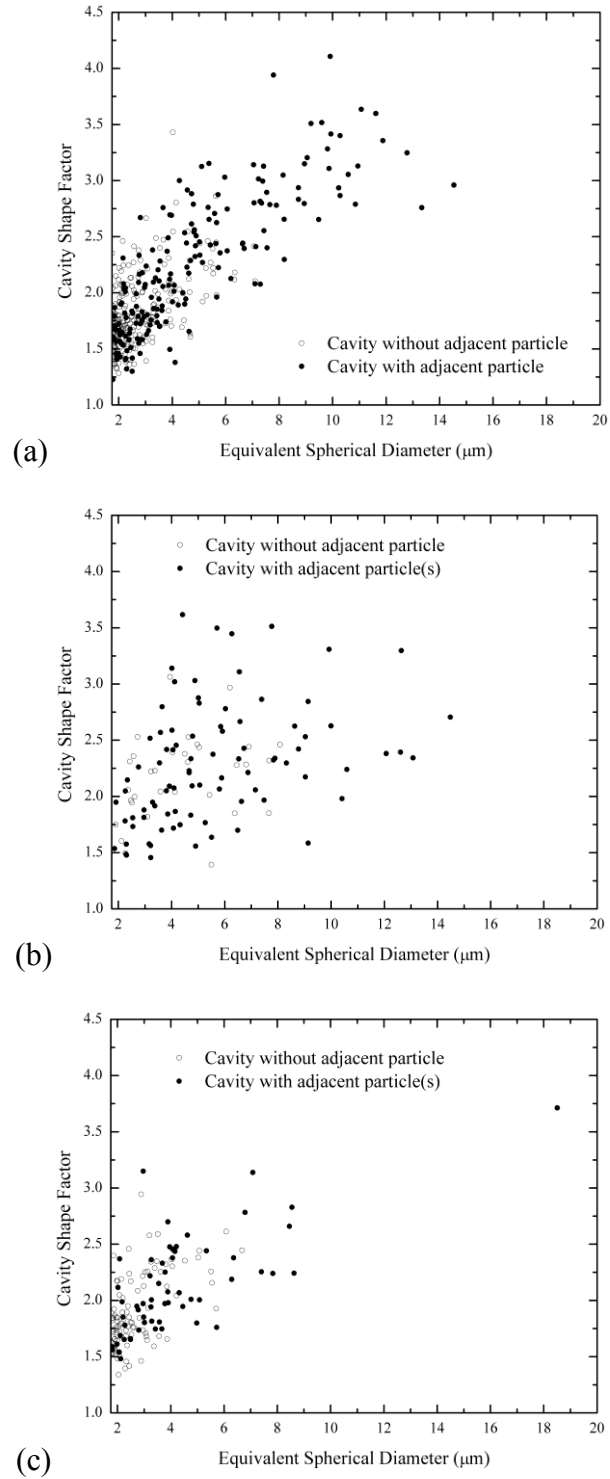


Fig 6.7: $\text{Al}_6(\text{Mn,Fe})$ particle shape factor against particle equivalent spherical diameter for (a) SD1.3, (b) GBS 0.9 and (c) GBS 1.3 specimens are shown.

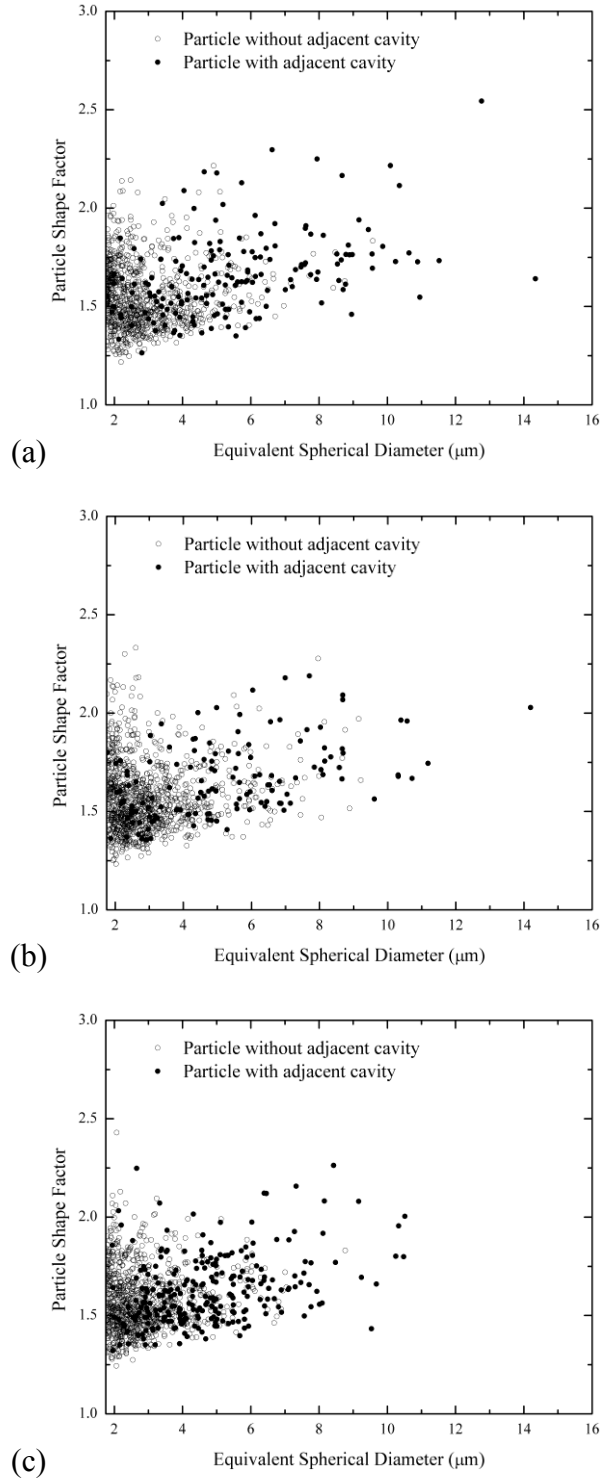


Fig 6.8: Mg-Si particle shape factor against particle equivalent spherical diameter for (a) SD1.3, (b) GBS 0.9 and (c) GBS 1.3 specimens are shown.

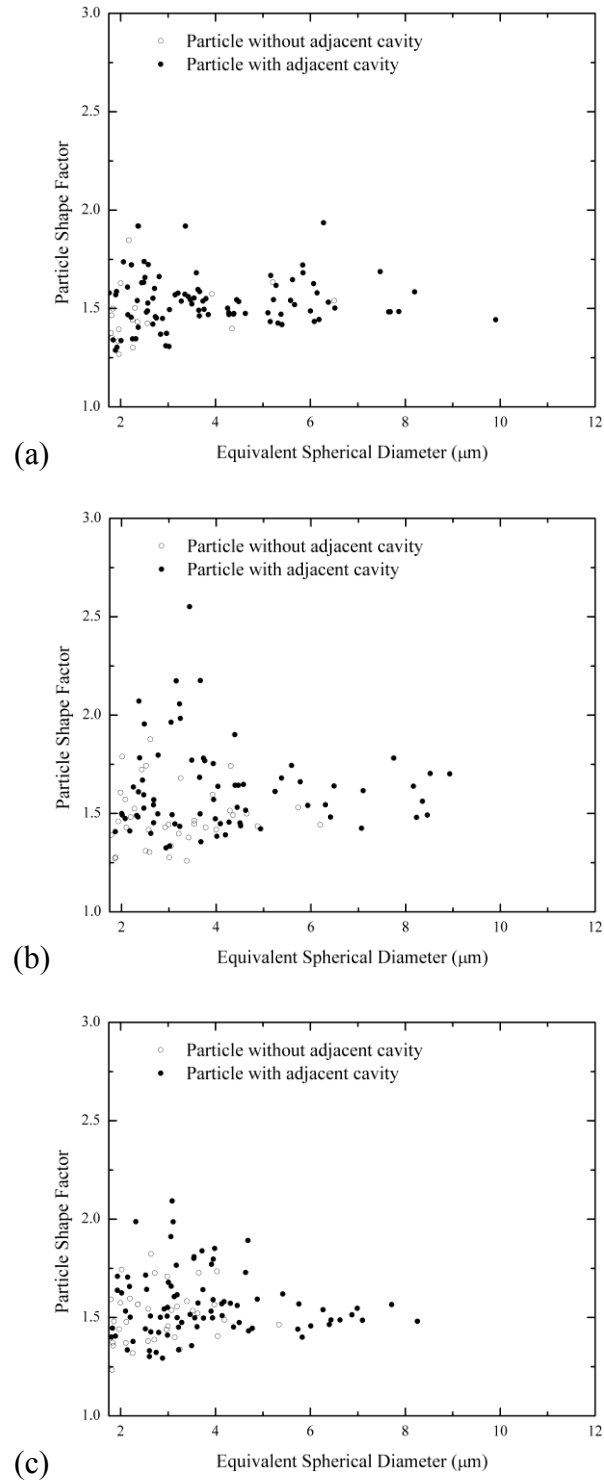


Fig. 6.9: Intermetallic particle size distributions for (a) $\text{Al}_6(\text{Mn,Fe})$ and (b) Mg-Si are shown.

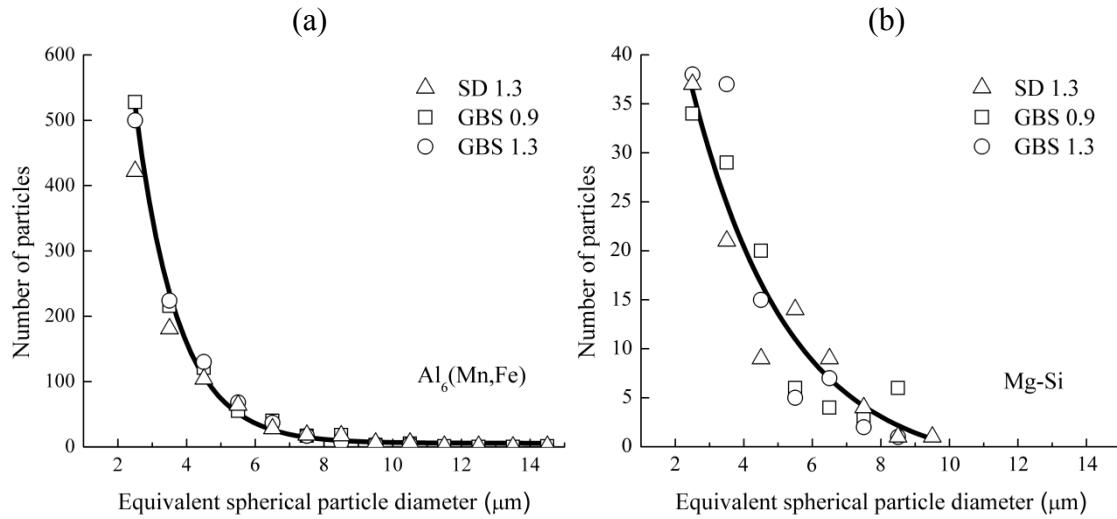
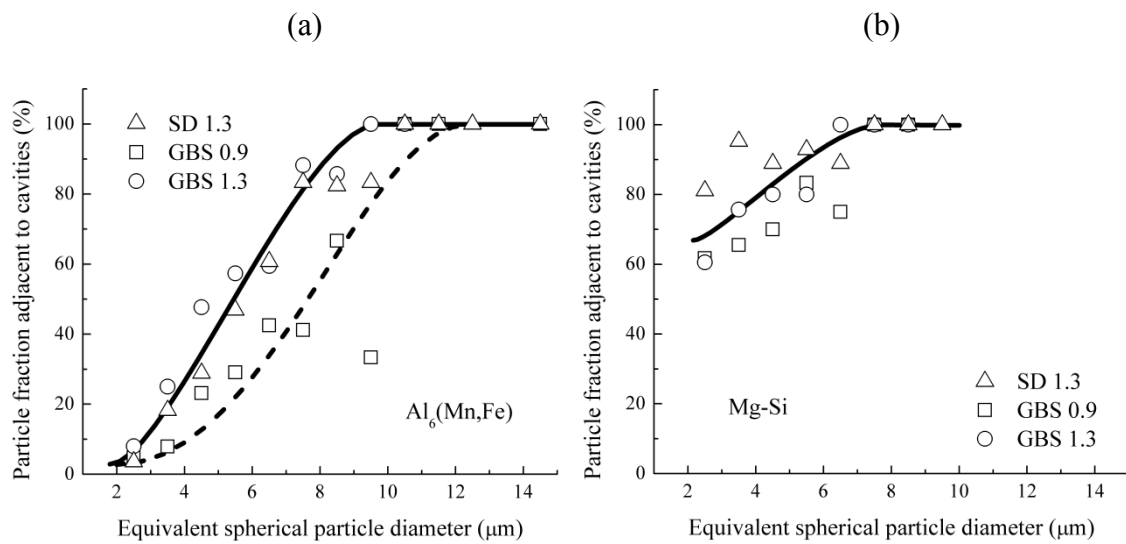


Fig. 6.10: The fraction of particles adjacent to cavities is shown as a function of equivalent spherical particle diameter for (a) $\text{Al}_6(\text{Mn,Fe})$ and (b) Mg-Si intermetallic particles.



Chapter 7: Two-Dimensional Characterization

In contrast to 3-D microstructure characterization by visualizing and analyzing 3-D data sets, conventional 2-D microstructure characterization relies on examination and image analysis of 2-D photomicrographs. Common metallographic methods involve the identification and measurement of phases, precipitates and constituents and the determination of the size and shape of grains, characteristics of grain boundaries and other observable defects. However, a microstructure is an ensemble of many features within a volume of material. Because of the limitations of 2-D data, these traditional metallography techniques may not easily reveal and quantify microstructural patterns, spatial distributions, correlations, clustering and interactions. Understanding relationships between spatial distribution of cavities and intermetallic particles, local true strain and deformation mechanism are particularly relevant in superplastic alloys. To derive numerical data from photomicrographs, quantitative image analysis is required. Such analysis is conducted in the current investigation to study the interaction of complex cavities and other microstructural features.

Two-point correlation functions are useful statistical descriptors for microstructural characterization of spatial distribution and heterogeneity of microstructural features. This technique is commonly used to mathematically represent correlations between microstructural features in 2-D metallographic data [105, 107-108, 114-115]. A two-point correlation function $\langle P_{ij} \rangle$ can represent the probability that a particular object (j) exists at a specific distance and along a specific direction from a chosen location (i). In this investigation, 2-D micrographs were analyzed using standard 2-D image analysis and two-point correlation functions to mathematically represent correlations between microstructural features, such as cavity, $\text{Al}_6(\text{Mn,Fe})$ particles and Mg-Si particles. These data provide supplementary information to 3-D characterization,

which was presented in chapter 6, for studying the cavitation damage in AA5083 material.

The two-point correlation functions used in the current study are generated from statistical analysis of data from 2-D photomicrographs. The particular images analyzed using two-point correlation functions are shown in Fig 7.1. These images were selected from the middle of three 3-D serial-section data sets, SD1.3, GBS0.9 and GBS1.3. Each image was recorded at a magnification of 200 \times with resolution of 0.18 μm / pixel and a size of 3000 \times 2000 pixels, which corresponds to a physical area of 540 \times 360 μm . Cavities and particles are denoted by different colors. The Reconstruct software package [89] was used for microstructure identification and analysis. Area fraction, spherical diameter and size distribution of two types of particles and cavities were measured using ImageJ image-analysis software [110]. The numbers of cavities and two types of intermetallic particles analyzed from these 2-D images are provided in Table 7.1. Data for cavity and particle spherical diameter distribution in each specimen are given in Fig. 7.2. From these data, only small differences in the particle sizes and distributions are evident. The quantity of $\text{Al}_6(\text{Mn,Fe})$ particles is significantly larger than Mg-Si particles in all 2-D image data. Conversely, cavities are very different in size and distribution between the three data sets. Further quantitative image analyses, such as two-point correlation function analysis, are required to characterize microstructural patterns, spatial distributions, correlations, clustering and interactions between microstructural features.

The following relationships between pairs of microstructural features were calculated using this methodology: 1. cavities and cavities (cavity/cavity), 2. $\text{Al}_6(\text{Mn,Fe})$ particles and $\text{Al}_6(\text{Mn,Fe})$ particles ($\text{Al}_6(\text{Mn,Fe})/\text{Al}_6(\text{Mn,Fe})$), 3. $\text{Al}_6(\text{Mn,Fe})$ particles and cavities ($\text{Al}_6(\text{Mn,Fe})/\text{cavity}$) and 4. Mg-Si particles and cavities (Mg-Si/cavity). Because of small number of Mg-Si particles in each of 2-D image data, correlations between Mg-

Si particles and Mg-Si particles would not be statistically meaningful and are not reported in this study. The calculation of two-point correlations between objects of the same phase, e.g. cavity/cavity or $\text{Al}_6(\text{Mn,Fe})/\text{Al}_6(\text{Mn,Fe})$, involves details worth noting. The first step in calculating the two-point correlation function is to choose a point, a pixel from a 2-D image, which lies on a particular object (phase). Then a second point (pixel) is chosen at another location, and a calculation is made for these two points. The two-point correlation function is essentially an accumulation of such calculations over an area sufficient in size to provide statistical significance to the result. When the first and second points lie on the same phase, a decision must be made in the calculation process. This decision depends on whether the two points lying on the same phase also lie on separate objects, to the extent which it is possible to distinguish separate objects in a 2-D image. Thus, calculation of the two-point correlation function between points within the same phase can: 1. include all point pairs without regard to the specific objects included, identifying only the phases, or 2. exclude those point pairs which lie on the same object. Each of these methods produces different information, and two-point correlation functions were calculated by both methods for this study.

By specifying different measurement distances (r) of two-point correlation functions, image analysis can be conducted for small ($\sim 0.5 \mu\text{m}$) as well as large scales ($\sim 120 \mu\text{m}$) depending on the size and resolution of analyzed image. Since the average intermetallic particle size is less than $8 \mu\text{m}$ in diameter, and most cavities are less than $10 \mu\text{m}$ in diameter in the current study, a $27 \mu\text{m}$ (150 pixels) measurement distance was chosen, which defines a $54 \times 54 \mu\text{m}^2$ (301×301 pixels) analysis array to reveal correlations and spatial distributions of microstructural features while preserving detailed interactions.

7.1 THE CAVITY – CAVITY CORRELATION

This correlation calculates the two-point correlation function between points within cavity and includes all point pairs without regard to the specific objects included. Both types of contour plot, probability in percentage shown in the left column and probability in normalized unit shown in the right column, are provided for all analyses. Results of the cavity/cavity correlation calculated from SD 1.3, GBS 0.9 and GBS 1.3 images are shown as contour plots in Fig. 7.3. In the left column of Fig. 7.3, numbers shown on the contours are probabilities in percentage. Dashed contours represent locations of completely random correlation, i.e. no meaningful correlation between objects, which were calculated by averaging the probabilities at all locations. The dashed contours are, thus, a value of unity for the normalized two-point correlation function, i.e. $\langle P_{ij} \rangle = 1$. In the right column of Fig. 7.3, numbers shown on the contours represent the normalized probabilities, where the value above “1” stands for the probability more than the random level. All contour plots are shown in the same orientation, where the tensile direction is horizontal and the long transverse direction is vertical.

These plots in Fig. 7.3 provide information such as cavity size, morphology and the degree of alignment. In the SD 1.3 specimen, cavities are elongated and aligned along the tensile direction. In the GBS 0.9 specimen, cavities are rounded and somewhat aligned along the tensile direction. In the GBS 1.3 specimen, cavities are rounded, and no alignment between cavities is observed.

7.2 THE $\text{Al}_6(\text{Mn,Fe})$ – CAVITY CORRELATION

In $\text{Al}_6(\text{Mn,Fe})$ /cavity correlation contour plots shown in Fig. 7.4, very weak evidence for $\text{Al}_6(\text{Mn,Fe})$ particles aligning with cavities along the tensile axis is observed in the SD 1.3 and GBS 0.9 specimens, but no such alignment is observed in the GBS 1.3 specimen.

7.3 THE Mg-Si – CAVITY CORRELATION

In Fig. 7.5, Mg-Si/cavity correlation contour plots show that Mg-Si particles more strongly align with cavities along the tensile axis in the SD 1.3 and GBS 0.9 specimens than do $\text{Al}_6(\text{Mn,Fe})$ particles, but no alignment is observed in the GBS 1.3 specimen. These results suggest that particles, particularly Mg-Si intermetallic particles, are interacting with cavities under some testing conditions. However, further details of the relationships between particles and cavities are not available from these 2-D data.

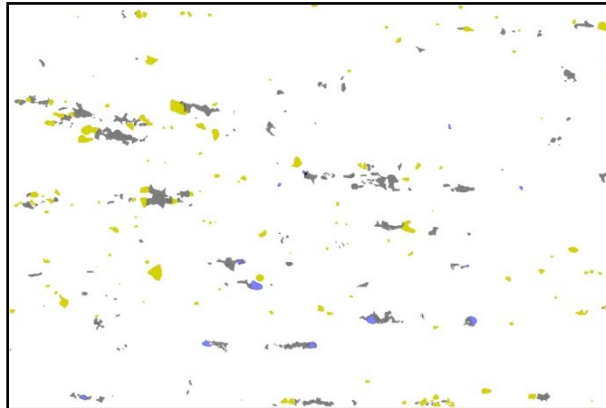
In order to elucidate the degree to which microstructural features are aligned along the tensile axis in the SD 1.3 specimen, two-point correlations were calculated by the second method, which excludes point pairs lying on the same object. This calculation reveals alignment between objects and effectively excludes the effect of individual object shape. These calculations for correlations between cavities, designated cavity/separate cavity, and $\text{Al}_6(\text{Mn,Fe})$ particles, designated $\text{Al}_6(\text{Mn,Fe})$ /separate $\text{Al}_6(\text{Mn,Fe})$, are presented in Fig. 7.6. Fig. 7.6(a) reveals that separate cavities are strongly aligned along the tensile axis in the SD 1.3 specimen. Similar calculations revealed much weaker alignment of cavities along the tensile direction in the GBS 0.9 specimen. Because the tensile axis is parallel to the rolling direction in the specimens studied, it is possible that stringers of intermetallic particles aligned with the rolling direction might affect the alignment of cavities. Fig. 7.6(b) reveals alignment of $\text{Al}_6(\text{Mn,Fe})$ particles with the tensile (rolling) direction. However, the alignment of cavities with the tensile direction in the SD 1.3 specimen, Fig. 7.6(a), is less than that of $\text{Al}_6(\text{Mn,Fe})$ particles with the tensile (rolling) direction, Fig. 7.6(b). Thus, the alignment of cavities along the tensile axis is a result of more than intermetallic particle stringers and can be largely attributed to the SD creep mechanism. Somewhat remarkably, the degree of cavity alignment with the tensile direction in the GBS 0.9 specimen, Fig. 7.6(c), is very similar to that of the $\text{Al}_6(\text{Mn,Fe})$

particles, Fig. 7.6(b). This suggests that $\text{Al}_6(\text{Mn,Fe})$ particles are nucleation sites for cavities, at least in GBS creep deformation. The lesser number of Mg-Si particles prevented a statistically meaningful calculation of two-point correlations to determine alignment of this particle type.

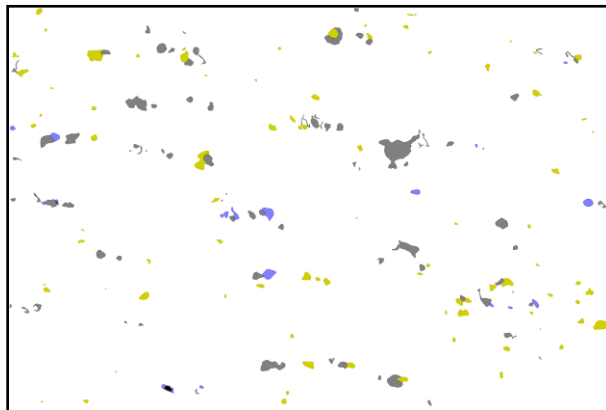
Table 7.1: The number and area fraction of cavity and two types of intermetallic particles are shown for three data sets.

Data Set	Microstructural Feature	Number of Features	Area Fraction of Feature
SD 1.3	Cavity	154	1.7
	Al ₆ (Mn,Fe)	128	1.1
	Mg-Si	12	0.1
GBS 0.9	Cavity	77	1.5
	Al ₆ (Mn,Fe)	186	1.5
	Mg-Si	15	0.1
GBS 1.3	Cavity	213	13.9
	Al ₆ (Mn,Fe)	128	0.9
	Mg-Si	16	0.1

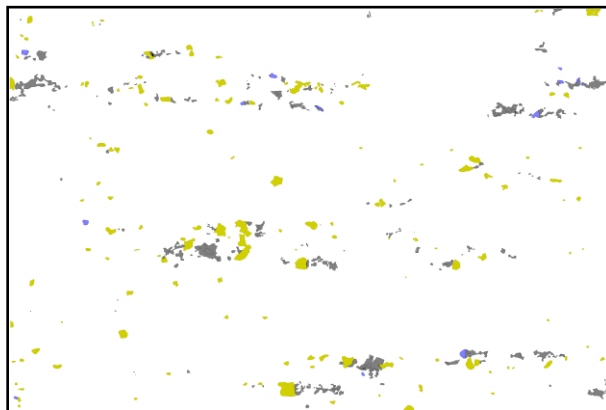
Fig. 7.1: Images used for two-point correlation function analysis from 2-D data sets (a) SD 1.3, (b) GBS 0.9 and (c) GBS 1.3 are shown. Microstructural features in these images are cavities in gray, $\text{Al}_6(\text{Mn,Fe})$ particles in yellow and Mg-Si particles in purple.



(a)

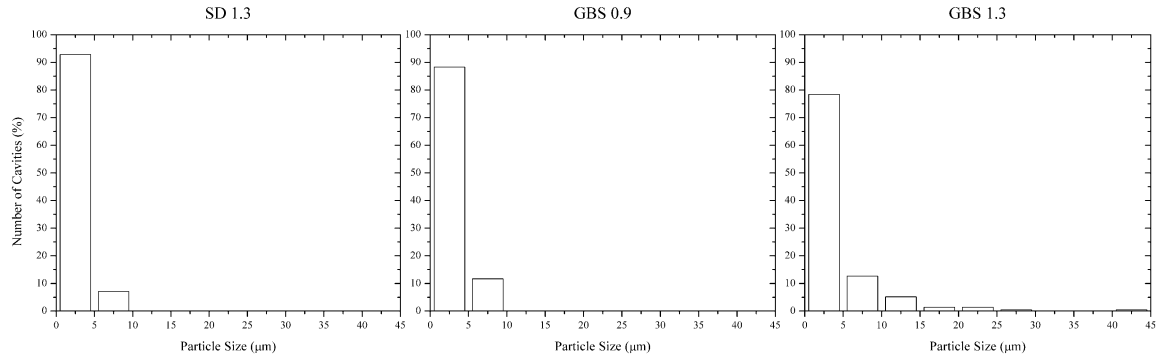


(b)

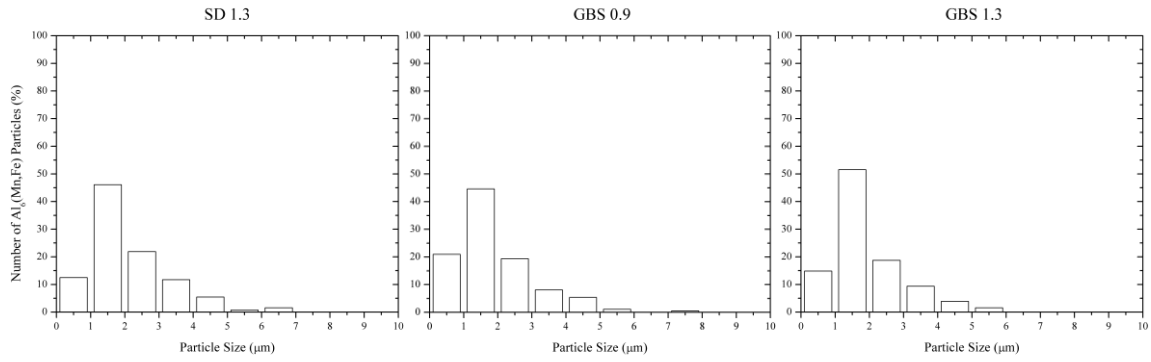


(c)

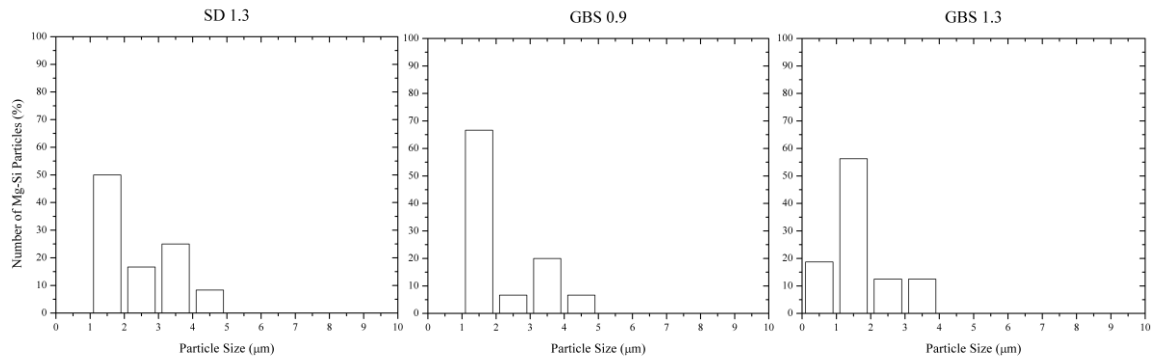
Fig 7.2: Histograms of the size distributions for (a) cavity (b) $\text{Al}_6(\text{Mn,Fe})$ particles and (c) Mg-Si particles from images of three data sets are shown.



(a)

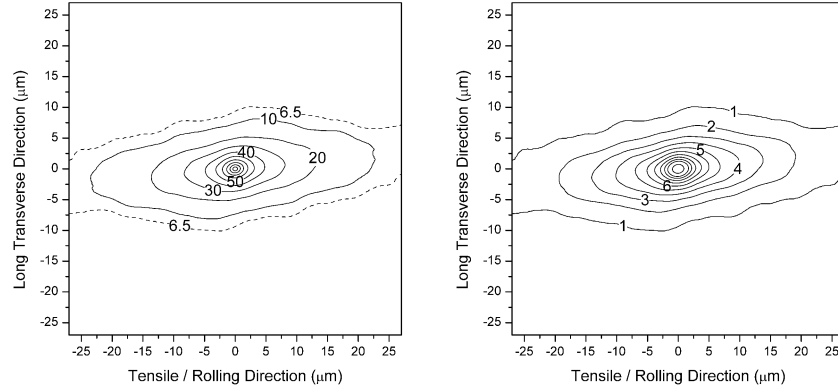


(b)

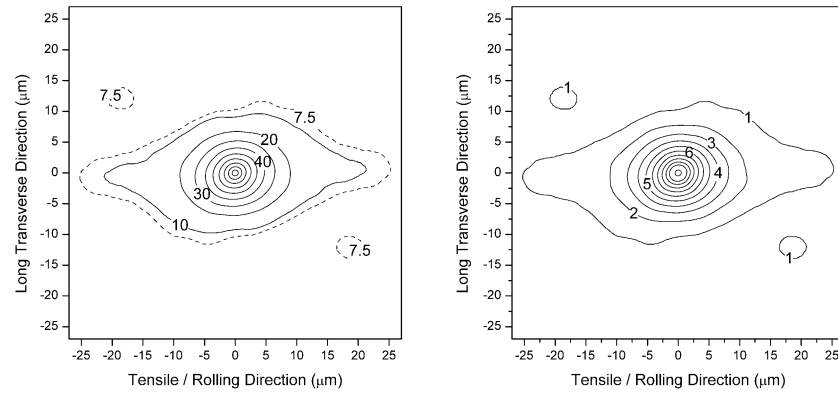


(c)

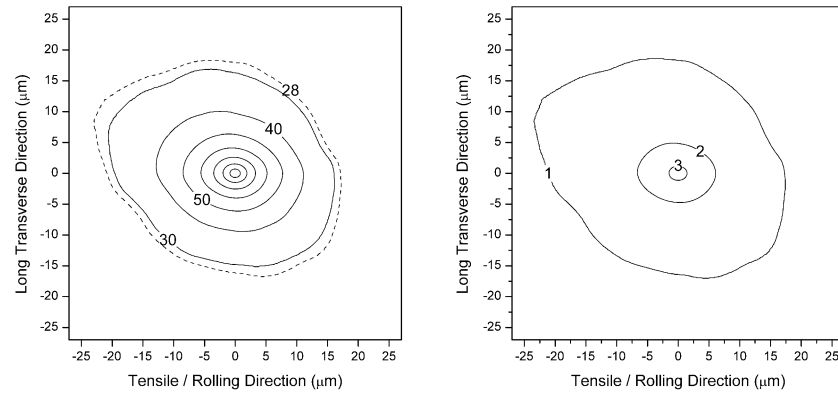
Fig. 7.3: Two-point correlation analyses for (a) SD 1.3: Cavity/Cavity, (b) GBS 0.9: Cavity/Cavity and (c) GBS 1.3: Cavity/Cavity are reported in contour plots.



(a) SD 1.3: Cavity/Cavity

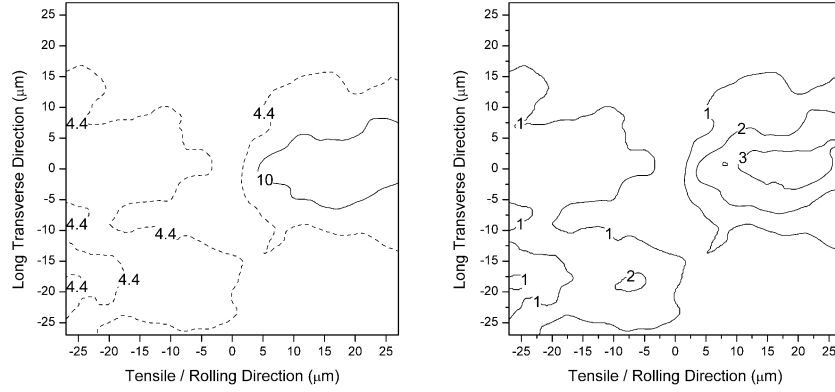


(b) GBS 0.9: Cavity/Cavity

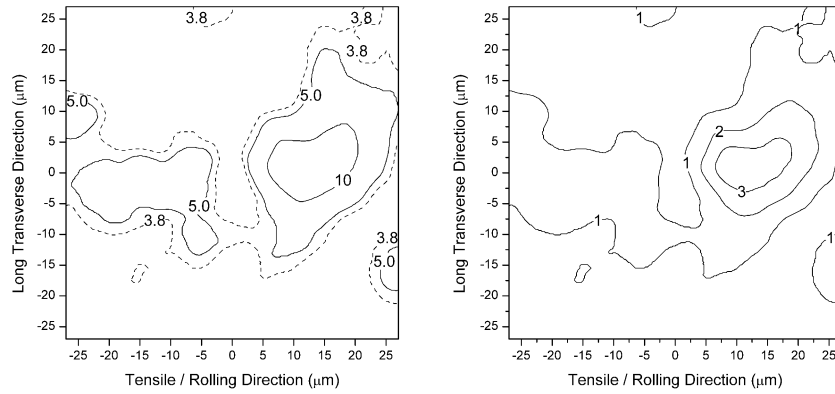


(c) GBS 1.3: Cavity/Cavity

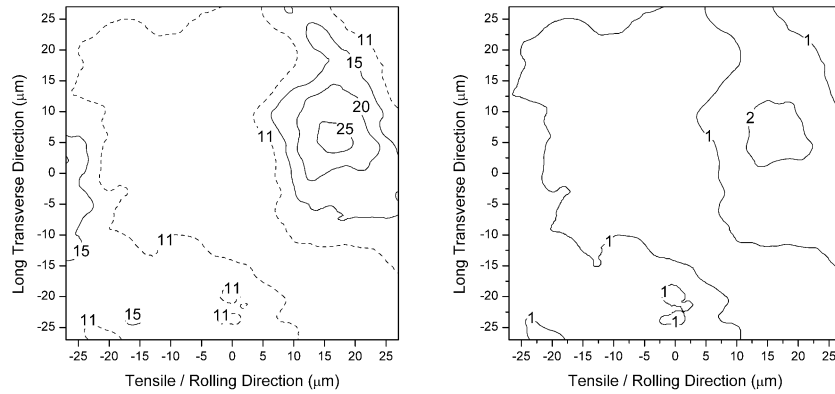
Fig. 7.4: Two-point correlation analyses for (a) SD 1.3: $\text{Al}_6(\text{Mn,Fe})/\text{Cavity}$, (b) GBS 0.9: $\text{Al}_6(\text{Mn,Fe})/\text{Cavity}$ and (c) GBS 1.3: $\text{Al}_6(\text{Mn,Fe})/\text{Cavity}$ are reported in contour plots.



(a) SD 1.3: $\text{Al}_6(\text{Mn,Fe})/\text{Cavity}$

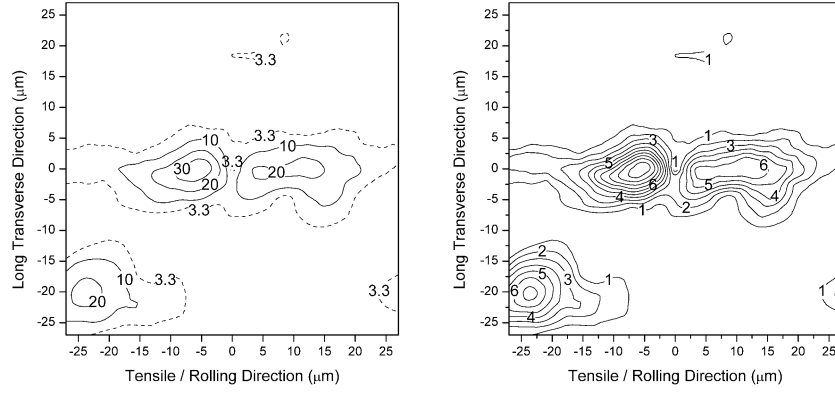


(b) GBS 0.9: $\text{Al}_6(\text{Mn,Fe})/\text{Cavity}$

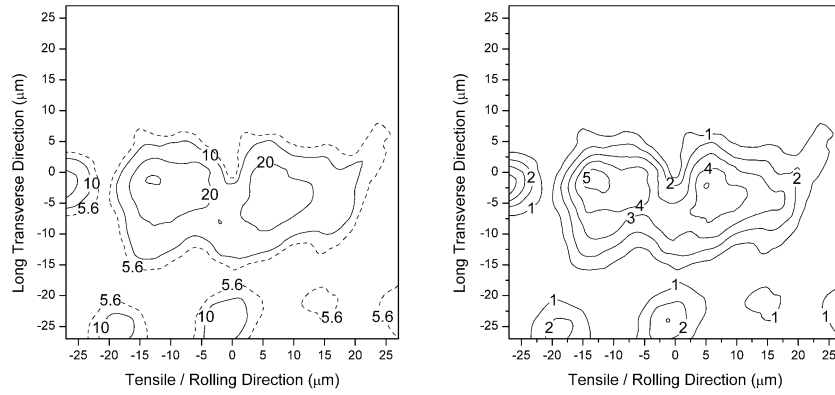


(c) GBS 1.3: $\text{Al}_6(\text{Mn,Fe})/\text{Cavity}$

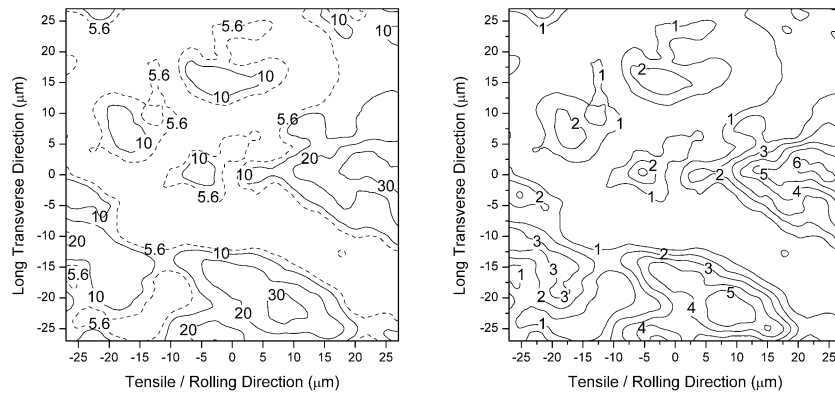
Fig. 7.5: Two-point correlation analyses for (a) SD 1.3: Mg-Si/Cavity, (b) GBS 0.9: Mg-Si/Cavity and (c) GBS 1.3: Mg-Si/Cavity are reported in contour plots.



(a) SD 1.3: Mg-Si/Cavity

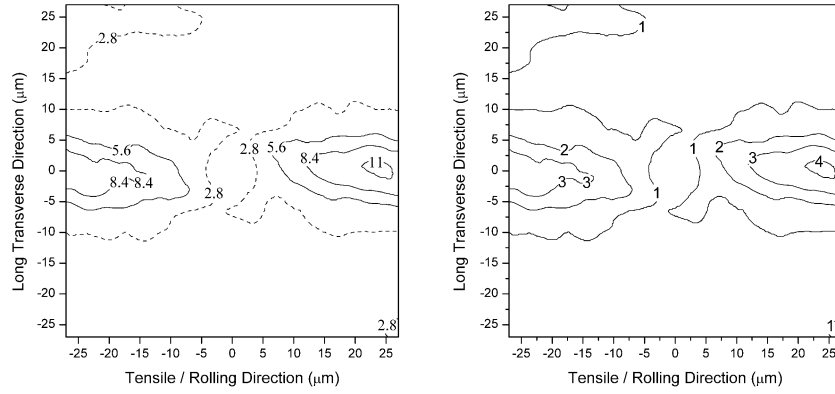


(b) GBS 0.9: Mg-Si/Cavity

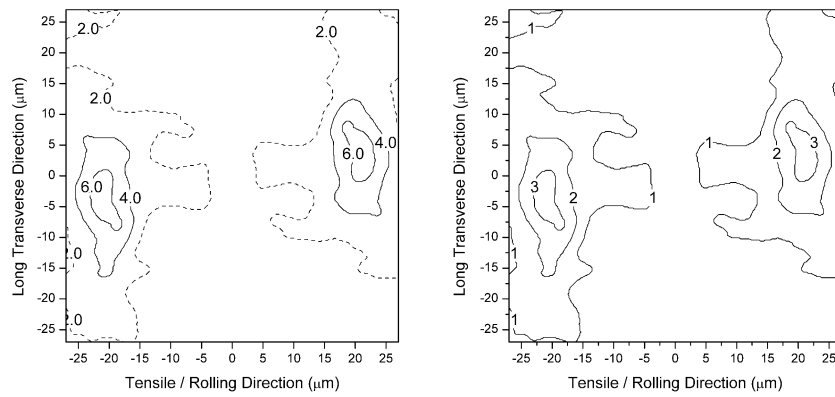


(c) GBS 1.3: Mg-Si/Cavity

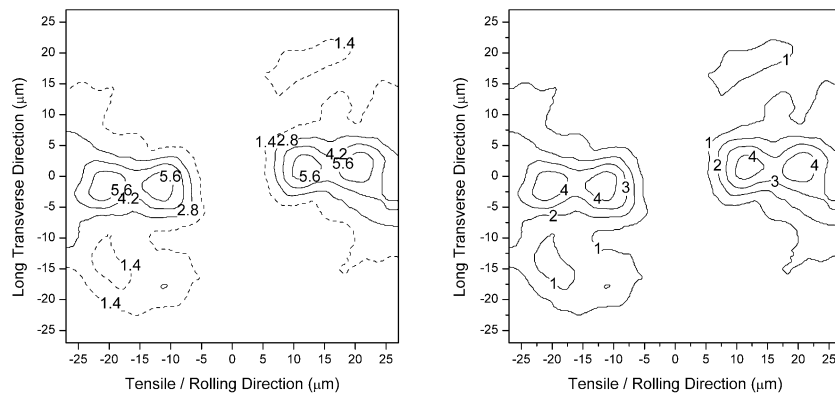
Fig. 7.6: Two-point correlation analyses for (a) SD 1.3: Cavity/Separate Cavity, (b) SD 1.3: $\text{Al}_6(\text{Mn,Fe})$ /Separate $\text{Al}_6(\text{Mn,Fe})$ and (c) GBS 0.9: Cavity/Separate Cavity are reported in contour plots.



(a) SD 1.3: Cavity/Separate Cavity



(b) SD 1.3: $\text{Al}_6(\text{Mn,Fe})$ /Separate $\text{Al}_6(\text{Mn,Fe})$



(c) GBS 0.9: Cavity/Separate Cavity

Chapter 8: Conclusion

Results of failure surface characterization confirm that the mechanism of filament formation is oxide growth. No filaments were observed on specimens tested in vacuum. High concentrations of oxygen and magnesium were observed in newly exposed surfaces and in filaments on specimens tested in air, indicating that magnesium-rich oxide was formed during testing. These results suggest that the formation of filaments on fine-grained AA5083 material during superplastic deformation occurs by growth of magnesium-rich oxides. Further investigation is needed to definite the oxide growth mechanism and characterize the crystalline structure of filaments. This could be accomplished using a combination focused ion beam (FIB) to remove individual filaments and transmission electron microscopy (TEM) to characterize those filaments.

The experimental investigation of 3-D microstructural features and the supplemental results from two-point correlation functions provides new insight into the nature of cavitation evolution in AA5083 sheet materials deformed at elevated temperatures and strain rates similar to those used in the SPF and QPF commercial forming processes. Cavitation developed under conditions promoting GBS creep is distinctly different from cavitation developed under conditions promoting SD creep. GBS creep produces cavities that grow quickly with strain and develop into very large, interconnected cavity structures. SD creep produces a larger number of smaller cavities which align along the tensile direction, which is identical to the rolling direction in this study, and have a lesser propensity to interconnect. The initiation of cavitation occurs at a similar strain for both GBS and SD creep deformation, and initiation was previously shown to occur at a similar strain for both deformation mechanisms. Taking adjacency between intermetallic particles and cavities as an indication of cavity nucleation at

particles leads to the following conclusions. Large $\text{Al}_6(\text{Mn,Fe})$ particles, particularly those with equivalent spherical diameters of greater than $10\text{ }\mu\text{m}$, tend to initiate cavities. All $\text{Al}_6(\text{Mn,Fe})$ particles with a diameter of $10\text{ }\mu\text{m}$ or greater were found to be adjacent to cavities. Mg-Si particles of all sizes examined are very likely to nucleate cavities. Even Mg-Si particles in the size range of 2 to $3\text{ }\mu\text{m}$ have a probability greater than 60% of residing adjacent to a cavity. These results clearly indicate that a reduction in size of the coarsest $\text{Al}_6(\text{Mn,Fe})$ particles and a reduction or elimination of Mg-Si intermetallic particles will have the beneficial effect of reducing cavitation in AA5083 sheet used for SPF and QPF operations.

However, several unresolved issues remain in understanding cavitation behaviors. Future investigations should focus on characterizing the role of grain boundaries and crystallographic texture during cavitation, as this study does not reveal the effect of these microstructural features. An EBSD study including grain boundary information would be useful to further understand the cavity growth mechanisms during creep deformation. Additional data sets at small strains would be useful for clarifying the initiation stage of cavitation. Specimens tested with the tensile direction perpendicular to the rolling direction would be helpful to reveal the effect of microstructural anisotropy, such as alignment of intermetallic particles along stringers, on cavitation evolution [116].

Appendix

Program A: Calculation of two-point correlation function using Mathematica™ 6.0

```
SetDirectory["C:\\Documents and Settings\\brian\\My Documents\\PCF\\SD1.3_33"];

Block[{a,b},a=b=0;

data=Import["SD1.3_33.PGM","Data"];

data01=Import["SD1.3_33_01.PGM","Data"];

data02=Import["SD1.3_33_02.PGM","Data"];

data03=Import["SD1.3_33_03.PGM","Data"];

rmax=Input["The Maximum Measurment Distance (Pixel)"];

countX=Input["Image Size of X (Horizontal) axis "]-2;

countY=Input["Image Size of Y (Vertical) axis "]-2;

Print["Analysis Progress...",Dynamic[Round[Refresh[100. a/(countY+1-2 rmax),UpdateInterval→10],
01]],"%"];

Print["Y=",Dynamic[Refresh[a,UpdateInterval→10]],"/",countY+1-2 rmax];

Print["X=",Dynamic[Refresh[b,UpdateInterval→10]],"/",countX+1-2 rmax];

cp=rmax+1;

p11M=p12M=p13M=p21M=p22M=p23M=p31M=p32M=p33M=Array[0&,{2 rmax+1, 2 rmax+1}];

ts=tf=SessionTime[];

Print["Running Time... ",Dynamic[Round[Refresh[(tf-ts)/60, UpdateInterval→10],.1]], " Min"];

Print["Time to Finish... ",Dynamic[Round[Refresh[(((tf-ts) (countY+2-2 rmax)/(a+1))-(tf-ts))/60,
UpdateInterval→10],.1]], " Min"];

Label["start"];

bp=data[[cp+a,cp+b]];

If[bp==0,Goto["nextpixelB"]];
```



```

tpm01=data01[[1+a;;2 rmax+1+a,1+b;;2 rmax+1+b]];
tpm02=data02[[1+a;;2 rmax+1+a,1+b;;2 rmax+1+b]];
tpm03=data03[[1+a;;2 rmax+1+a,1+b;;2 rmax+1+b]];
If[bp==1,Goto["bpp2"],If[bp< 2,Goto["bpp3"],Goto["bpp4"]]];
Label["bpp2"];
p11M=p11M+tpm01;p12M=p12M+tpm02;p13M=p13M+tpm03;
Goto["nextpixelB"];
Label["bpp3"];
p21M=p21M+tpm01;p22M=p22M+tpm02;p23M=p23M+tpm03;
Goto["nextpixelB"];
Label["bpp4"];
p31M=p31M+tpm01;p32M=p32M+tpm02;p33M=p33M+tpm03;
Label["nextpixelB"];
If[(countX-b)<2 rmax, Goto["nextpixelA"], b++];
Goto["start"];
Label["nextpixelA"];
b=0;
If[(countY-a)<2 rmax, Goto["end"], a++];
tf=SessionTime[];
Goto["start"];
Label["end"];
Print["Exporting Data..."];
Export["p11M.csv",MatrixForm[p11M]];
Export["p12M.csv",MatrixForm[p12M]];
Export["p13M.csv",MatrixForm[p13M]];

```

```
Export["p21M.csv",MatrixForm[p21M]];
Export["p22M.csv",MatrixForm[p22M]];
Export["p23M.csv",MatrixForm[p23M]];
Export["p31M.csv",MatrixForm[p31M]];
Export["p32M.csv",MatrixForm[p32M]];
Export["p33M.csv",MatrixForm[p33M]];
Print["Analysis Completed!!!"];]
```

Program B: Calculation of self and self-excluded correlation functions using

Mathematica™ 6.0

```
SetDirectory["C:\\Users\\Brian\\Desktop\\Brian\\Brian\\PCF\\SD1.3_33"];

Block[{a,b},a=b=0;

data=Import["SD1.3_33.PGM","Data"];

Print["SD1.3_33.PGM....loaded"];

data01=Import["SD1.3_33_01.PGM","Data"];

Print["SD1.3_33_01.PGM....loaded"];

data01a=Import["SD1.3_33_01_#.PGM","Data"];

Print["SD1.3_33_01_#.PGM....loaded"];

data02=Import["SD1.3_33_02.PGM","Data"];

Print["SD1.3_33_02.PGM....loaded"];

data02a=Import["SD1.3_33_02_#.PGM","Data"];

Print["SD1.3_33_02_#.PGM....loaded"];

data03=Import["SD1.3_33_03.PGM","Data"];

Print["SD1.3_33_03.PGM....loaded"];

data03a=Import["SD1.3_33_03_#.PGM","Data"];

Print["SD1.3_33_03_#.PGM....loaded"];

rmax=Input["The Maximum Distance (Pixel)"];

countX=Input["Image Size of X (Horizontal) axis "]-2;

countY=Input["Image Size of Y (Vertical) axis "]-2;

Print["Analysis Progress...",Dynamic[Round[Refresh[100. a/(countY+1-2 rmax),UpdateInterval→10],.
01]],"%"];

Print["Y=",Dynamic[Refresh[a,UpdateInterval→10]],"/",countY+1-2 rmax];

Print["X=",Dynamic[Refresh[b,UpdateInterval→10]],"/",countX+1-2 rmax];
```

```

cp=rmax+1;

p11self=p11sep=p22self=p22sep=p33self=p33sep=Array[0&,{2 rmax+1,2 rmax+1}];

ts=tf=SessionTime[];

Print["Running Time... ",Dynamic[Round[Refresh[(tf-ts)/60,UpdateInterval→10],.1]]," Min"];

Print["Time to Finish... ",Dynamic[Round[Refresh[(((tf-ts) (countY+2-2 rmax)/(a+1))-(tf-
ts))/60,UpdateInterval→10],.1]]," Min"];

Label["start"];

bp=data[[cp+a,cp+b]];

If[bp==0,Goto["nextpixelB"]];

If[bp==1,Goto["bpp1"],If[bp==2,Goto["bpp2"],Goto["bpp3"]]];

Label["bpp1"];

tpm01self=D[data01a[[1+a;;2 rmax+1+a,1+b;;2 rmax+1+b]]/. data01a[[cp+a,cp+b]] →x,x];

tpm01sep=data01[[1+a;;2 rmax+1+a,1+b;;2 rmax+1+b]]-tpm01self;

p11self=p11self+tpm01self;

p11sep=p11sep+tpm01sep;

Goto["nextpixelB"];

Label["bpp2"];

tpm02self=D[data02a[[1+a;;2 rmax+1+a,1+b;;2 rmax+1+b]]/. data02a[[cp+a,cp+b]] →x,x];

tpm02sep=data02[[1+a;;2 rmax+1+a,1+b;;2 rmax+1+b]]-tpm02self;

p22self=p22self+tpm02self;

p22sep=p22sep+tpm02sep;

Goto["nextpixelB"];

Label["bpp3"];

tpm03self=D[data03a[[1+a;;2 rmax+1+a,1+b;;2 rmax+1+b]]/. data03a[[cp+a,cp+b]] →x,x];

tpm03sep=data03[[1+a;;2 rmax+1+a,1+b;;2 rmax+1+b]]-tpm03self;

```

```

p33self=p33self+tpm03self;

p33sep=p33sep+tpm03sep;

Label["nextpixelB"];

If[(countX-b)<2 rmax, Goto["nextpixelA"], b++];

Goto["start"];

Label["nextpixelA"];

b=0;

If[(countY-a)<2 rmax, Goto["end"], a++];

tf=SessionTime[];

Goto["start"];

Label["end"];

Print["Exporting Data..."];

Export["p11self.csv",MatrixForm[p11self]];

Export["p11sep.csv",MatrixForm[p11sep]];

Export["p22self.csv",MatrixForm[p22self]];

Export["p22sep.csv",MatrixForm[p22sep]];

Export["p33self.csv",MatrixForm[p33self]];

Export["p33sep.csv",MatrixForm[p33sep]];

Print["Analysis Completed!!!"];]

```

Remarks:

1. The image to be analyzed was first converted to “PGM” format using ImageJ software and stored in a working folder for data input and output.
2. This “PGM” image can be manipulated to create several image data, so that data01, data02 and data03 contain only one microstructure feature (coded as “1”)

and aluminum matrix (coded as “0”). For example, data01 contains only cavities and matrix, data02 contains only $\text{Al}_6(\text{Mn,Fe})$ particles and matrix, and data03 contains only Mg-Si particles and matrix. The “data” contains all microstructure features with the following coding: 0 = matrix, 1 = cavity, 2 = $\text{Al}_6(\text{Mn,Fe})$ particle and 3 = Mg-Si particle.

3. The rmax is the maximum distance (r) in two-point correlation functions.
4. “countX” and “countY” are the size of the horizontal and vertical pixels of image. For the current image size, countX = 3000 and countY = 2000.
5. p11M, p12M, p13M, p21M, p22M, p23M, p31M, p32M and p33M arrays are two-point correlation function. The size of these arrays depends on the size of rmax. The current study uses rmax = 150 pixel. This will create a 301×301 rectangular array for analysis in the data image.
6. “cp” (Center Point) is used to represent the x and y coordinates of the two-point correlation function arrays such as pxxM. The first point of cp is (151, 151) in the current study.
7. “bp” is the base point acquired from “data” of specific x-y coordinates. “bp” can be 1, 2, 3, or 4, depending on microstructure features.
8. “tpm01”, “tpm02” and “tpm03” are top point arrays with size equal to “pxxM” arrays. These arrays are moving pixel by pixel and represent the specific area of data01, data02 and data03.
9. The “pxxM” arrays are equal to specific two-point correlation functions. The first x is the origin point (*i*) and the second x is the correlated point (*j*) in a two-point correlation function $\langle P_{ij} \rangle$. For example, the p12M represents the two-point correlation function for cavity/ $\text{Al}_6(\text{Mn,Fe})$. After the analysis, the program will

generate “pxxM.csv” files, which contain all correlation events during calculation. Further calculation is needed to acquire the desired two-point correlation function.

Bibliography

- [1] M-A Kulas, W. P. Green, E. M. Taleff, P. E. Krajewski and T. R. McNelley. "Failure mechanism in superplastic AA5083 materials." *Metallurgical and Materials Transactions A*, 37A (2006) 645-655.
- [2] W. Gan, S.S. Babu, N. Kapustka, and R.H. Wagoner. "Microstructural Effects on the Springback of Advanced High-Strength Steel." *Metallurgical and Materials Transactions A*, 37A (2006) 3221-3231.
- [3] IBIS Associates (M. Bull and R. Chavali). "Benefit Analysis: Use of Aluminum Structures in Conjunction with Alternative Powertrain Technologies in Automobiles" *Aluminum Association*, May 2008.
- [4] A. I. Taub, P. E. Krajewski, A. A. Luo, and J. N. Owens. "The evolution of technology for materials processing over the last 50 years: The automotive example." *JOM*, 59 (2007) 48-57.
- [5] A. I. Taub. "Materials Challenges for a Sustainable Automotive Industry." The Byron E. Short Lecture in Mechanical Engineering, The University of Texas at Austin, Austin, TX. March 28th, 2008.
- [6] C. A. Ungureanu, S. Das and I. S. Jawahir. "Life-cycle Cost Analysis: Aluminum versus Steel in Passenger Cars." *Proceedings of a Symposia, TMS*, (2007) 11-24.
- [7] P. A. Friedman and S. G. Luckey, "On the expanded usage of superplastic forming of aluminum sheet for automotive applications." *Materials Science Forum*, 447-448 (2004) 199-204.
- [8] P. E. Krajewski and J. G. Schroth. "Overview of Quick Plastic Forming Technology." *Materials Science Forum*, 551-552 (2007) 3-12.
- [9] J. R. Davis. *ASM Specialty Handbook: Aluminum and Aluminum Alloys*. ASM Intl., 1993.
- [10] H. Iwasaki, K. Higashi, S. Tanimura, T. Komatubara and S. Hayami, "Superplastic Deformation Characteristics of 5083 Aluminum Alloy." *Superplasticity in Advanced Materials*, Ed's: S.Hori, M.Tokizane and N. Furushiro, The Japan Society for Research on Superplasticity, (1991) 447-452.
- [11] R. Verma, P. A. Friedman, A. K. Ghosh, S. Kim and C. Kim. "Characterization of superplastic deformation behavior of a fine grain 5083 Al alloy sheet." *Metallurgical and Materials Transactions A*, 27A (1996) 1889-1898.

- [12] E. M. Taleff, P. J. Nevland, and P. E. Krajewski. "Tensile ductility of several commercial aluminum alloys at elevated temperatures." *Metallurgical and Materials Transactions A*, 32A (2001) 1119-1130.
- [13] T. R. McNelley, K. Oh-Ishi, A. P. Zhilyaev, S. Swaminthan, P. E. Krajewski and E. M. Taleff. "Characteristics of the Transition from Grain-Boundary Sliding to Solute Drag Creep in Superplastic AA5083." *Metallurgical and Materials Transactions A*, 39A (2008) 50-64.
- [14] F. J. Humphreys. "The nucleation of recrystallization at second phase particles in deformed aluminium." *Acta Metallurgica*, 25 (1977) 1323-44.
- [15] C. F. Martin, J. J. Blandin, and L. Salvo. "Variations in microstructure and texture during high temperature deformation of Al-Mg alloy." *Materials Science & Engineering: A*, 297(1-2) (2001) 212-222.
- [16] V. I. Polkin, A. O. Nikiforov, and I. I. Novikov. "Peculiarities of technological route to produce SP sheets of AMg₄ (analog of 5083) alloy." *Materials Science Forum*. 170-172 (1994) 329-332.
- [17] J. S. Vetrano, C. A. Lavender, C. H. Hamilton, M. T. Smith, and S. M. Bruemmer. "Superplastic behavior in a commercial 5083 aluminum alloy." *Scripta Metallurgica et Materialia*, 30 (1994) 565-570.
- [18] D. Sherby and J. Wadsworth. "Superplasticity - recent advances and future directions." *Progress in Materials Science*, 33 (1989) 169-221.
- [19] H. Watanabe, K. Ohori, and Y. Takeuchi. "Superplastic behavior of Al-Mg-Cu alloys." *Transactions of the Iron and Steel Institute of Japan*, 27(9) (1987) 730-733, 1987.
- [20] J. Hu, K. Ikeda and T. Murakami. "Effect of heat treatment after hot-rolling on texture and formability for 5083 alloy sheet." *Journal of Japan Institute of Light Metals*, 46 (1996) 126-131.
- [21] S. Kim, M. P. Balogh and R. A. Waldo, *Advances in Superplastic Forming*. E. M. Taleff, P. A. Friedman, P. E. Krajewski, R. S. Mishra and J. G. Schroth, eds., TMS 2004 139-149.
- [22] Y. S. Sato, S. H. C. Park, and H. Kokawa. "Microstructural factors governing hardness in friction-stir welds of solid-solution-hardened Al alloys." *Metallurgical and Materials Transactions A*, 32A (2001) 3033-3042.
- [23] N. Llorca-Isern, C. Luis-Perez, P. A. Gonzalea, L. Laborde and D. Patino, "Analysis of structure and mechanical properties of AA 5083 aluminium alloy

- processed by ECAE.” *Reviews on Advanced Materials Science*, 10 (2005) 473-478.
- [24] M. Czechowski. “Low-cycle fatigue of friction stir welded Al-Mg alloys.” *Journal of Materials Processing Technology*, 164-165 (2005) 1001-1006.
 - [25] G. Lucadamo, N. Y. C. Yang, C. San Marchi and E. J. Lavernia. “Microstructure characterization in cryomilled Al 5083.” *Materials Science & Engineering*, A430 (2006) 230-241.
 - [26] A. J. Barnes. “Superplastic Forming 40 Years and Still Growing.” *Journal of Materials Engineering and Performance*, 16 (2007) 440-454.
 - [27] T. G. Nieh, J. Wadsworth and O. D. Sherby. *Superplasticity in Metals and Ceramics*. Cambridge University Press, 1997.
 - [28] D. G. Sanders. “The current state-of-the-art and the future in airframe manufacturing using superplastic forming technologies.” *Materials Science Forum*, 357-359 (2001) 17-22.
 - [29] M-A Kulas, W. P. Green, E. M. Taleff, P. E. Krajewski and T. R. McNelley. “Deformation mechanisms in superplastic AA5083 materials.” *Metallurgical and Materials Transactions A*, 36A (2005) 1249-1261.
 - [30] E. M. Taleff, W. P. Green, M-A Kulas, T. R. McNelley. and P. E. Krajewski “Analysis, representation, and prediction of creep transients in Class I alloys.” *Materials Science & Engineering*, A410-411 (2005) 32-37.
 - [31] J. R Bradley and J. E. Carsley. *Advance in Superplasticity and Superplastic Forming*, E. M. Taleff, P.A. Friedman, P. E. Krajewski, R. S. Mishra and . G. Schroth, eds., TMS, Warrendale, PA, (2004) 149-157.
 - [32] W. D. Nix. “On some fundamental aspects of superplastic flow.” *In Superplastic Forming*, Ed. by. S. P. Agrawal, Metals Park: ASM, (1985), 3–12.
 - [33] A. Ball and M. M. Hutchison. “Superplasticity in the Aluminum-Zinc eutectoid.” *Metal Science Journal*, 3 (1969) 1-7.
 - [34] A. K. Mukherjee. “The rate controlling mechanism in superplasticity.” *Materials Science and Engineering*, 8(2) (1971) 83-89.
 - [35] T. G. Langdon. “Grain boundary sliding as a deformation mechanism during creep.” *Philosophical Magazine*, 22(178) (1970) 689-700.

- [36] R. C. Gifkins. "Grain-boundary sliding and its accommodation during creep and superplasticity." *Metallurgical and Materials Transactions A*, 7(8) (1976) 1225-1232.
- [37] H. Fukuyo, H. C. Tsai and O. D. Sherby. "Superplasticity and Newtonian-viscous Flow in Fine-grained Class I Solid Solution Alloys" *ISIJ International*, 31(1) (1991) 76-85.
- [38] J. Weertman. "Theory of steady-state creep based on dislocation climb." *Journal of Applied Physics*, 26(10) (1955) 1213-1217.
- [39] D. Sherby and P. M. Burke. "Mechanical behavior of crystalline solids at elevated temperature." *Progress in Materials Science*, 13 (1968) 325-390.
- [40] P. Yavari, F. A. Mohamed and T. G. Langdon. "Creep and substructure formation in an Al-5%Mg solid solution alloy." *Acta Metallurgica*, 29(8) (1981) 1495-1507.
- [41] J. Weertman. "Steady-state creep of crystal." *Journal of Applied Physics*, 28(10) (1957) 1185-1189.
- [42] E. M. Taleff and J. Qiao. "Numerical modeling of solute-drag creep." *Modeling The Performance of Engineering Structural Materials II*, TMS, Warrendale, PA, (2001) 3-12.
- [43] W. R. Cannon and O. D. Sherby. "High temperature creep behavior of Class I and Class II solid solution alloys." *Metallurgical Transactions*, 1 (1970) 1030-1032.
- [44] F. A. Mohamed and T. G. Langdon. "Transition from dislocation climb to viscous glide in creep of solid solution alloys." *Acta Metallurgica*, 22(6) (1974) 779-88.
- [45] J. Weertman. "Creep of indium, lead, and some of their alloys with various metals." *Trans. TMS-AIME*, 218 (1960) 207-218.
- [46] K. Oh-ishi, J. F. Boydon and T. R. McNelley. "Deformation mechanisms and cavity formation in superplastic AA5083." *Advances in Superplasticity and Superplastic Forming*, Proceedings of a Symposium held during the TMS Annual Meeting, Charlotte, NC, Mar. (2004) 14-18.
- [47] D. H. Bae and A. K. Ghosh. "Cavity formation and early growth in a superplastic Al-Mg alloy." *Acta Materialia*, 50(3) (2002) 511-523.
- [48] D. H. Bae and A. K. Ghosh. "Cavity growth during superplastic flow in an Al-Mg alloy: I. Experimental study." *Acta Materialia*, 50(3) (2002) 993-1009.
- [49] D. H. Bae and A. K. Ghosh. "Cavity growth in a superplastic Al-Mg alloy: II. An improved plasticity based model." *Acta Materialia*, 50(3) (2002) 1011-1029.

- [50] E. M. Taleff and P. J. Nevland. "The high-temperature deformation and tensile ductility of Al alloys." *JOM* 51(1) (1999) 34-36.
- [51] E. M. Taleff, T. Leon-Salamanca, R. A. Ketcham, R. Reyes and W. D. Carlson. "Nondestructive evaluation of cavitation in an Al-Mg material deformed under creep conditions." *Journal of Materials Research*, 15(1) (2000) 76-84.
- [52] P. A. Friedman and A. K. Ghosh. "Microstructural Evolution and Superplastic Deformation Behavior of Fine Grain 5083Al." *Metallurgical and Materials Transactions A*, 27(A) (1996) 3827-3839.
- [53] H. Iwasaki, T. Mori, T. Tagata, M. Matsuo and K. Higashi. "Cavitation in Superplastic Al-Mg Alloy." *Materials Science Forum*, 233-234 (1997) 81-88.
- [54] R. M. Cleveland, A. K. Ghosh and J. R. Bradley. "Comparison of superplastic behavior in two 5083 aluminum alloys." *Materials Science & Engineering*, A351(1-2) (2003) 228-236.
- [55] H. Q. Yu, J. J. Blandin and L. Salvo. "Comparison between 2D and 3D characterizations of damage induced by superplastic deformation." *Materials Science Forum*, 447-448 (2004) 55-60.
- [56] N. Chandra, M. K. Khraisheh and P. Kalu. "Effect of state of stress on the cavitation behavior of Al 5083 superplastic material." *Materials Science Forum*, 475-479 (2005) 2931-2936.
- [57] R. Raj and M. F. Ashby. "Intergranular fracture at elevated temperature." *Acta Metallurgica*, 23 (1975) 653-666.
- [58] A. H. Chokshi and T. G. Langdon. "A model for diffusional cavity growth in superplasticity." *Acta Metallurgica*, 35 (1987) 1089-1101.
- [59] E. Smith and J. T. Barnby. "Nucleation of grain-boundary cavities during high-temperature creep." *Metal Science Journal*, 1 (1967) 1-4.
- [60] A. C. F. Cocks and M. F. Ashby. "Creep fracture by coupled power-law creep and diffusion under multiaxial Stress." *Metal Science*, 16 (1982) 465-474.
- [61] M. J. Stowell, D. W. Livesey, and N. Ridley. "Cavity coalescence in superplastic deformation." *Acta Metallurgica*, 32 (1984) 35-42.
- [62] J. Pilling. "Effect of Coalescence on cavity growth during superplastic deformation" *Materials Science and Technology*, 1 (1985) 461-465.

- [63] B. Kim and K. Hiraga. "Simulation of cavitation processes in superplastic deformation." *Metallurgical and Materials Transactions A*, 33A (2002) 3449-3455.
- [64] P. D. Nicolaou and S. L. Semiatin. "An analysis of the effect of continuous nucleation and coalescence on cavitation during hot tension testing." *Acta Materialia*, 48 (2000) 3441-3450.
- [65] M. A. Khaleel, H. M. Zbib and E. A. Nyberg. "Constitutive modeling of deformation and damage in superplastic materials." *International Journal of Plasticity*, 17 (2001) 277-206.
- [66] J. Pilling and N. Ridley. "Superplasticity in crystalline solids." *The Institute of Metals*, London (1989)102.
- [67] J. W Hancock. "Creep cavitation without a vacancy flux." *Metal Science*, 10(9) (1976) 319-25.
- [68] C. F. Martin, C. Josserond, J. J. Blandin, L. Salvo, P. Cloetens and E. Boller. "X-ray microtomography study of cavity coalescence during superplastic deformation of an AL-Mg alloy." *Materials Science and Technology*, 16 (2000) 1299-1301.
- [69] L. Dupuy and J. J. Blandin. "Damage sensitivity in a commercial Al alloy processed by equal channel angular extrusion." *Acta Materialia*, 50 (2002) 3251–3264.
- [70] L. Salvo, P. Cloetens, E. Maire, S. Zabler, J. J. Blandin, J. Y. Buffiere, W. Ludwig, E. Boller, D. Bellet and C. Josserond. "X-ray micro-tomography an attractive characterisation technique in materials science." *Nuclear Instruments and Methods in Physics Research B*, 200 (2003) 273–286.
- [71] C. L. Chen and M. J. Tan. "Cavity growth and filament formation of superplastically deformed Al 7475 Alloy." *Materials Science & Engineering*, A298 (2001) 235-244.
- [72] Y. Takayama, T. Tozawa and H. Kato. "Superplasticity and thickness of liquid phase in the vicinity of solidus temperature in a 7475 aluminum alloy." *Acta Materialia*, 47 (1999) 1263-1270.
- [73] M. G. Zelin. "On micro-superplasticity." *Acta Materialia*, 45 (1997) 3533-3542.
- [74] W. J. D. Shaw, I. A. Gunee and M. Kuhn. "Modeling of microsuperplasticity in mechanically alloyed aluminum." *International Journal of Fracture*, 97 (1999) 103-111.

- [75] R. B. Grishaber, R. S. Mishra and A. K. Mukherjee. "Effect of testing environment on intergranular microsuperplasticity in an aluminum MMC." *Materials Science & Engineering*, A220 (1996) 78-84.
- [76] W. J. D. Shaw. "The role of microsuperplastic flow in high temperature fracture of AL-9021 mechanically alloyed aluminium" *Journal of Materials Science Letters*, 24 (1989) 4114-4119.
- [77] W. D. Cao, X. P. Lu and H. Conrad. "Whisker formation and the mechanism of superplastic deformation." *Acta Materialia*, 44 (1996) 697-706.
- [78] S. Griffiths, D. Whittle, N. Ridley and R. I. Todd. "Superplasticity in commercial Al 7475." *Materials Science Forum*, 447-448 (2004) 283-288.
- [79] J. H. Robinson, M. A. Rust and R. I. Todd. "Mechanisms of microsuperplasticity." *Materials Science Forum*, 551-552 (2007) 135-145.
- [80] J. J. Blandin, B. Hong, A. Varloteaux, M. Suery and G. L'Esperance. "Effect of the nature of grain boundary regions on cavitation of a superplastically deformed aluminum alloy." *Acta Materialia*, 44 (1996) 2317-2326.
- [81] S. F. Claeys, J. W. Jones and J. E. Allison. *Dispersion Strengthened Aluminum Alloys*. Y.-W. Kim and W. M. Griffith, eds., TMS: Warrendale, PA, (1988) 323-336.
- [82] W. J. D. Shaw. "Microsuperplastic behavior." *Materials Letters*, 4 (1985) 1-4.
- [83] Y. Takayama, S. Sasaki, T. Tozawa, H. Kato, H. Watanabe and M. Kokubo. "Superplasticity and fractography over wide range of temperature and strain rate in a 5083 aluminum alloy." *Journal of Japan Institute of Light Metals*, 49 (1999) 378-382.
- [84] W. P. Green, M-A. Kulas, A. Niazi, K. Oh-ishi, E. M. Taleff, P. E. Krajewski and T. R. McNelley. "Deformation and failure of a superplastic AA5083 aluminum material with a Cu addition." *Metallurgical and Materials Transactions A*, 37A (2006) 2727-2738.
- [85] D. H. Bae and A. K. Ghosh. "Observation Related to Healing of Interface Damage and Cavity Nucleation during Superplastic Flow." *Materials Science & Engineering*, A322 (2002) 233-240.
- [86] O. D. Sherby and J. Wadsworth. *Superplasticity in Aerospace*, H. C. Heikkinen and T. R. McNelley, eds., TMS, Warrendale, PA, (1988) 3-27.
- [87] N. Ridley and Z.C. Wang. "Cavitation in Superplastic Metals." *Materials Science Forum*, 170-172 (1994) 177-186.

- [88] J. Pimenoff, Y. Yagodzinskyy, J. Romu and H. Hanninen. "Effects of the Temperature of Warm Rolling on the Superplastic Behaviour of AA5083 Aluminum base Alloy." *Materials Science Forum*, 357-359 (2001) 277-282.
- [89] F. N. Rhines and K. R. Craig. "Measurement of average grain volume and topological parameters by serial sectioning analysis." *Metallurgical and Materials Transactions A*, 7A (1976) 1729-1734.
- [90] M. V. Kral, M. A. Mangan, G. Spanos and R. O. Rosenberg. "Three-dimensional analysis of microstructures." *Materials Characterization*, 45 (2000) 17-23.
- [91] M. V. Kral and G. Spanos "Three-dimensional analysis of proeutectoid cementite precipitates." *Acta Materialia*, v47 n2 (1999) 711-724.
- [92] H. Singh and A. M. Gokhale. "Visualization of three-dimensional microstructures." *Materials Characterization*, 54 (2005) 21– 29.
- [93] N. Chawla, V. V. Ganesh and B. Wunsch. "Three-dimensional (3D) microstructure visualization and finite element modeling of the mechanical behavior of SiC particle reinforced aluminum composites." *Scripta Materialia*, 51 (2004)161-165.
- [94] M. Li, S. Ghosh, T. N. Rouns, H. Weiland, O. Richmond and W. Hunt. "Serial section method in the construction of 3-D microstructures for particle-reinforced MMCs." *Materials Characterization*, 41 (1998) 81-95.
- [95] J. E. Spowart, H. M. Mullens and B. T. Puchala. "Collecting and Analyzing Microstructures in Three Dimensions: A Fully Automated Approach." *JOM*, 55(10) (2003) 35-37.
- [96] H. F. Poulsen, X. Fu, E. Knudsen, E. M. Lauridsen, L. Margulies and S. Schmidt. "3DXRD – Mapping Grains and Their Dynamics in 3 Dimensions." *Materials Science Forum*, 467-470 (2004) 1363-1372.
- [97] H. F. Poulsen, D. J. Jensen and G. B. M. Vaughan. "Three-Dimensional X-Ray Diffraction Microscopy Using High-Energy X-Rays." *MRS Bulletin*, Mar. (2004) 166-169.
- [98] J. R. Davids, Ed. *ASM Specialty Handbook, Aluminium and Aluminum Alloys*, ASM International, (1993).
- [99] ANSI H35.1. *American National Standard Alloy and Temper Designation Systems for Aluminum*, American National Standards Institute (2004).
- [100] J. Alkemper and P. W. Voorhees. "Quantitative serial sectioning analysis". *Journal of Microscopy*, 201(3) 2001 388-394.

- [101] J. C. Fiala. "Reconstruct: A Free Editor for Serial Section Microscopy." *Journal of Microscopy*, 218 (2005) 52-61.
- [102] A. M. Gokhale, A. Tewari and H. Garmestani. "Constraints on microstructural two-point correlation functions." *Scripta Materialia*, 53 (2005) 989-993.
- [103] ASM metals handbook. *Metallography and microstructures*, vol. 9. Materials Park, OH: ASM International, (2004) 428.
- [104] S. Lin, H. Garmestani and B. Adams. "The evolution of probability functions in an inelastically deforming two-phase medium." *International Journal of Solids and Structures*, 37 (2000) 423-434.
- [105] A. Tewari, A. M. Gokhale, J. E. Spowart and D. B. Miracle. "Quantitative characterization of spatial clustering in three-dimensional microstructures using two-point correlation functions." *Acta Materialia*, 52 (2004) 307-319.
- [106] D. S. Li, G. Saheli, M. Khaleel and H. Garmestani. "Quantitative prediction of effective conductivity in anisotropic heterogeneous media using two-point correlation functions." *Computational Materials Science*, 38 (2006) 45-50.
- [107] H. Singh, A. M. Gokhale, Y. Mao and J. E. Spowart. "Computer simulations of realistic microstructures of discontinuously reinforced aluminum alloy (DRA) composites" *Acta Materialia*, 54 (2006) 2131-2143.
- [108] A. D. Rollett, R. Campman and D. Saylor. "Three Dimensional Microstructures: Statistical Analysis of Second Phase Particles in AA7075-T651." *Materials Science Forum*, 519-521 (2006) 1-10.
- [109] P. B. Corson. "Correlation functions for predicting properties of heterogeneous materials. I. Experimental measurement of spatial correlation functions in multiphase solids." *Journal of Applied Physics*, 45 (1974) 3159-3164.
- [110] M. D. Abramoff, P. J. Magelhaes and S. J. Ram. "Image Processing with ImageJ". *Biophotonics International*, 11(7) (2004) 36-42.
- [111] Wolfram Research, Inc., *Mathematica*, Version 5.0, Champaign, IL (2003).
- [112] D. Drouin, A.R. Couture, D. Joly, X. Tastet, V. Aimez, R. Gauvin. "CASINO V2.42-a fast and easy-to-use modeling tool for scanning electron microscopy and microanalysis users." *Scanning*, 29 (2007) 92-101.
- [113] I. M. Ritchie, J. V. Sanders and P. L. Weickhardt. "Oxidation of a dilute aluminum magnesium alloy." *Oxidation of Metals*, 3 (1971) 91-101.

- [114] H. Singh, Y. Mao, A. Sreeranganathan and A. M. Gokhale. "Application of digital image processing for implementation of complex realistic particle shapes/morphologies in computer simulated heterogeneous microstructures." *Modelling and Simulation in Materials Science and Engineering*, 14(3) (2006) 351-363.
- [115] K. Marthinsen, J. M. Fridy, T. N. Rouns, K. B. Lippert and E. Nes. "Characterization of 3-D particle distributions and effects on recrystallization kinetics and microstructure." *Scripta Materialia*, 39(9) (1998) 1177-1183.
- [116] M-A Kulas, P. E. Krajewski, J. R. Bradley, and E. M. Taleff. "Forming-limit diagrams for hot-forming of AA5083 aluminum sheet: Continuously cast material." *Journal of Materials Engineering and Performance*, 16(3) (2007) 308-313.

Vita

Jung-Kuei (Brian) Chang was born in Chiayi, Taiwan on January 29, 1975. In 1990, he entered National Taipei Institute Technology, Taiwan. In August 1995, he received degree of Bachelor of Materials Engineering and joined the R.O.C army in the same year. After retired from military, he attended the graduate school in National Tsing Hua University, Taiwan. He completed a M.S. degree in Materials Science and Engineering, and was employed by a semiconductor equipment manufacturing company in 2000. In 2003, he enrolled in the graduate school in University of Texas at Arlington for one year and then transferred to the University of Texas at Austin.

Permanent address: 3F, 118, Sec. 3, San-Ho Rd. Sanchun City, Taipei, Taiwan

This dissertation was typed by the author.